Cosmology with Clusters of Galaxies: High-redshift Clusters and the Evolution of Cluster Substructure

by

Tesla Erin Jeltema

B.S. Physics (1999)
College of William and Mary

Submitted to the Department of Physics
in partial fulfillment of the requirements for the degree of

Doctor of Philosophy

at the

MASSACHUSETTS INSTITUTE OF TECHNOLOGY

June 2004

Author .....
Department of Physics
May 18, 2004

Certified by .....
Claude R. Canizares
Associate Provost and Professor of Physics
Thesis Supervisor

Accepted by .....
Thomas J. Greytak
Professor of Physics
Associate Department Head for Education

Cosmology with Clusters of Galaxies: High-redshift Clusters and the Evolution of Cluster Substructure

by

Tesla Erin Jeltema

Submitted to the Department of Physics
on May 18, 2004, in partial fulfillment of the
requirements for the degree of
Doctor of Philosophy

Abstract

Clusters of galaxies have become an important cosmological tool, yet we do not understand many aspects of their formation and development. In this thesis, I pursue two projects aimed at using clusters to constrain cosmology and better understanding cluster evolution.

First, I examine the *Chandra* observation of MS1054-0321. MS1054-0321 is the highest redshift cluster in the *Einstein* Medium Sensitivity Survey (EMSS), and it was one of the first high-redshift clusters observed with *Chandra*. I confirm that this cluster is hot and massive, although its temperature is slightly lower than inferred previously. I also detected an iron line in this cluster, one of the first detections of iron in a cluster at these redshifts, with an abundance consistent with early enrichment of the ICM. MS1054-0321 exhibits significant substructure, which I study in detail for the first time. In X-rays, it appears to be a nearly equal mass double cluster in the process of merging. Both the cluster galaxies and mass associated with the western subclump are offset from the X-ray peak, possibly indicating that the gas in the subclump is being stripped off as it falls into the cluster. Despite the lower temperature, I find that the detection of this cluster in the EMSS constrains Ω_m to be less than one.

In the second project, I investigate the evolution of cluster substructure with redshift, quantifying for the first time cluster structure out to $z \sim 1$. My sample includes 40 X-ray selected, luminous clusters from the *Chandra* archive, and I quantify cluster morphology using the power ratio method (Buote & Tsai 1995). I find that, as expected qualitatively from hierarchical models of structure formation, high-redshift clusters have more substructure and are dynamically more active than low-redshift clusters. Specifically, the clusters with $z > 0.5$ have significantly higher average third and fourth order power ratios than the lower redshift clusters. This observation of structure evolution indicates that dynamical state may be an important systematic effect in cluster studies seeking to constrain cosmology, and when calibrated against numerical simulations, structure evolution will itself provide interesting bounds on cosmological models.

Thesis Supervisor: Claude R. Canizares
Title: Associate Provost and Professor of Physics

Acknowledgments

First and foremost, I would like to thank my advisor, Professor Claude Canizares. He has provided valuable advice and guidance on everything from research to postdocs, he kept me from getting too bogged down in details, and he taught me to salsa. Somehow I always feel calmer and more clear-headed after I meet with him. I also received invaluable help from my collaborators Mark Bautz, David Buote, and Megan Donahue as well as many members of the MIT CXC group. Mark Bautz and Herman Marshall, in particular, patiently answered my many questions.

I would also like to thank my committee members, Professor Scott Burles and Professor Alan Guth, for their comments. I have had useful conversations with several of the other professors in the department, including Professor Schechter and Professor Bertschinger. I am also grateful to my fellow graduate students. Amalia Hicks and Mike Malm both worked with me early on when I was learning the Chandra analysis, and the astrophysics graduate students and the women in physics provided friendship and distraction through lunches, dinners, and beers. Finally, I would like to thank my friends and family who kept me sane throughout graduate school and the thesis process, assuming I qualify as sane.

Contents

List of Figures

List of Tables

Chapter 1

Introduction

1.1 Cosmology with Clusters

In the standard picture of hierarchical structure formation, structure in the universe forms through the gravitational collapse of primordial density perturbations. Massive clusters of galaxies represent the extreme high-density tail of the distribution of initial perturbations, and their formation is very sensitive to the underlying cosmology. The growth rate of density perturbations is reflected in the evolution of the number density of clusters with redshift. This evolution combined with the abundance of clusters in the present epoch has been used to constrain both the amplitude of density perturbations on an 8 h^{-1} Mpc scale, σ_8, and the matter density, Ω_m (e.g., Henry 2004; Vikhlinin et al. 2003; Borgani et al. 2001; Henry 2000; Donahue & Voit 1999; Eke et al. 1998). Harder to constrain but becoming possible with current and future high-redshift samples is the contribution from dark energy or a cosmological constant, Λ (e.g., Henry 2004; Ettori, Tozzi, & Rosati 2003; Vikhlinin et al. 2003). The sensitivity of cluster number density to cosmological model is shown in Figure 1. It is clear from Figure 1b that the density of massive, high-redshift clusters leads to the tightest constraints. For example, it has been shown that the observation of MS1054-0321, a massive cluster at z=0.83, in the *Einstein* Medium Sensitivity Survey (EMSS) alone constrains Ω_m to be less than one (Jeltema et al. 2001; Donahue et al. 1998).

Another method of using clusters to constrain cosmological models is through the fraction of their mass in baryons (e.g., White et al. 1993; Allen et al. 2003; Ettori et al. 2003; Vikhlinin et al. 2003). Clusters form out of large volumes, so their composition should reflect the composition of the universe as a whole (White et al. 1993). Most of the baryons in clusters are in the X-ray emitting gas, and the gas mass fraction, f_g, gives a lower limit on the cluster's baryon fraction. It can then be combined with measurements of the baryon density (e.g., Kirkman et al. 2003; Spergel et al. 2003; Burles, Nollett, & Turner 2001), Ω_B, to put an upper limit on $\Omega_m \leq \Omega_B/f_g$. A couple of recent papers have used gas mass fraction as a standard candle, constraining cosmological parameters through the assumption that gas mass fraction does not evolve with redshift (Allen et al. 2003; Ettori et al. 2003).

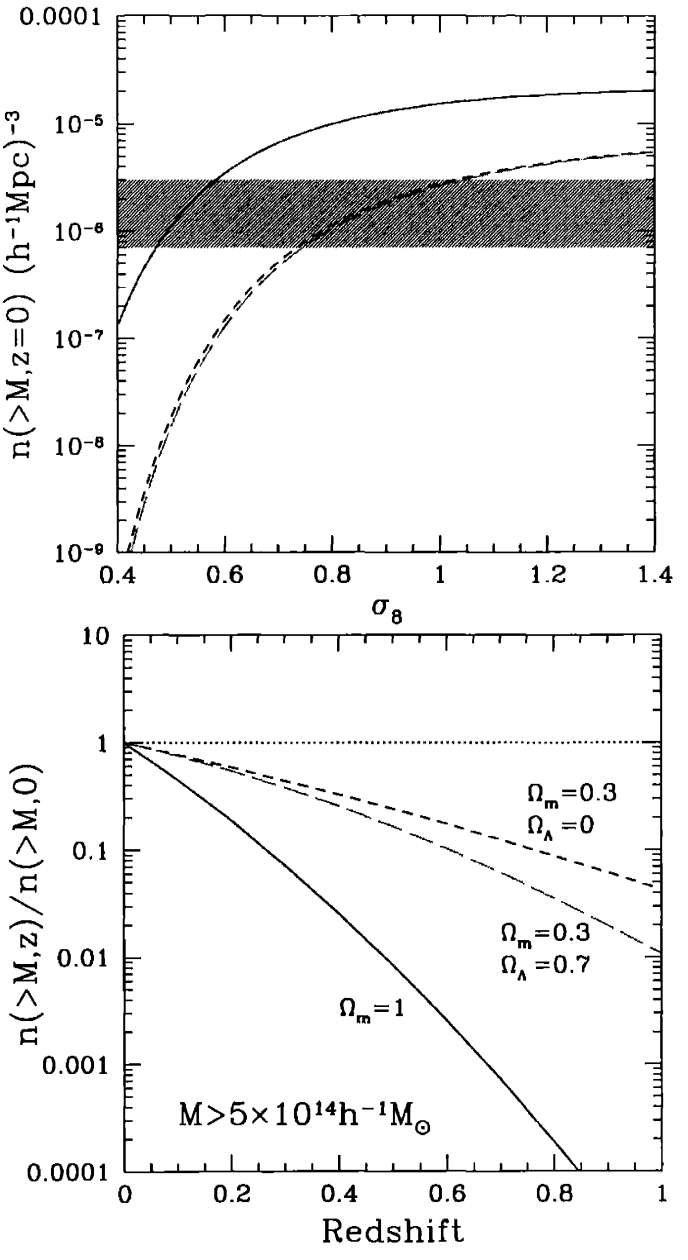

Figure 1-1 Adapted from Rosati, Borgani, & Norman (2002). The sensitivity of the cluster mass function to cosmological models. Top: The cumulative mass function at $z = 0$ for $M > 5 \times 10^{14} h^{-1} M_\odot$ for three cosmologies, as a function of σ_8, with the shape parameter of the power spectrum, $\Gamma = 0.2$; solid line, $\Omega_m = 1$; long-dashed line, $\Omega_m = 0.3$, $\Omega_\Lambda = 0.7$; short-dashed line, $\Omega_m = 0.3$, $\Omega_\Lambda = 0$. The shaded area indicates the observational uncertainty in the determination of the local cluster space density. Bottom: Evolution of $n(> M, z)$ for the same cosmologies and the same mass-limit, with $\sigma_8 = 0.5$ for the $\Omega_m = 1$ case and $\sigma_8 = 0.8$ for the low-density models.

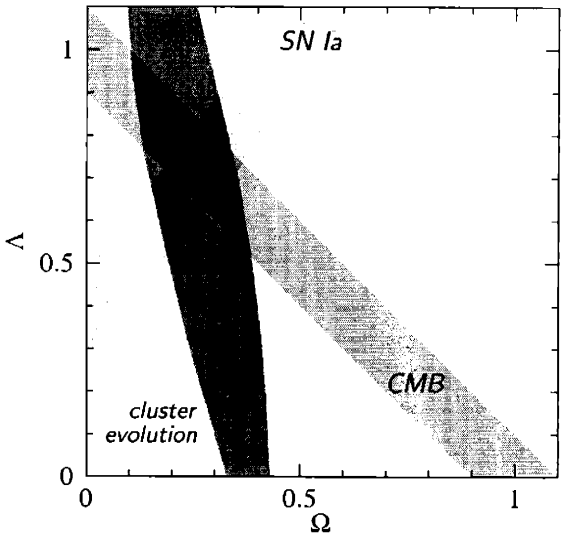

Figure 1-2 Adapted from Vikhlinin et al. (2003). Comparison of the cluster evolution constraints with those from distant supernova and the CMB. For each technique, the 68% confidence regions are shown. The CMB results were taken from Sievers et al. (2003) and Rubiño-Martin et al. (2003), the supernova results from Perlmutter et al. (1999) and Riess et al. (1998), and the cluster evolution results from Vikhlinin et al. (2003).

The cosmological constraints placed by clusters are independent and complementary to those placed by studies of the cosmic microwave background (CMB) and Type IA supernova (e.g., Spergel et al. 2003; Perlmutter et al. 1999; Riess et al. 1998). These different methods of studying cosmology act as checks for each other, and combining them gives tighter constraints by breaking the degeneracies among the parameters inherent in any one method. As an example, Figure 2 shows a comparison of the constraints on Ω_m and Ω_Λ placed by studies of the CMB, Type IA supernova, and cluster evolution.

1.2 Status of Observations

Determining cosmological parameters from cluster studies requires the ability to detect clusters over a large redshift range, a method of accurately determining cluster masses based on some observable quantity, and a well-known selection function. Cluster surveys generally search for clusters based on either an over-density of galaxies at optical wavelengths or the extended, hot intracluster medium (ICM) at X-ray wavelengths. Optical surveys are sensitive to both projection of structure along the line of sight and background subtraction, but the accuracy of detecting distant clusters can be significantly improved by using galaxy color information (e.g., Gladders & Yee 2000). X-ray selection, on the other hand, reliably identifies physically bound systems because the existence of a hot ICM indicates a deep potential well. The ICM emits via thermal bremsstrahlung, and the X-ray emissivity is proportional to the gas

density squared. Therefore, X-ray observations probe the densest regions of clusters and are less sensitive to projection than optical studies; although, the detection of high-redshift clusters in X-rays requires a reasonable time investment because of the need to be sensitive to low surface brightness extended sources. X-ray surveys are also flux-limited with fairly well-understood selection functions, leading to a well-defined survey volume.

Another advantage of X-ray observations is that cluster mass can be estimated from X-ray temperature or luminosity. This method assumes that the X-ray emitting gas is roughly in hydrostatic equilibrium with the cluster's gravitational potential. It has been shown through comparison to numerical simulations and other mass estimators to be reasonably accurate overall, though significant variations in luminosity and temperature can result from cluster mergers (Randall, Sarazin, & Ricker 2002; Ritchie & Thomas 2002; Mathiesen & Evrard 2001). Another method of estimating cluster mass is by measuring the velocity dispersion of the member galaxies and applying the virial theorem, an approach that also assumes dynamical equilibrium. The only method of detecting clusters that directly probes cluster mass is the measurement of the distortion of background galaxies due to weak lensing. However, weak lensing gives total mass along the line of sight. To date only a handful of clusters have been discovered through shear-selection, but the first weak lensing surveys are underway (Wittman et al. 2003). Also in its infancy is the detection of clusters through the distortion of the CMB spectrum when the CMB photons inverse-Compton scatter off the hot ICM electrons, the Sunyaev-Zeldovich (SZ) effect. The SZ effect does not depend on redshift, and with the instruments planned or underway, SZ surveys may become a powerful method of detecting clusters (see Carlstrom, Holder, & Reese 2002 for a review).

Recent X-ray studies of the evolution of the abundance of clusters generally find $0.1 < \Omega_m < 0.6$ and $0.6 < \sigma_8 < 0.9$ for a flat ΛCDM cosmology and including the statistical and systematic uncertainties (e.g., Henry 2004; Vikhlinin et al. 2003; Borgani et al. 2001; Henry 2000; Donahue & Voit 1999; Eke et al. 1998). For a review of X-ray surveys and the evolution of the number density of clusters see Rosati et al. (2002). Studies based on the assumption of a constant gas mass fraction find similar results (Ettori et al. 2003; Allen et al. 2003). More precise cosmological constraints will require a better understanding of the complex physical processes in clusters including heating mechanisms, cooling, and the effects of mergers. With their improved spatial and spectral resolution, *Chandra* and *XMM-Newton* are revolutionizing our view of cluster physics. Observations with these observatories combined with the incorporation of new physical process in numerical simulations will lead to a significant reduction in the systematic uncertainties.

1.3 Cluster Structure

A third method of constraining cosmological models with clusters is through the amount of substructure they contain (Richstone, Loeb, and Turner 1992). Clusters form and grow through mergers with other clusters and groups. These mergers are

observed as multiple peaks in the cluster density distribution or as disturbed cluster morphologies. The cluster relaxation time is relatively short, on the order of a Gyr, and the fraction of unrelaxed clusters should reflect their formation rate. The formation epoch of clusters depends on both Ω_m and Λ, so the amount of substructure in clusters in the present epoch and how quickly it evolves with redshift depend on these parameters. In low density universes, clusters form earlier and will be on average more relaxed at low redshift. Clusters at high redshift, closer to the epoch of cluster formation, should be on average dynamically younger and show more structure.

This method does not currently place as tight constraints on the matter density as those described in the previous section, but this situation will improve with larger samples and higher resolution numerical simulations. In addition to probing cluster formation and evolution, a quantitative measurement of cluster substructure is important to constrain systematic biases in observed cluster properties, particularly those used to estimate mass. The calculation of cluster masses and gas mass fractions generally assume that clusters are spherical or elliptical, roughly isothermal, and in hydrostatic equilibrium. These conditions are clearly not true during a merger. Hydrodynamic simulations of clusters have shown that mergers can lead to large deviations in a cluster's X-ray temperature and luminosity (Randall et al. 2002; Ritchie & Thomas 2002; Mathiesen & Evrard 2001). Based on the boosts in temperature and luminosity in their simulated mergers, Randall et al. (2002) show that fits to the X-ray temperature function (XTF) or X-ray luminosity function of massive clusters can lead to overestimates of σ_8 by 20%. Ω_m was also underestimated in the fits based on the XTF. On the observational side, Smith et al. (2003) find that for a sample of 10 lensing clusters at $z \simeq 0.2$ the unrelaxed clusters are 30% hotter than the relaxed clusters.

There are also indications that the optical and X-ray properties of clusters diverge at high-redshift, a situation that is quite possibly related to cluster structure. I have been involved in a project to follow-up high-redshift clusters from the Red-Sequence Cluster Survey (RCS) with *Chandra*. RCS is an optical survey that uses the color-magnitude relationship of cluster galaxies to identify moderate to high-redshift clusters (Gladders & Yee 2000). We find that these clusters have lower luminosities and, where measurable, lower temperatures than expected from their optical richness (Yee & Ellingson 2003). One possibility is that these high-redshift clusters are in the process of forming. The galaxies are basically in place, but the cluster has not yet virialized. The observed optical richness may also come from several structures along the line of sight that have not yet merged to form a single cluster. Lubin, Mulchaey, & Postman (2004) found a similar result; they observe two optically-selected high-redshift clusters with *XMM-Newton* and find that their X-ray luminosities and temperatures are low for their velocity dispersions. The nature of these clusters and the evolution of the relationship of optical and X-ray observables needs to be understood before these clusters can be used as cosmological tools, and the evolution of cluster structure may shed light on this situation.

1.4 Outline of this Thesis

In this thesis, I pursue the goal of studying cosmology with galaxy clusters through both one of the most detailed X-ray observations of a high-redshift cluster ever performed and the first study of cluster structure and the frequency of cluster mergers over a large redshift range.

In Chapter 2, I examine the *Chandra* observation of the high-redshift cluster MS1054-0321. This cluster is the highest redshift cluster in the *Einstein* Medium Sensitivity Survey (EMSS) at $z = 0.83$, and it is one of the most massive high-redshift clusters known. The observation of MS1054-0321 in the EMSS alone constrains Ω_m to be less than one (Jeltema et al. 2001; Donahue et al. 1998). MS1054-0321 also shows distinct substructure which I confirm and examine in detail for the first time with the *Chandra* observation. This study was one of the first studies of a high-redshift cluster with the *Chandra Observatory*.

In Chapter 3, I investigate for the first time the observed evolution of cluster structure with redshift out to $z \sim 1$. To quantify cluster morphology, I use the power ratio method developed by Buote & Tsai (1995). Power ratios are constructed from moments of the two-dimensional gravitational potential and are, therefore, related to a cluster's dynamical state. My sample includes 40 clusters selected from the *Chandra* archive with redshifts between 0.1 and 0.9. I divide these into high and low-redshift subsamples and compare their average power ratios.

Bibliography

[1] Allen, S.W., Schmidt, R.W., Fabian, A.C., & Ebeling, H. 2003, MNRAS, 342, 287

[2] Borgani, S., Rosati, P., Tozzi, P., Stanford, S.A., Eisenhardt, P.R., Lidman, C., Holden, B., Della Ceca, R., Norman, C., & Squires, G. 2001, ApJ, 561, 13

[3] Buote, D.A., & Tsai, J.C. 1995, ApJ, 452, 522

[4] Burles, S., Nollett, K.M., Turner, M.S. 2001, ApJ, 552, L1

[5] Carlstrom, J.E., Holder, G.P., Reese, E.D. 2002, ARA&A, 40, 643

[6] Donahue, M., Voit, G.M., Gioia, I., Luppino, G., Hughes, J.P., & Stocke, J.T. 1998, ApJ, 502, 550

[7] Donahue, M. & Voit, G.M. 1999, ApJ, 523, L137

[8] Eke, V.R., Cole, S., Frenk, C.S., & Henry, J.P. 1998, ApJ, 419, L9

[9] Ettori, S., Tozzi, P., & Rosati, P. 2003, A&A, 398, 879

[10] Gladders, M.D., & Yee, H.K.C. 2000, AJ, 120, 2148

[11] Henry, J.P. 2000, ApJ, 534, 565

[12] Henry, J.P. 2004, ApJ, accepted, astro-ph/0404142

[13] Jeltema, T.E., Canizares, C.R., Bautz, M.W., Malm, M.R., Donahue, M., & Garmire, G.P. 2001, ApJ, 562, 124

[14] Kirkman, D., Tytler, D., Suzuki, N., O'Meara, J.M., & Lubin, D. 2003, ApJS, 149, 1

[15] Lubin, L.M., Mulchaey, J.S., & Postman, M. 2004, ApJ, 601, L9

[16] Mathiesen, B.F., & Evrard, A.E. 2001, ApJ, 546, 100

[17] Perlmutter, S., et al. 1999, ApJ, 517, 565

[18] Randall, S.W., Sarazin, C.L., & Ricker, P.M. 2002, ApJ, 577, 579

[19] Richstone, D., Loeb, A., & Turner, E.L. 1992, ApJ, 393, 477

[20] Riess, A.G., et al. 1998, AJ, 116, 1009

[21] Ritchie, B.W., & Thomas, P.A. 2002, MNRAS, 329, 675

[22] Rosati, P., Borgani, S., & Norman, C. 2002, ARA&A, 40, 539

[23] Rubiño-Martin, J.A., et al. 2003, MNRAS, 341, 1084

[24] Sievers, J.L., et al. 2003, ApJ, 591, 599

[25] Smith, G.P., Edge, A.C., Eke, V.R., Nichol, R.C., Smail, I., & Kneib, J.-P. 2003, ApJ, 590, L79

[26] Spergel, D.N., et al. 2003, ApJS, 148, 175

[27] Vikhlinin, A., Voevodkin, A., VanSpeybroeck, L., Quintana, H., McNamara, B.R., Gioia, I., Hornstrup, A., Henry, J.P., Forman, W.R., & Jones, C. 2003, ApJ, 590, 15

[28] White, S.D.M., Navarro, J.F., Evrard, A.E., & Frenk, C.S. 1993, Nature, 366, 429
[29] Wittman, D., Margoniner, V.E., Tyson, J.A., Cohen, J.G., Dell'Antonio, I.P., & Becker, A.C. 2003, ApJ, 597, 218
[30] Yee, H.K.C., & Ellingson, E. 2003, ApJ, 585, 215

Chapter 2

Chandra X-Ray Observatory Observation of the High-Redshift Cluster MS 1054−0321

Most of this chapter was published in Jeltema, T.E., Canizares, C.R., Bautz, M.W., Malm, M.R., Donahue, M., & Garmire, G.P. 2001, ApJ, 562, 124.

2.1 Introduction

Clusters of galaxies are the largest and most recently virialized objects in the universe. Massive clusters represent the extreme end of the distribution of initial density perturbations and are, therefore, extremely sensitive to the density parameter Ω_m. If $\Omega_m = 1$, the number density of clusters evolves quickly with redshift, and massive clusters must have formed recently (Carlberg et al. 1997). However, for a low density universe ($\Omega_m < 1$), the evolution with redshift is much slower, and massive clusters must form early to account for their present number density. The existence of massive clusters at high redshift, therefore, places strong constraints on Ω_m. The virial mass of a cluster can be related to its X-ray temperature, and so Ω_m can be constrained through the evolution of cluster temperature with redshift (Oukbir & Blanchard 1992; Donahue & Voit 1999; Eke, Cole, & Frenk 1996).

In this paper, we present the *Chandra* X-ray Observatory observation of MS1054-0321, the highest redshift cluster in the Einstein Extended Medium Sensitivity Survey (EMSS; Gioia et al. 1990; Henry et al. 1992) with z = 0.83. This cluster has previously been observed at X-ray wavelengths with *ASCA* and *ROSAT*. Its mass has been estimated from the *ASCA* X-ray temperature of $12.3^{+3.1}_{-2.2}$ keV (Donahue et al. 1998, hereafter D98), from β-model fits to the *ROSAT/HRI* data (Neumann & Arnaud 2000, hereafter NA00), and, at optical wavelengths, from its weak lensing signal (Hoekstra, Franx, & Kuijken 2000; Luppino & Kaiser 1997) and observed velocity dispersion (Tran et al. 1999). All of these methods indicate that MS1054 is a massive cluster, which in conjunction with its high redshift implies $\Omega_m < 1$. Substructure, an indication that the cluster may not be completely relaxed, was

seen in both the *ROSAT/HRI* observation and the weak lensing data (D98; NA00; Hoekstra et al. 2000).

Using *Chandra*, we make a more accurate temperature determination. We also examine in greater detail the substructure in the X-ray distribution. Lastly, we estimate the mass and velocity dispersion of MS1054 and investigate the constraints this cluster places on an $\Omega_m = 1$ universe. Throughout the paper, we use $H_0 = 100h$ km s^{-1} Mpc^{-1}. For $q_0 = 0.5$ and $\Lambda = 0$, one arcminute is 249 h^{-1} kpc at the cluster's redshift.

2.2 Observation Preparation

Chandra observed MS1054 with the back-illuminated ACIS-S3 detector on 2000 April 21-22 for 91 ks. To create a clean "events file" for analysis, we kept only *ASCA* grades 0, 2, 3, 4, and 6[1]. We then examined the satellite aspect and light curve to eliminate time intervals of bad aspect or high background. The net useful exposure time was then 88 ks. The spectral analysis was limited to the 0.8-7 keV range. Point sources were detected using *wavdetect*, a wavelet source detection program in the *Chandra* Interactive Analysis of Observations Software (CIAO), with a significance threshold of 10^{-6}. Twenty-three sources were removed from the data. For fitting, all spectra were extracted in PI (pulse height-invariant) channels, which correct for the gain difference between different regions of the CCD, and grouped to give a minimum of 20 counts per energy bin. The background was estimated from the local background on the ACIS-S3 chip. The net cluster count rate was 0.13 counts s^{-1} in a 2′ radius region and in the 0.3-7.0 keV band. Spectra were analyzed using XSPEC (v11.0.1). We generally used redistribution matrix (RMF) and ancillary response (ARF) files based on the center of a given spectrum's extraction region. Choosing RMFs and ARFs for different points in the cluster did not significantly affect our fits.

2.3 Analysis

2.3.1 Cluster Properties

In order to find the overall cluster temperature, a spectrum was extracted from a 1.5′ (374 h^{-1} kpc) radius circular aperture surrounding the cluster. The cluster center was taken to be R.A.(2000) = $10^h56^m58^s.6$ and decl.(2000) = $-03°37'36''.7$, which corresponds to the best-fit center from NA00. The spectrum was fit with a Raymond-Smith thermal plasma model (Raymond & Smith 1977; updated to 1992 version) with foreground absorption. The absorption was fixed at the galactic value of 3.6×10^{20} atoms cm^{-2} (Dickey & Lockman 1990), the redshift was fixed at 0.83, and the iron abundance and temperature were free to vary. The best-fit temperature is $10.4^{+1.7}_{-1.5}$ keV[2]

[1] *Chandra* Proposers' Observatory Guide http://asc.harvard.edu/udocs/docs/docs.html, section "Technical Description", subsection "ACIS"

[2] Using new calibration files released for the *Chandra* data after this project was completed, the cluster temperature is $7.4^{+1.4}_{-0.9}$ keV. See the notes at the end of this chapter.

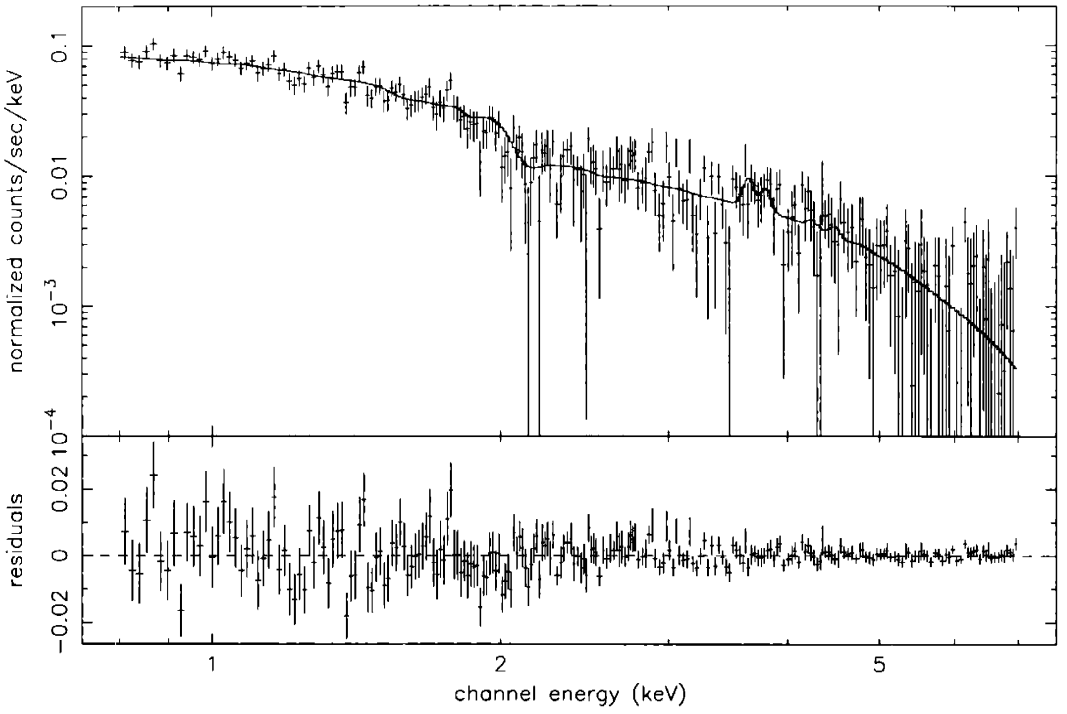

Figure 2-1 X-ray spectrum and residuals for MS1054-0321. The spectrum was binned so that there were a minimum of 20 counts per energy bin. *Solid line:* Best-fit model.

with an abundance of 0.26 ± 0.15 relative to the abundances of Anders & Grevesse (1989). The quoted uncertainties are 90% confidence levels for the two free parameters. MS1054 has a bolometric luminosity of 1.2×10^{45} h^{-2} ergs s^{-1} and a luminosity in the 2-10 keV band of 6.3×10^{44} h^{-2} ergs s^{-1} ($q_0 = 0.1$). The detection of the iron emission line allows us to fit for the redshift, which gives $z = 0.83 \pm 0.03$. Using a mekal model instead of a Raymond-Smith model did not affect these results, and the intrinsic cluster absorption was consistent with zero.

Figure 1 shows the binned spectrum and best fit folded model. The fit is good with a reduced χ^2 of 1.03 for 239 degrees of freedom. Figure 2 shows the χ^2 contours for the iron abundance versus cluster temperature.

The best fit cluster temperature from the *Chandra* data is somewhat lower than the *ASCA* temperature of $12.3^{+3.1}_{-2.2}$ keV (D98). However, the two results agree within the 90% limits, and there is no statistically significant discrepancy. In addition, the *ASCA* results could be affected by point sources that *ASCA* could not resolve. For a 2′ radius region around the cluster including point sources, we find a best fit temperature of $11.4^{+2.5}_{-1.7}$ keV.

We also investigated the variation of temperature with radius by extracting spectra in five concentric annuli. Annuli were required to have at least 2000 counts above background, which could only be achieved out to a radius of 1.14′. We do not find a significant temperature gradient. The best-fit temperatures vary between annuli by over 2 keV. However, all temperatures overlapped at the 90% confidence level. A plot

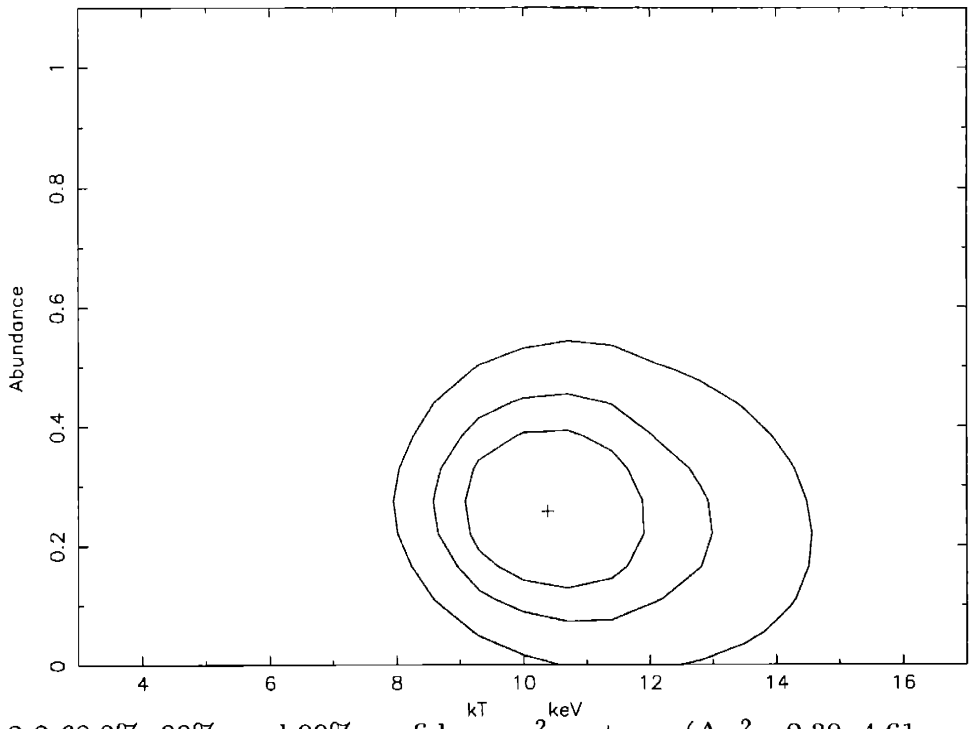

Figure 2-2 68.3%, 90%, and 99% confidence χ^2 contours ($\Delta\chi^2$ =2.30, 4.61, and 9.21) for the cluster iron abundance and temperature.

of temperature as a function of radius is shown in Figure 3.

2.3.2 Substructure

The *Chandra* image of MS1054, including the point sources, is shown in Figure 4. The image has been adaptively smoothed using the CIAO program *csmooth* with a minimum significance of 3 and a maximum significance of 5. The existence of substructure is evident as two distinct peaks can be seen in the X-ray image separated by about 1.2′ (300 h^{-1} kpc). Figure 5 shows a Hubble Space Telescope WFPC2 I-band mosaic (F814W) of the cluster assembled from the HST archive (for a discussion of the HST data see van Dokkum et al. 2000) with our X-ray contours overlaid. In the HST image, MS1054 appears as an extended string of galaxies. There are several galaxies centered on the eastern X-ray peak, including the central cD galaxy. However, the western peak appears to have galaxies lining its southern edge rather than at the center.

We investigated the temperature of each of these clumps separately, taking spectra in a 0.41′ radius circle around the brightest pixel in each clump. The eastern clump was taken to be centered at R.A.(2000) = $10^h57^m0^s.2$ and decl.(2000) = $-03°37'39''.6$, and the western peak center was R.A.(2000) = $10^h56^m55^s.6$ and decl.(2000) = $-03°37'42''.5$. The spectra were again fit with a Raymond-Smith model with the absorbing N_H fixed at 3.6×10^{20} cm^{-2}, the redshift fixed at 0.83, and the iron abundance and temperature free to vary.

For the eastern clump, the best fit temperature is $10.5^{+3.4}_{-2.1}$ keV with a reduced

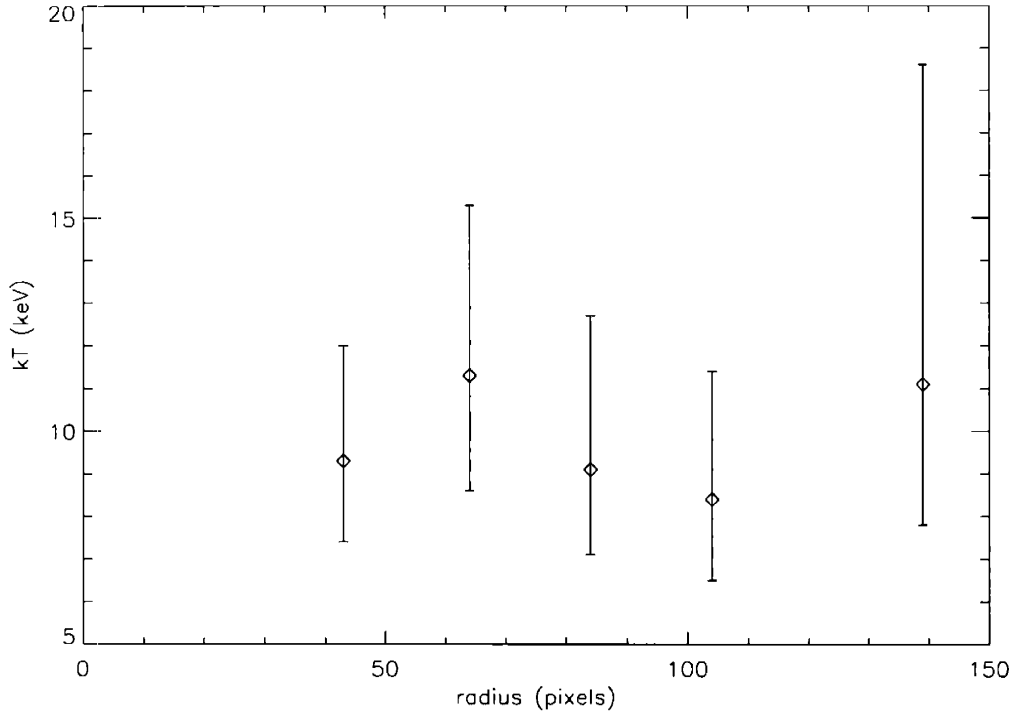

Figure 2-3 X-ray temperature as a function of radius. Temperatures were determined in concentric annuli, and the radius plotted is the outer radius of each annulus. The temperature error bars give the 90% confidence limits. 1 pixel = $2''.03$ = 2.04 h^{-1} kpc.

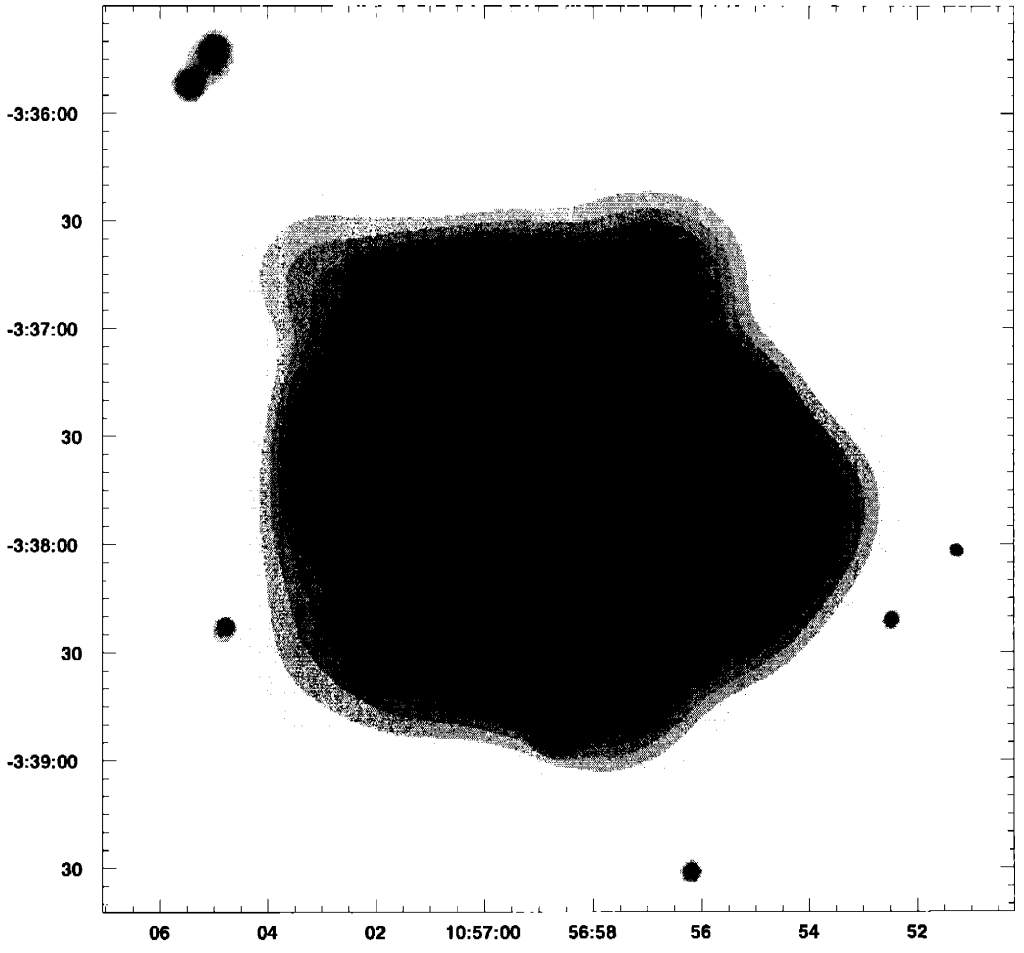

Figure 2-4 Smoothed *Chandra* image of MS1054. The image was smoothed with the CIAO program *csmooth*.

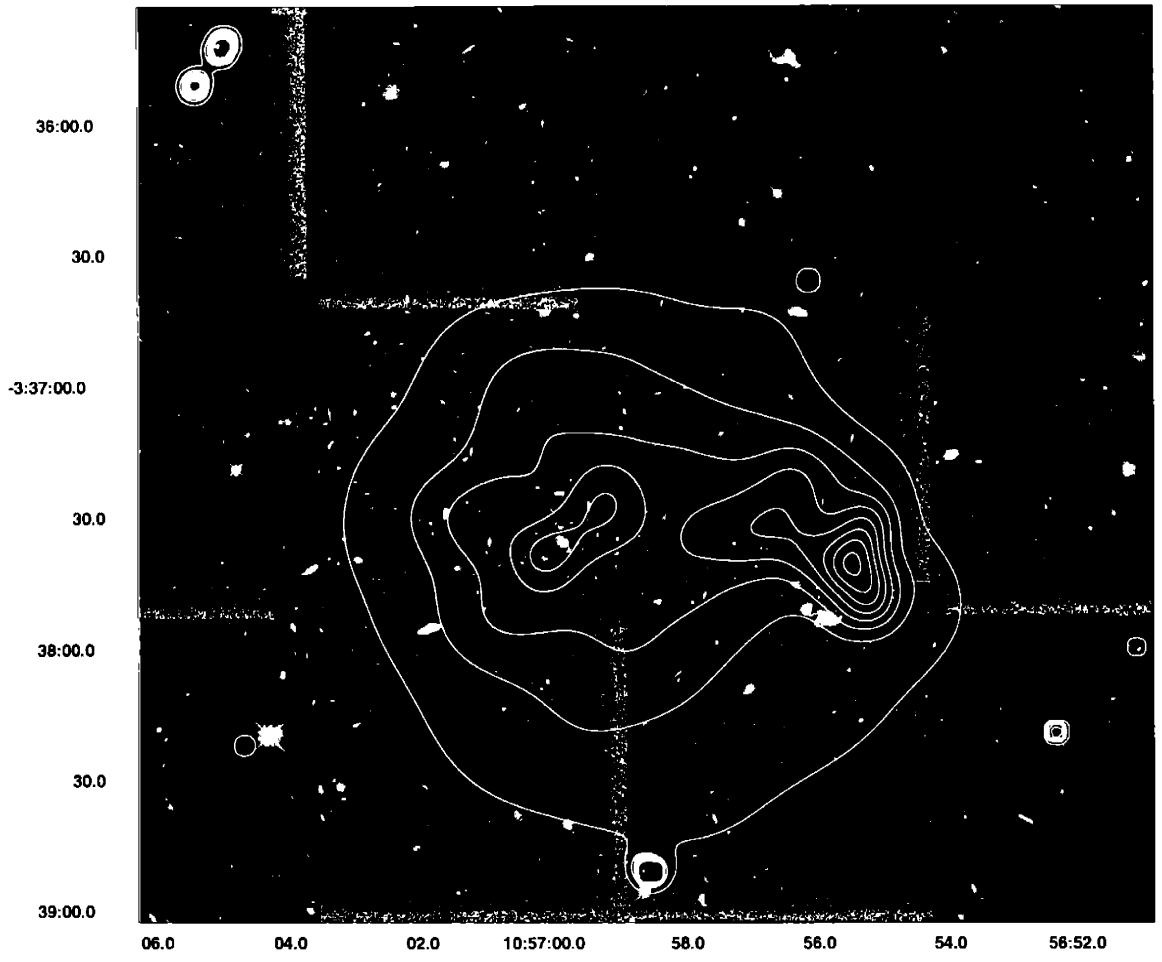

Figure 2-5 Hubble I-band mosaic of MS1054 with contours from the smoothed X-ray image overlaid. Contours are evenly spaced from 0 to 1 by 0.10.

χ^2 of 0.94 for 75 degrees of freedom. This temperature agrees well with the overall cluster temperature. For the western clump, the temperature is $6.7^{+1.7}_{-1.2}$ keV with a reduced χ^2 of 1.08 for 62 degrees of freedom. The eastern clump is somewhat hotter than the western clump, with the lower limit of the 90% confidence range for the eastern clump temperature just equaling the upper limit for the western clump. The spectra and best fit folded models are shown in Figure 6. We find the iron abundances of the eastern and western clumps to be $0.08^{+0.23}_{-0.08}$ and $0.46^{+0.27}_{-0.26}$ respectively, which are consistent with each other and with the value 0.26 ± 0.15 derived for the whole cluster. Figure 7 shows the abundance versus temperature contours for both clumps.

Within a radius of $0.41'$, the two clumps have similar luminosities. The eastern clump luminosity is 1.4×10^{44} h^{-2} ergs s^{-1} (2-10 keV) and 2.6×10^{44} h^{-2} ergs s^{-1} bolometric, and for the western clump the luminosity is 1.0×10^{44} h^{-2} ergs s^{-1} (2-10 keV) and 1.7×10^{44} h^{-2} ergs s^{-1} bolometric ($q_0 = 0.1$). The western clump has a higher central surface brightness, but is also more compact. The eastern clump is comparatively diffuse, whereas the western clump is smaller and denser.

To get an indication of temperature variations in the cluster, we created a map of the hardness ratio. First, we made hard (1.5-7 keV) and soft (0.3-1.5 keV) band images, smoothing each using *csmooth* and the output smoothing scales, the kernel size at which the signal to noise is greater than three, from the full band image in Figure 4. From each image we subtracted the background in the appropriate energy band. We also discarded pixels with less than twice the background to reduce inaccuracies near the edge of the cluster where we have few counts. Finally, the hard band image was divided by the soft band image. This hardness ratio map is shown in Figure 8. Lighter colors correspond to a higher hardness ratio and may indicate higher temperatures. The full band contours are overlaid on the image. The eastern clump does appear to have a higher hardness ratio and, therefore, a higher temperature than the western clump. There does not appear to be a shock between the two clumps. Indeed, the interclump region is cooler than the cluster as a whole.

Substructure in MS1054 was seen previously in the *ROSAT/HRI* observation, which has lower resolution than *Chandra* (NA00, D98). NA00 also find two components and identify the eastern clump as the main cluster component. Indeed, our position of the eastern clump is quite close to the central cD galaxy which has R.A.(2000) = $10^h56^m59^s.9$ and decl.(2000) = $-03°37'37''.3$ (D98). The western clump could either be a subgroup falling into the cluster or a foreground group of galaxies. Since we detect an iron line, we fit for the redshift of the western clump in XSPEC and get a value of $z = 0.84 \pm 0.02$, which agrees well with the redshift of the cluster.

Substructure can also be seen in the weak lensing analysis of the optical data. In their weak lensing study, Hoekstra, Franx, & Kuijken (2000) find three clumps in the mass distribution that all appear to have similar masses. An approximate overlay of the *Chandra* X-ray contours on their weak lensing mass reconstruction is shown in Figure 9. Their central and western clumps seem to correspond to our eastern and western clumps. However, we do not detect the north-eastern weak lensing clump. This result was noted by Clowe et al. (2000) when they overlaid the *ROSAT/HRI* contours on the Keck weak lensing data. It is possible that this third peak is not as fully collapsed as the other two and, therefore, is not yet visible in

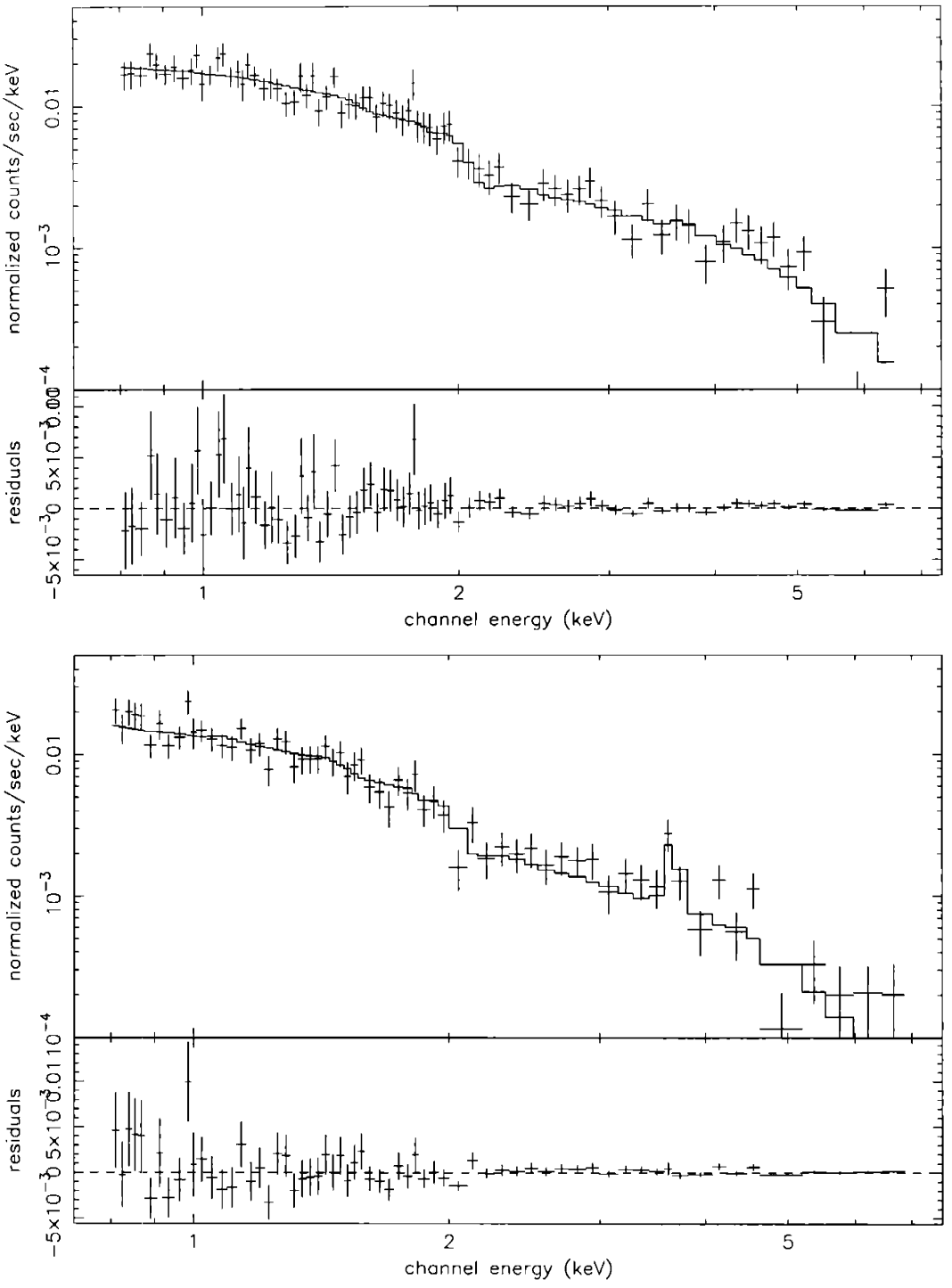

Figure 2-6 X-ray spectrum and residuals for a 0.41′ radius circle around the (a) eastern peak and (b) western peak. *Solid line:* Best-fit model.

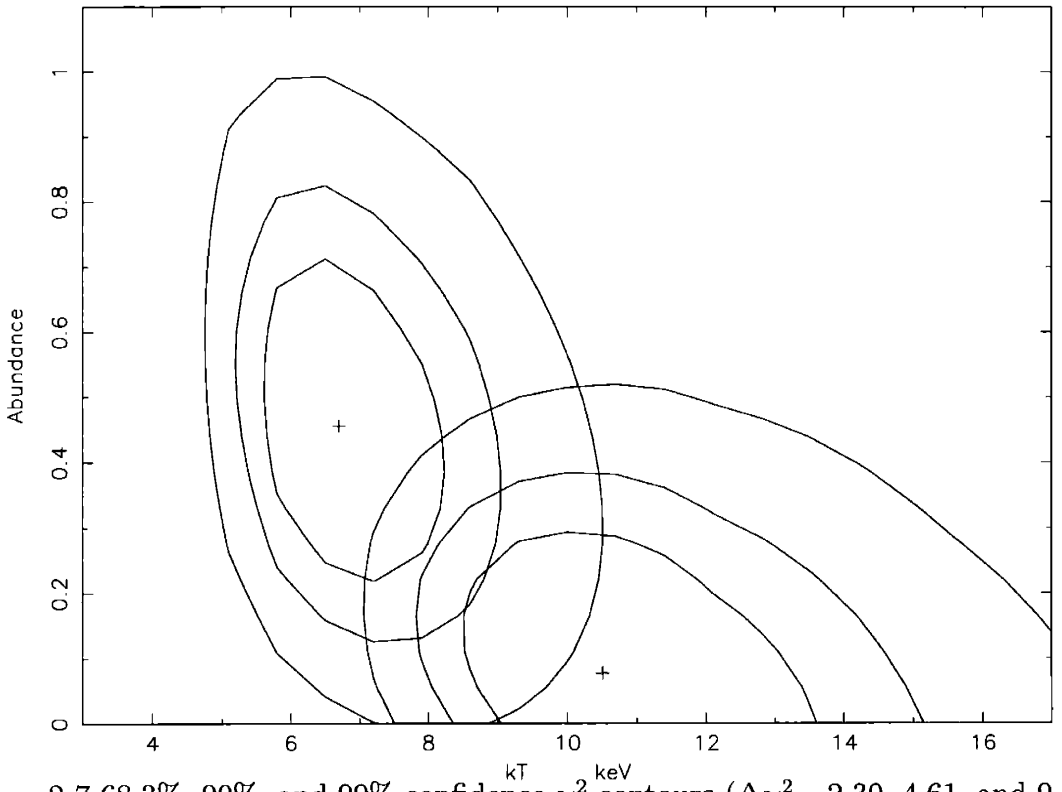

Figure 2-7 68.3%, 90%, and 99% confidence χ^2 contours ($\Delta\chi^2$ =2.30, 4.61, and 9.21) for the iron abundance and temperature of the eastern and western peaks. The eastern peak contours are centered at kT= 10.5 keV and an abundance of 0.08. The western peak contours are centered at kT= 6.7 keV and an abundance of 0.46.

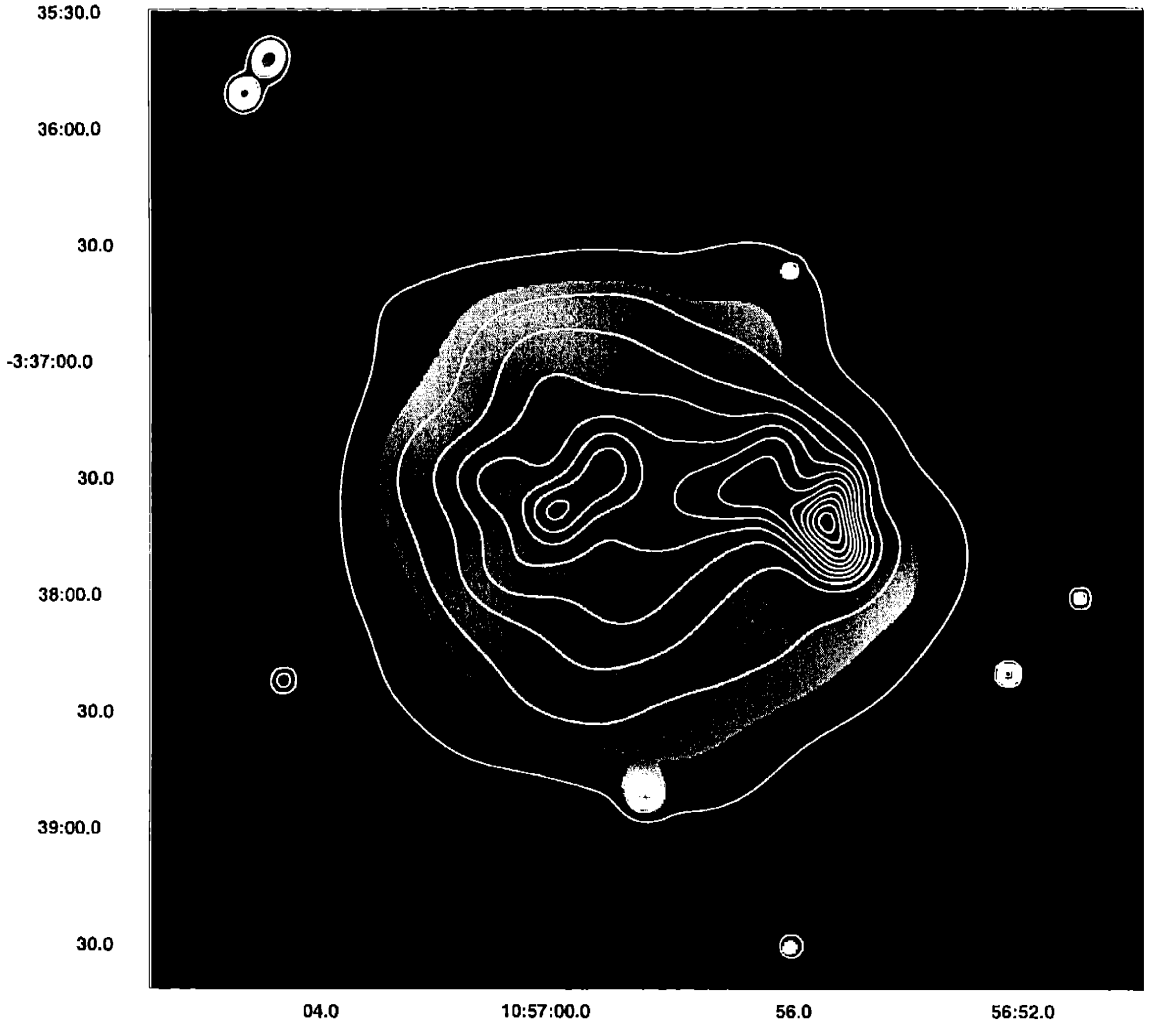

Figure 2-8 Hardness ratio map with full band contours overlaid. The smoothed hard band (1.5-7 keV) image was divided by the smoothed soft band (0.3-1.5 keV) image after taking out pixels with less than twice the background. Lighter colors correspond to a higher ratio. Contours are evenly spaced from 0 to 1 by 0.067.

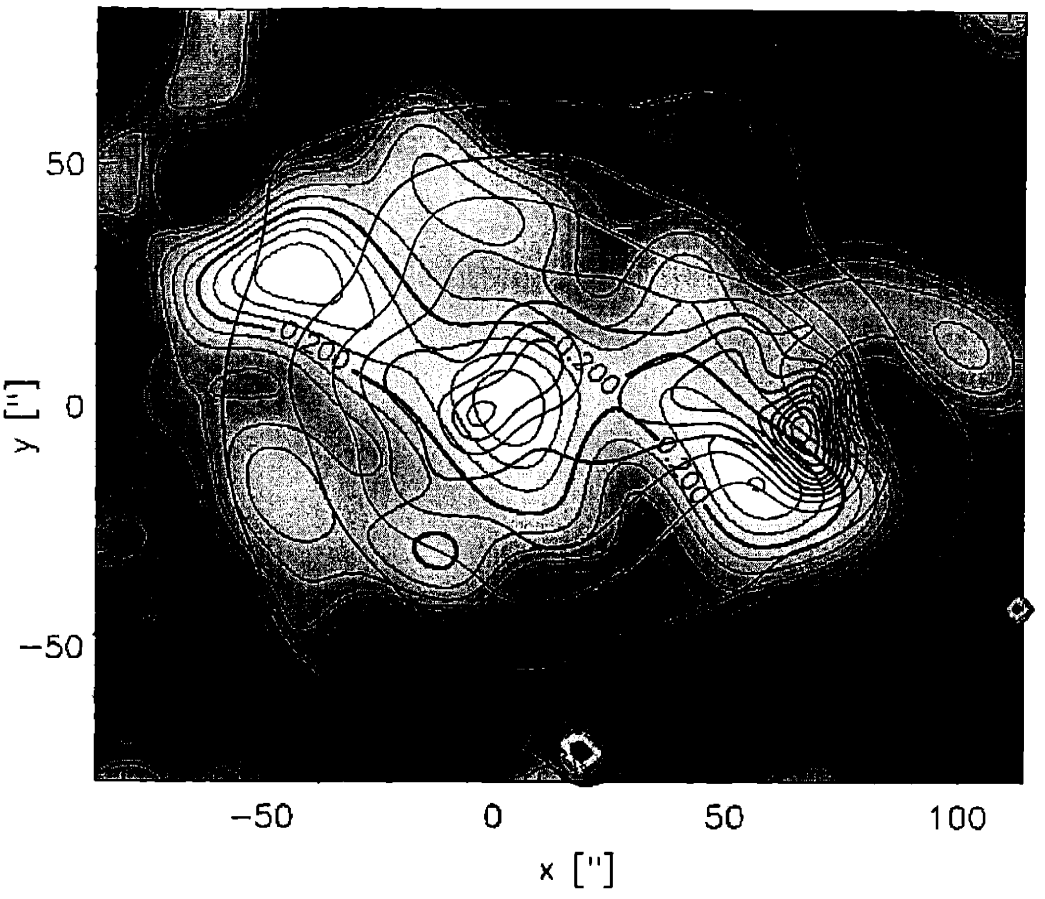

Figure 2-9 Weak lensing mass reconstruction from Hoekstra et al. (2000) overlaid with the X-ray contours. The position of the contours with respect to the mass profile is approximated, but relative positions are good to within 3″. The origin corresponds to the central cD galaxy, and negative x values indicate east of this origin.

X-rays. Alternatively, reanalysis of the weak lensing data shows that the details of the substructure are not well constrained by the data (Marshall et al. 2002).

We used the galaxy redshifts published in Tran et al. (1999) to estimate the mean velocity of each of the three weak lensing clumps. For the north-eastern, central, and western clumps the mean velocities and one sigma errors are $161,700 \pm 280$ km s^{-1}, $162,600 \pm 410$ km s^{-1}, and $162,300 \pm 350$ km s^{-1} respectively. The difference in the velocities of the unseen north-eastern peak and central peak is 900 ± 690 km s^{-1}, indicating that a significant relative velocity is possible but not required by the limited data (6-7 galaxies per clump).

In the HST image, MS1054 has a filamentary appearance. It is possible that this cluster is in reality a series of clumps along a filament that are in the process of merging. The clear separation of the two X-ray peaks indicate that the cluster is most likely in a pre-merger state. When considering the overlay of the X-ray contours

on both the Hubble mosaic and the weak lensing mass map it appears that both the cluster galaxies and mass associated with the western subclump lie below the X-ray peak. This leads to the interesting possibility that the gas in the subclump is being stripped off as it falls into the cluster.

In light of this cluster's complicated structure using a spherical, hydrostatic, isothermal model may lead to errors in estimating the mass. To get an indication of these errors, we turn to cluster simulations. Simulations show that mergers can introduce large errors in mass estimates using X-ray properties, but generally produce underestimates (Mathiesen & Evrard 2001; Evrard, Metzler, & Navarro 1996; Roettiger, Burns, & Loken 1996; Schindler 1996). In section 4, we estimate the virial mass of the cluster using a scaling relation between the mass and X-ray temperature. Scaling relations between cluster virial mass and temperature are normalized through cluster simulations and use either a mass weighted or emission weighted temperature. These temperatures are not necessarily the same as the spectral temperature obtained from observations.

Recently, Mathiesen & Evrard (2001) have used simulations to investigate the relationship between these three temperatures. As they note, one might expect that a subclump containing cooler gas would cause an underestimation of the cluster temperature and mass, whereas a shock containing hotter gas would cause an overestimate of these properties. However, the larger effect will be due to the subclump which is more massive and luminous than the gas in the shock, and mergers will lead to an underestimate of the mass. Indeed, they find that the spectrally determined temperatures are nearly always lower than both the emission and mass-weighted temperatures with typical errors of 10-20%. In the case of the mass-weighted temperature they show that all large underestimates of the temperature occur close to a merger. We conclude that if MS1054 is not in hydrostatic equilibrium, then we should underestimate its mass. This only strengthens our conclusions about Ω_m.

2.3.3 Point Sources

We resolve nine point sources within a 3′ radius of the cluster center. From a search of the NASA/IPAC Extragalactic Database (NED), one of these corresponds to LCRS B105416.2−032123, which is an AGN detected at radio frequencies with a redshift of 0.2. Our position for this source is R.A.(2000) = $10^h56^m48^s.7$ and decl.(2000) = $-03°37'27''.4$, and the NED quoted position is R.A.(2000) = $10^h56^m48^s.8$ and decl.(2000) = $-03°37'26''$. One of the other sources is in the vicinity of one of the MS1054 galaxies used by D98 in studying the velocity dispersion, R.A.(2000) = $10^h56^m52^s.5$ and decl.(2000) = $-03°38'21''.5$ compared to NED of R.A.(2000) = $10^h56^m53^s.3$ and decl.(2000) = $-03°38'16''$. The remaining sources do not seem to have any obvious NED counterparts.

Chapman et al. (2002) report a SCUBA source, SMMJ 10571-0337, near MS1054. This source has a 850 μm flux of 15mJy, but is not detected by *Chandra*. Based on our non-detection of this source, we estimate the upper limit on its flux in the 2-7 keV range to be 1.3×10^{-15} ergs cm^{-2} s^{-1}.

The point source closest to the cluster is centered at R.A.(2000) = $10^h56^m58^s.7$

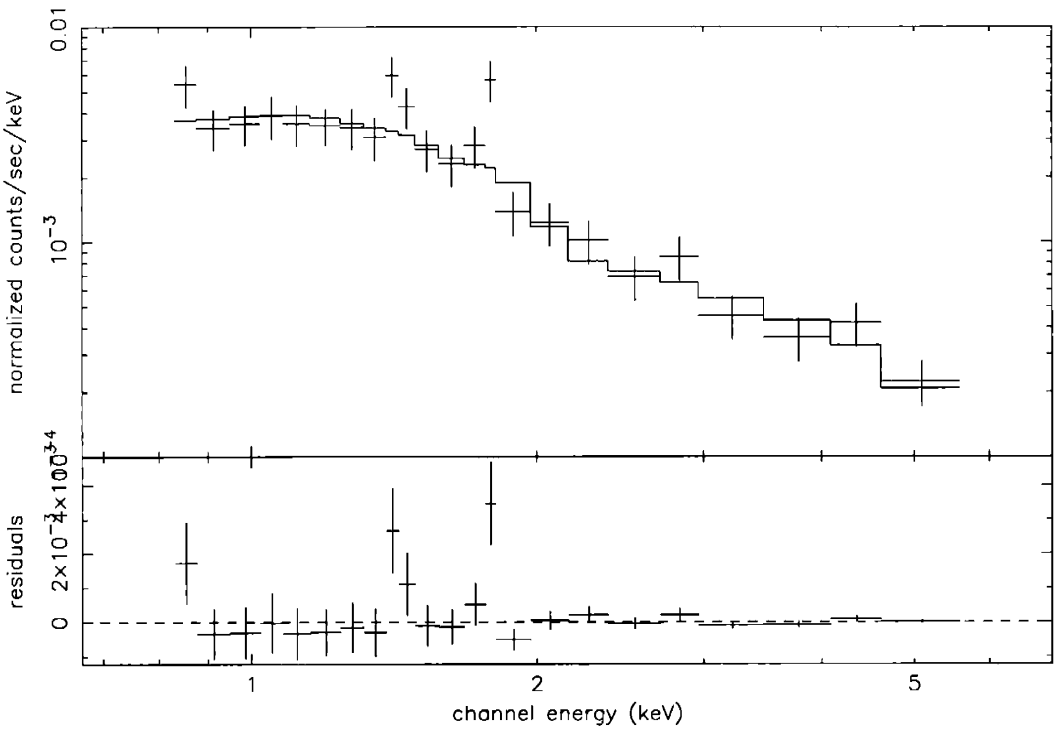

Figure 2-10 X-ray spectrum and residuals for the point source centered at R.A.(2000) = $10^h56^m58^s.7$ and decl.(2000) = $-03°38'53''.5$. The spectrum was binned so that there were a minimum of 20 counts per energy bin. *Solid line:* Best-fit model.

and decl.(2000) = $-03°38'53''.5$ and was seen in the *ROSAT* image as a small southern extension to the cluster. Fitting to an absorbed power law, gives $N_H = 2.2^{+1.8}_{-1.4} \times 10^{21}$ atoms/cm^2, and photon index 1.7±0.3, with a reduced χ^2 of 1.26 for 20 degrees of freedom. This photon index is typical of a Seyfert I type AGN. The binned spectrum and folded model are shown in Figure 10. The flux of this source is approximately 3.1×10^{-14} ergs cm^{-2} s^{-1} (2-7 keV). Although this object was not found in the NED database, there is a small object in the HST image that may correspond to it.

2.4 Cluster Mass and Velocity Dispersion

Using the X-ray temperature, $10.4^{+1.7}_{-1.5}$ keV, we can estimate both the velocity dispersion and mass of MS1054 and compare them to the optical results. From the *Chandra* temperature the implied velocity dispersion is $(kT_X/\mu m_p)^{1/2} = 1289^{+102}_{-96}$ km s^{-1}. This agrees well with the observed velocity dispersion of 1170 ± 150 km s^{-1} (Tran et al. 1999) and the velocity dispersion derived from weak lensing of 1311^{+83}_{-89} km s^{-1} (Hoekstra et al. 2000).

The virial mass of the cluster can be estimated for $\Omega_m = 1$ by assuming that the mean density in the virialized region is ~200 times the critical density at the cluster's redshift and that the cluster is isothermal (Evrard et al. 1996, Hjorth, Oukbir, & van Kampen 1998, D98). From the simulations of Evrard et al. (1996), the mass-

temperature relation for the mass within a region whose density is 200 times the critical density is

$$M_{vir} \approx (1.45 \times 10^{15} h^{-1} M_{\odot}) \Big(\frac{1}{1+z}\Big)^{3/2} \Big(\frac{kT_X}{10keV}\Big)^{3/2} \tag{2.1}$$

(Arnaud & Evrard 1999). This scaling law method of estimating the mass of clusters is more accurate than estimates derived from a β-model fit to the surface brightness because the scaling law has a smaller variance and is less sensitive to the cluster's dynamical state. However, the scaling law method depends on the normalization of the M-T relation which is derived from cluster simulations (Evrard et al. 1996). Bryan & Norman (1998) compare the normalizations from several cluster simulation studies and find that the scatter in normalizations is small, similar to the scatter of clusters around the M-T relation. We use the relation given by Evrard et al. (1996) because it gives the smallest mass. As we noted before, we expect to underestimate the mass due to the presence of substructure and this can only strengthen our conclusions in the following section.

From the *Chandra* temperature, the virial mass is approximately $6.2^{+1.6}_{-1.3} \times 10^{14} h^{-1} M_{\odot}$ within $r_{200} = 0.76 h^{-1}$ Mpc. The errors here represent the errors in the temperature. This mass is somewhat lower than those derived from weak lensing, $M(\leq 0.87 h_{50}^{-1} Mpc) = 1.2 \pm 0.2 \times 10^{15} h_{50}^{-1} M_{\odot}$, and the observed velocity dispersion, $M(\leq 1 h^{-1} Mpc) = 1.9 \pm 0.5 \times 10^{15} h^{-1} M_{\odot}$ (Hoekstra et al. 2000; Tran et al. 1999). Assuming $M \propto R$ in order to compare with our mass, these masses are approximately $M(\leq 0.76 h^{-1} Mpc) = 1.0 \pm 0.2 \times 10^{15} h^{-1} M_{\odot}$ and $M(\leq 0.76 h^{-1} Mpc) = 1.4 \pm 0.4 \times 10^{15} h^{-1} M_{\odot}$ respectively.

Another method of estimating the mass comes from fitting a beta-model to the observed surface brightness. The radial surface brightness profile is modeled as $S = S_0 (1 + r^2/r_c^2)^{-3\beta+0.5}$ where r_c is the core radius. The background subtracted radial surface brightness profile is shown in Figure 11. Attempts to fit to a β-model failed because the best fit was obtained for unreasonably large values of β and the core radius. This behavior was also noted in NA00 for the *ROSAT/HRI* data. NA00 found that if they removed the western substructure they could get a good fit to a β-model; however, we were not able to get a reasonable fit even with the western clump removed. In their simulated clusters, Bartelmann & Stienmetz (1996) find that they get more accurate masses by constraining β to be one and fitting for the core radius, though their masses are still biased low by about 10%. Following this method, we get a best-fit core radius of 1.1′ (270 kpc). This core radius is rather large, on the order of the size of the cluster. However, using Eq. 22 from Bartelmann & Stienmetz (1996), we get a mass of $M(\leq 0.76 h^{-1} Mpc) = 7.4 \times 10^{14} h^{-1} M_{\odot}$. This agrees well with the mass we derive from the M-T relation.

2.5 Constraints on Ω_m

Following a line of reasoning similar to that used in D98, we determine the expected number density of clusters like MS1054 in an $\Omega_m = 1$ universe with initial Gaussian

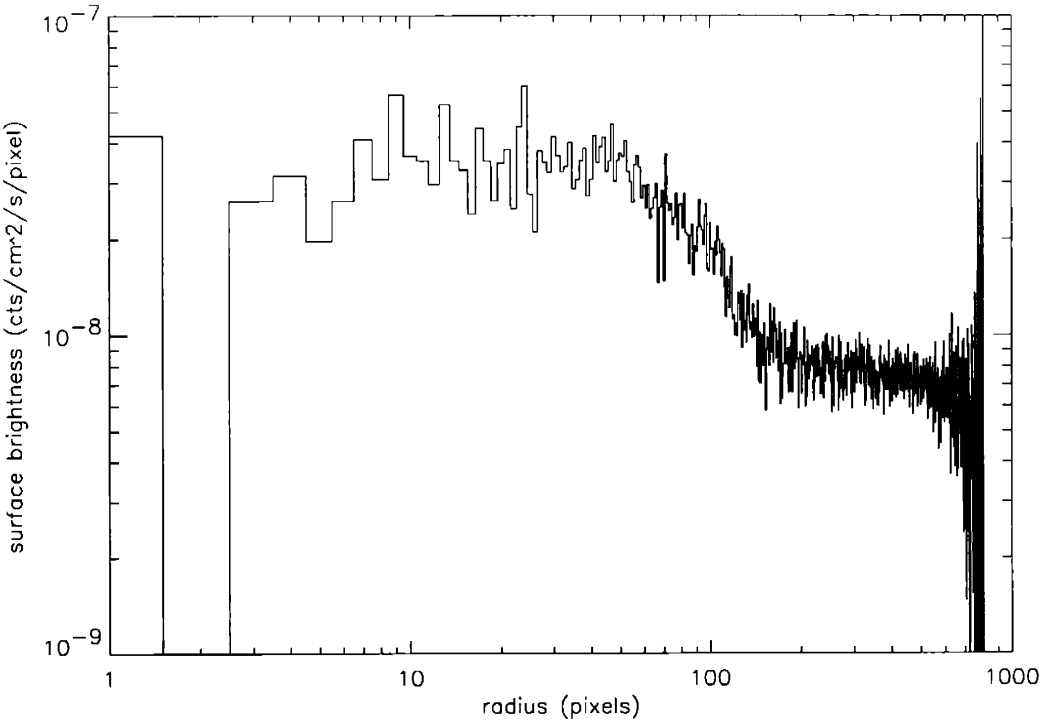

Figure 2-11 Radial surface brightness profile for MS1054-0321. 1 pixel = 2″.03 = 2.04 h^{-1} kpc.

perturbations, and we compare this value with the observed number density for detection in the EMSS. The comoving mass density of virialized objects with masses greater than M is given by the Press-Schechter formula

$$\rho(>M) = \rho_0 erfc(\frac{\nu_c}{\sqrt{2}}) = \frac{2\rho_0}{\sqrt{\pi}} \int_{\nu_c/\sqrt{2}}^{\infty} e^{-x^2}\, dx, \tag{2.2}$$

where ρ_0 is the current matter density, and ν_c is the critical threshold at which perturbations virialize (Press & Schechter 1974, D98).

We conservatively take the temperature of MS1054 to be greater than 8.5 keV; D98 used 10 keV for this calculation. The cluster mass is then at least $4.5 \times 10^{14} h^{-1} M_\odot$. The current number density of clusters of a given mass has been estimated from both observations and simulations (Bahcall & Cen 1992, Eke et al. 1996, Bahcall, Fan, & Cen 1997). We will use the results of Bahcall et al. (1997) as they give us the highest number density. We, therefore, find that at $z = 0$ the number density is less than $1.1 \times 10^{-6} h^3$ Mpc^{-3}. The mass density is then approximately $\rho(>M) \sim nM \sim 4.9 \times 10^8 h^2 M_\odot$ Mpc^{-3}.

From the Press-Schechter formula with this mass density, $\nu_c(z = 0)$ is greater than 3.13. If $\Omega_m = 1$, ν_c is proportional to (1+z), and $\nu_c(z = 0.83)$ is greater than 5.72 for clusters with $T_X > 8.5$ keV. This corresponds to a mean virialized mass density of like clusters at z=0.83 less than $2970 h^2 M_\odot$ Mpc^{-3}, and a number density less than $6.6 \times 10^{-12} h^3$ Mpc^{-3}. However, detection of MS1054 in the EMSS gives a density

of like clusters of $\sim 10^{-8}h^3$ Mpc^{-3} (D98). This exceeds our prediction for an $\Omega_m = 1$ universe with Gaussian perturbations by a factor of more than 10^3. Although the lower *Chandra* temperature gives an expected number density a factor of 15 higher than that found in D98, it does not change their conclusion that $\Omega_m = 1$ is very unlikely.

Donahue and Voit (1999) fit for Ω_m using three cluster samples with different redshift ranges. They find $\Omega_m \simeq 0.45$ for an open universe and $\Omega_m \simeq 0.27$ for a flat universe. These results are unaffected by the lower temperature for MS1054. In fact, with a temperature of 10 keV, MS1054 appears to lie closer to the best fit temperature function for the high redshift sample.

2.6 Summary

The *Chandra* observation of the cluster MS1054-0321 at z = 0.83 indicates that it has an X-ray temperature of $10.4^{+1.7}_{-1.5}$ keV. This is somewhat lower than, but consistent with, the temperature of $12.3^{+3.1}_{-2.2}$ keV previously found from the *ASCA* data (D98). We are also able to make the first positive identification of an iron line in this cluster and find a value of 0.26 ± 0.15 for the abundance relative to solar (Anders & Grevesse 1989). The detection of iron in a cluster at this redshift is consistent with early enrichment of the ICM (Mushotzky & Loewenstein 1997). *Chandra* was able to resolve substructure in MS1054, confirming the substructure in the *ROSAT/HRI* observation, and to identify a number of point sources surrounding it, a task beyond the spatial resolution of the *ROSAT/HRI*. The X-ray distribution appears to have two clumps. For the eastern clump, probably associated with the main cluster component, we find an X-ray temperature of $10.5^{+3.4}_{-2.1}$ keV. For the western clump, we find a slightly lower temperature of $6.7^{+1.7}_{-1.2}$ keV. The best-fit redshift of this second clump corresponds to the cluster redshift, and it is probably a subgroup falling into the cluster. The hardness ratio map shows no evidence of a shock between the two clumps; however, comparison of the X-ray contours with the Hubble image and weak lensing mass reconstruction may indicate that the gas in the subclump is being stripped off as it falls into the cluster. We do not detect a third clump seen in the weak lensing derived mass distribution.

In this work, we confirm, along with the weak lensing and velocity dispersion data, that MS1054 is truly a massive cluster. With *Chandra*'s resolution, we are able for the first time to determine the temperature of different regions of the cluster. This allows us to confirm that the entire cluster is hot, and that we are not measuring an anomalously high temperature due to a small shock-heated region. With *Chandra*, we are also able to quantify the point source contamination and remove it from the data when determining the temperature.

The velocity dispersion derived from our temperature is in good agreement with the observed velocity dispersion and weak lensing estimates, although our mass estimate is somewhat lower than the masses derived from these methods (Tran et al. 1999; Hoekstra et al. 2000). The lower X-ray temperature from *Chandra* of course leads to a smaller derived virial mass than the *ASCA* estimate. Even with this smaller

mass, the predicted number density of clusters like MS1054 assuming Gaussian perturbations in an $\Omega_m = 1$ universe is much smaller than the observed density. Cluster simulations indicate that we may underestimate the cluster's mass owing to the presence of substructure, but this does not affect our conclusions. Given the assumption of Gaussian initial fluctuations, this cluster still provides convincing evidence for $\Omega_m < 1$. When seen in conjunction with cosmic microwave background experiments that find $\Omega_{tot} \sim 1$ (Miller et al. 1999; de Bernardis et al. 2000; Hanany et al. 2000), this implies the existence of dark energy in the universe independent of the supernova result (Riess et al. 1998; Perlmutter et al. 1999).

2.7 Notes

The research described in this chapter was published in Jeltema, T.E., Canizares, C.R., Bautz, M.W., Malm, M.R., Donahue, M., & Garmire, G.P. 2001, ApJ, 562, 124. After this project was completed, new calibration files and analysis procedures were released for the *Chandra* data. The main result of these changes is that the cluster temperature decreases a little (Gioia et al. 2004). Gioia et al. (2004) analyze the *XMM-Newton* observation of MS1054-0321 and find it to have a temperature of $7.2^{+0.7}_{-0.6}$ keV. They also reanalyze the Chandra data and find a temperature of $7.4^{+1.4}_{-0.9}$ keV. We repeated our analysis in section 2.5 using the lower limit on the temperature from Gioia et al. (2004). Even with the lower temperature, the detection of MS1054-0321 in the EMSS still implies $\Omega_m < 1$. For an $\Omega_m = 1$ universe, the probability of finding MS1054-0321 in the EMSS is less than 0.05.

We noted above that we expect to underestimate the temperature, and therefore the mass, of MS1054 based on simulations of cluster mergers (Mathiesen & Evrard 2001). Two slightly more recent studies have found that simulated mergers cause large increases in cluster temperature (Randall, Sarazin, & Ricker 2002; Ritchie & Thomas 2002). There are a number of differences between these studies and Mathiesen & Evrard (2001), such as the definition of temperature, and they are difficult to compare. One important difference is that Randall et al. (2002) and Ritchie & Thomas (2002) compare their temperatures to the combined temperature of the two components before the merger. Mathiesen & Evrard (2001) study the temperature within a radius of fixed over density, which would not initially include the secondary. In reality, the observed luminosity and temperature depend on both the radius used and the time relative to core passage. Shocks can increase the temperature, but the addition of cold gas from the secondary decreases it. Following a merger, there are secondary dips and peaks in the luminosity and temperature due to periods of expansion followed by recollapse.

In the case of MS1054, we do not believe that we are overestimating the mass. We find no evidence of a shock between the two peaks, and the temperature of the eastern peak matches the temperature of the cluster as a whole. MS1054 has the appearance of a cluster that is just beginning to merge or perhaps is undergoing an off-center merger. In addition, our mass estimate is lower than the mass derived through weak lensing.

2.8 Acknowledgments

We would like thank Greg Bryan for the very helpful discussion of cluster simulations and mass estimates. We would also like to thank Herman Marshall, Mike Wise, and the rest of the MIT HETG/CXC group. Special thanks go to Megan Sosey of the Space Telescope Science Institute for her work on the Hubble mosaic image. This work was funded by contract SAO SV1-61010, NASA contracts NAS8-39073, NAS8-37716, and NAS8-38252, and HST grant GO-6668. MED was also partially supported by NAG5-3257 and NAG5-6236. TEJ would like to acknowledge the support of a NSF fellowship.

Bibliography

[1] Anders, E., & Grevesse, N. 1989, Geochimica et Cosmochimica Acta, 53, 197
[2] Arnaud, M., & Evrard, A.E. 1999, MNRAS, 305, 631
[3] Bahcall, N.A., & Cen, R. 1992, ApJ, 398, L81
[4] Bahcall, N.A., Fan, X., & Cen, R. 1997, ApJ, 485, L53
[5] Bartelmann, M., & Stienmetz, M. 1996, MNRAS, 283, 431
[6] Bryan, G.L., & Norman, M.L. 1998, ApJ, 495, 80
[7] Carlberg, R.G., Morris, S.L., Yee, H.K.C., & Ellingson, E. 1997, ApJ, 479, L19
[8] Chapman, S.C., Scott, D., Borys, C., & Fahlman, G.G. 2002, MNRAS, 330, 92
[9] Clowe, D., Luppino, G.A., Kaiser, N., Gioia, I.M. 2000, ApJ, 539, 540
[10] de Bernardis, P., et al., 2000, Nature, 404, 955
[11] Dickey, J.M., & Lockman, F.J. 1990, ARA&A, 28, 215
[12] Donahue, M., & Voit, G.M. 1999, ApJ, 523, L137
[13] Donahue, M., Voit, G.M., Gioia, I., Luppino, G., Hughes, J.P., & Stocke, J.T. 1998, ApJ, 502, 550 (D98)
[14] Eke, V.R., Cole, S., & Frenk, C.S. 1996, MNRAS, 282, 263
[15] Evrard, A.E., Metzler, C.A., & Navarro, J.F. 1996, ApJ, 469, 494
[16] Gioia, I.M., Maccacaro, T., Schild, R.E., Wolter, A., & Stocke, J.T. 1990, ApJS, 72, 567
[17] Gioia, I.M., Braito, V., Branchesi, M., Della Ceca, R., Maccacaro, T., & Tran, K.-V. 2004, A&A, 419, 517
[18] Hanany, S., et al., 2000, ApJ, 545, L5
[19] Henry, J.P., Gioia, I.M., Maccacaro, T., Morris, S.L., Stocke, J.T., & Wolter, A. 1992, ApJ, 386, 408
[20] Hjorth, J., Oukbir, J., & van Kampen, E., 1998, MNRAS, 298, L1
[21] Hoekstra, H., Franx, M., & Kuijken, K. 2000, ApJ, 532, 88
[22] Luppino, G.A., & Kaiser, N. 1997, ApJ, 475, 20
[23] Marshall, P.J., Hobson, M.P., Gull, S.F., & Bridle, S.L. 2002, MNRAS, 335, 1037
[24] Mathiesen, B.F., & Evrard, A.E. 2001, ApJ, 546, 100
[25] Miller, A.D., et al., 1999, ApJ, 524, L1
[26] Mushotzky, R.F., & Loewenstein, M. 1997, ApJ, 481, L63
[27] Neumann, D.M., & Arnaud, M. 2000, ApJ, 542, 35 (NA00)
[28] Oukbir, J., & Blanchard, A. 1992, A&A, 262, L21
[29] Perlmutter, S., et al. 1999, ApJ, 517, 565
[30] Press, W., & Schechter, P. 1974, ApJ, 187, 425
[31] Randall, S.W., Sarazin, C.L., & Ricker, P.M. 2002, ApJ, 577, 579

[32] Raymond, J.C., & Smith, B.W. 1977, ApJS, 35, 419
[33] Riess, A.G., et al. 1998, AJ, 116, 1009
[34] Ritchie, B.W., & Thomas, P.A. 2002, MNRAS, 329, 675
[35] Roettiger, K., Burns, J.O., & Loken, C. 1996, ApJ, 473, 651
[36] Schindler, S. 1996, A&A, 305, 756
[37] Tran, K.-V., Kelson, D.D., van Dokkum, P., Franx, M., Illingworth, G.D., & Magee, D. 1999, ApJ, 522, 39
[38] van Dokkum, P.G., Franx, M., Fabricant, D., Illingworth, G.D., & Kelson, D.D. 2000, ApJ, 541, 95

Chapter 3

The Evolution of Cluster Substructure

3.1 Introduction

Clusters form and grow through mergers with other clusters and groups. These mergers are observed as multiple peaks in the cluster density distribution or as disturbed cluster morphologies. The formation epoch of clusters depends on both Ω_m and Λ, so the amount of substructure in clusters in the present epoch and how quickly it evolves with redshift depend on these parameters. In low density universes, clusters form earlier and will be on average more relaxed in the present epoch. Clusters at high redshift, closer to the epoch of cluster formation, should be on average dynamically younger and show more structure.

A number of studies have been done on the structure of clusters at low-redshift. One of the first systematic studies was conducted by Jones & Forman (1992) who visually examined 208 clusters observed with the *Einstein* X-ray satellite. They separated these clusters into 6 morphological classes including single, elliptical, offset center, primary with small secondary, double, and complex. They found that 40% of their clusters fell into the latter five categories, and 22% fell into the three categories exhibiting multiple peaks. This study established that merging is common in clusters.

In order to test cosmology, a more quantitative measure of cluster structure and dynamical state is needed. Methods to quantify structure have used both the X-ray surface brightness distribution and, at optical wavelengths, the distribution of cluster galaxies. However, optical studies require a large number of galaxies (Dutta 1995), at least a few hundred, and are more susceptible to contamination from foreground and background objects. The only method of observing clusters that directly probes cluster mass is lensing. However, lensing is sensitive to the projection of mass along the line of sight. Strong lensing provides good resolution of mass substructure, but only at relatively small radii. In addition, strong lensing samples may be biased towards certain types of cluster structure. Weak lensing cluster observations are now becoming available for reasonably large samples of clusters; however, weak lensing does not have nearly as good resolution as current X-ray observations and, as men-

tioned before, is subject to projection effects. For the above reasons, we chose to study X-ray cluster observations. A future comparison of cluster structure in the weak lensing derived mass distributions to structure in the X-ray gas would be quite interesting.

X-ray studies of cluster substructure use a number of different statistics (see Buote 2002 for a review). Mohr et al. (1995) measured centroid variation, axial ratio or ellipticity, orientation, and radial fall-off for a sample 65 clusters. Several other studies have also used ellipticity (Gomez et al. 1997; Kolokotronis et al. 2001; Melott, Chambers, & Miller 2001; Plionis 2002); however, ellipticity is not a clear indicator of morphology. Relaxed systems can be elliptical, and substructure can be distributed symmetrically. Centroid variation is a better method in which the cluster centroid is calculated in a number of circular annuli of increasing radius. The emission weighted variation of this centroid is a measure of cluster structure (Mohr, Fabricant, & Geller 1993; Mohr et al. 1995; Gomez et al. 1997; Rizza et al. 1998; Kolokotronis et al. 2001). This method is most sensitive to equal mass double clusters.

Buote & Tsai (1995, 1996) developed the power ratio method to study a sample of 59 clusters observed with *ROSAT*. The power ratios are constructed from the moments of the X-ray surface brightness. This method has the advantages that it is both related to cluster dynamical state, and it is capable of distinguishing a large range of cluster morphologies. For our study, we chose to use the power ratio method, and it is described in more detail in section 3.3. A very large sample of clusters was studied by Schuecker et al. (2001) who looked at 470 *ROSAT* clusters. The small number of photons detected for many of their clusters prohibited using methods such as the power ratios and centroid variation. Instead, they chose to use three statistics: the β statistic which is sensitive to deviations from mirror symmetry, the Lee statistic which is most sensitive if two components are present, and the Fourier elongation test. They find that approximately 52% of their clusters have substructure in a $1h_{50}^{-1}$ Mpc radius aperture.

Richstone, Loeb, & Turner (1992) performed the first theoretical study of the relationship of substructure to cosmology. In their analytical calculations, they assumed that substructure is wiped out in a cluster crossing time, and they calculated the fraction of clusters in the spherical growth approximation which formed within the last crossing time as a function of Ω_m and Λ. They find that this fraction primarily depends on Ω_m, and they estimated that $\Omega_m \geq 0.5$ based on estimates of the frequency of substructure in low-redshift clusters (Jones & Forman 1992). This method, like the observational study of Jones & Forman (1992), predicts the ill-defined fraction of clusters with substructure. A more recent semi-analytical approach was developed by Buote (1998) who defined the dynamical state of a cluster as

$$\frac{\langle(\Delta\Phi^{\rm int})^2\rangle}{\langle(\overline{\Phi}^{\rm int})^2\rangle} \approx \left(\frac{\Delta M}{\overline{M}}\right)^2 + \sum_{l>0} \frac{\langle(\Phi_l^{\rm int})^2\rangle}{\langle(\Phi_0^{\rm int})^2\rangle}, \tag{3.1}$$

where Φ^{int} is the gravitational potential due to matter interior to a radius R, Φ_l^{int} is the lth term in the multipole expansion of the potential, $\overline{M}$ is the average mass, and ΔM is the mass accreted over a relaxation time. $\langle(\Delta\Phi^{\rm int})^2\rangle/\langle(\overline{\Phi}^{\rm int})^2\rangle$ is the fractional

increase in the rms spherically averaged potential over a crossing time. He assumes that the amount of substructure depends on the amount of mass accreted by a cluster over a relaxation timescale. This assumption leads to a strong correlation between $\Delta M/\overline{M}$ and the lower order terms of $\langle(\Phi_l^{\rm int})^2\rangle/\langle(\Phi_0^{\rm int})^2\rangle$, which are simply the three-dimensional versions of the power ratios (see section 3.3). Buote (1998) argues that $\Delta M/\overline{M}$ is also strongly correlated with the power ratios and that this correlation can be quantified with N-body simulations.

Although these semi-analytic methods give an indication of the expected evolution of cluster substructure and its dependance on cosmological parameters, perhaps the best method of constraining cosmological models is through the comparison to cluster simulations. Numerical simulations show that both the centroid (or center-of-mass) shift and the power ratios are capable of distinguishing cosmological models (Evrard et al. 1993; Jing et al 1995; Dutta 1995; Crone, Evrard, & Richstone 1996; Buote & Xu 1997; Thomas et al. 1998; Valdarnini, Ghizzardi, & Bonometto 1999; Suwa et al. 2003). Unfortunately, comparison of the different observational studies to simulations have led to contradictory conclusions. Mohr et al. (1995) found that their centroid shifts were consistent with $\Omega_m = 1$, and Buote & Xu (1997) find that the power ratios of their *ROSAT* clusters indicate an $\Omega_m < 1$ universe. Both of these studies have flaws. Buote & Xu (1997) used dark matter only simulations and approximated the power ratios of the X-ray surface brightness as the power ratios of the dark matter density squared. Mohr et al. (1995) used simulations which incorporate the cluster gas but which only included eight clusters. In addition, hydrodynamic simulations generally have poor force resolution for the gas.

Cluster structure has also been examined in two more recent sets of hydrodynamic simulations. Valdarnini et al. (1999) compute power ratios for clusters formed in three cosmological models: flat CDM, ΛCDM with $\Lambda = 0.7$, and CHDM with $\Omega_h = 0.2$ and one massive neutrino. For each model, they simulated 40 clusters and compared the results to the *ROSAT* sample studied by Buote & Tsai (1996) using the Student t-test, the F-test, and the Kolmogorov-Smirnov test. They find that the ΛCDM model is inconsistent with the data, but neither CDM or CHDM are ruled out. However, these simulations used $\sigma_8 = 1.1$. This value of σ_8 is fairly high and may cause the disagreement between the ΛCDM model and the data. In addition, these simulations neglect the effect of the tidal field at large scales. Suwa et al. (2003) compare simulated clusters in a ΛCDM and an OCDM cosmology, at both $z = 0$ and $z = 0.5$, using several methods of quantifying structure. They find that axial ratio and cluster clumpiness are not successful at distinguishing the two models. However, the center shifts and the power ratios of both the surface brightness and the projected mass density are able to discriminate between the models at $z = 0$. The power ratios of the surface brightness are also successful at $z = 0.5$. They restrict themselves to comparing the ability of different statistical indicators to distinguish cosmologies and do not compare to observations. Their simulations do not include processes like SNe feedback, radiative cooling, etc. and do not have sufficient resolution to directly compare to high-resolution X-ray data. Their results do show that cluster structure can potentially constrain Λ or a time dependent vacuum energy. Interestingly, both Valdarnini et al. (1999) and Suwa et al. (2003) find that the power ratios calculated

from the projected mass density are generally larger than those calculated from the X-ray surface brightness, because the relaxation timescale of the collisionless dark matter is longer than that of the collisional gas.

Obviously this situation needs further examination. In a future study, we will examine cluster morphology and its evolution in simulated clusters from several independent hydrodynamic simulations. The current work will focus on the observational side. Specifically, we seek to place an additional constraint on cosmological models by examining the evolution of cluster structure with redshift.

All of the observational studies described above are limited to clusters with redshifts less than approximately 0.3. Until recently, the number of clusters known with $z > 0.5$ has been limited to a few. However, recent surveys, notably the many *ROSAT* surveys, have increased this number by an order of magnitude (Rosati et al. 1998; Perlman et al. 2002; Gioia et al. 2003; Vikhlinin et al. 1998). It is now possible to study the evolution of cluster structure out to $z \sim 1$. Using a sample of 40 clusters observed with the *Chandra* X-ray Observatory we show that the amount of substructure in clusters increases with redshift, as expected qualitatively from hierarchical models of structure formation. Specifically, the power ratios are higher, on average, for clusters with $z > 0.5$ than for clusters with $z < 0.5$. This chapter is organized as follows: In section 3.2, we describe our sample selection. In 3.3, we give a more detailed description of the power ratio method. In 3.4, we describe the data reduction and the calculation of uncertainties, and in section 3.5 we give our results. Finally, we discuss the systematic effects which could influence our results, and we give our conclusions. We assume a cosmology of $H_0 = 70h_{70}$ km s^{-1} Mpc^{-1}, $\Omega_m = 0.3$, and $\Lambda = 0.7$ throughout.

3.2 The Sample

For this project, we use data from the *Chandra* archive, which allowed us to select clusters over a large redshift range with observations of sufficient depth. In addition, *Chandra's* superb resolution aids in the identification and exclusion of point sources from the analysis. A lower limit of $z = 0.1$ was placed on the redshift to ensure that a reasonable area of each cluster would be visible on a *Chandra* CCD. To ensure that the sample was relatively unbiased all clusters were selected from flux-limited X-ray surveys. The majority of the sample came from the *Einstein* Medium Sensitivity Survey (EMSS; Gioia & Luppino 1994) and the *ROSAT* Brightest Cluster Sample (BCS; Ebeling et al. 1998). Clusters were also required to have a luminosity greater than 5×10^{44} ergs s^{-1}, as listed in those catalogs. Additional high-redshift clusters were selected from recent *ROSAT* surveys including the *ROSAT* Deep Cluster Survey (RDCS), the Wide Angle *ROSAT* Pointed Survey (WARPS), the *ROSAT* North Ecliptic Pole Survey (NEP), and the 160 deg^2 survey (Rosati et al. 1998; Perlman et al. 2002; Gioia et al. 2003; Vikhlinin et al. 1998). The resulting sample contains 40 clusters with redshifts between 0.11 and 0.89. The initial sample contained about 50 clusters; however, several clusters were removed due to issues such as a high soft X-ray background flux, low signal-to-noise, or background flares.

The clusters along with their redshifts, observation IDs, clean exposure times, and luminosities within a radius of 0.5 Mpc are listed in Table 1. These luminosities were estimated from the *Chandra* observations in a 0.3-7.0 keV band and using a Raymond-Smith thermal plasma model with $N_H = 3 \times 10^{20}$ atoms cm^{-2}, $kT = 5$ keV, and an abundance of 0.3 relative to the abundances of Anders & Grevesse (1989). Changes in the column density and temperature did not have a large effect on the luminosities. The *Chandra* luminosities range from 2.0×10^{44} ergs s^{-1} to 2.3×10^{45} ergs s^{-1}.

In the following analysis, the clusters were divided into two samples. The high-redshift sample contains the 14 clusters with $z > 0.5$, and the low-redshift sample contains the 26 clusters with $z < 0.5$. The two samples have average redshifts of 0.24 and 0.71, respectively. The average luminosities of the two samples are 7.4×10^{44} ergs s^{-1} for the high-redshift sample and 9.1×10^{44} ergs s^{-1} for the low-redshift sample. As discussed later, this small difference in average luminosity does not effect our results.

3.3 The Power Ratio Method

Here we present the power ratio method as developed by Buote & Tsai (1995, 1996). The power ratios are capable of distinguishing a large range of cluster morphologies. Essentially, this method entails calculating the multipole moments of the X-ray surface brightness in a circular aperture centered on the cluster's centroid. The moments, a_m and b_m given below, are sensitive to asymmetries in the surface brightness distribution and are, therefore, sensitive to substructure. For example, for a perfectly round cluster the $m > 0$ moments are zero, for a perfectly elliptical cluster or a perfectly equal mass, symmetric double cluster the odd moments are zero but the even moments are not, and for all of the other Jones & Forman (1992) classifications the moments are all non-zero.

The physical motivation for this method is that it is related to the multipole expansion of the two-dimensional gravitational potential. Large potential fluctuations drive violent relaxation, and therefore, the power ratios are related to a cluster's dynamical state. The multipole expansion of the two-dimensional gravitational potential is

$$\Psi(R,\phi) = -2Ga_0 \ln\left(\frac{1}{R}\right) - 2G \sum_{m=1}^{\infty} \frac{1}{mR^m} \left(a_m \cos m\phi + b_m \sin m\phi\right). \qquad (3.2)$$

and the moments a_m and b_m are

$$\begin{aligned} a_m(R) &= \int_{R' \le R} \Sigma(\vec{x}') \, (R')^m \cos m\phi' d^2x', \\ b_m(R) &= \int_{R' \le R} \Sigma(\vec{x}') \, (R')^m \sin m\phi' d^2x', \end{aligned}$$

where $\vec{x}' = (R', \phi')$ and Σ is the surface mass density. In the case of X-ray studies, X-ray surface brightness replaces surface mass density in the calculation of the power ratios.

Table 3.1. The Sample

Cluster	Redshift	ObsID	Exposure (ks)	Luminosity ($10^{44} h_{70}^{-2}$ ergs s^{-1})
MS0015.9+1609	0.54	520	66	16.
CLJ0152.7-1357	0.83	913	36	5.0
A267	0.23	1448	7.0	6.0
MS0302.7+1658	0.42	525	9.9	2.8
RXJ0439.0+0715	0.24	1449	6.2	7.7
RXJ0439.0+0520	0.21	527	9.5	4.6
A520	0.20	528	9.3	6.2
MS0451.6-0305	0.54	902	42	17.
CLJ0542.8-4100	0.63	914	50	4.2
A665	0.18	531	8.9	7.6
ZWCL1953	0.38	1659	18	9.0
MS0906.5+1110	0.18	924	29	3.9
A773	0.22	533	11	7.2
A781	0.30	534	9.6	4.4
A963	0.21	903	36	7.9
ZWCL3146	0.29	909	45	23.
MS1054.5-0321	0.83	512	75	14.
CLJ1113.1-2615	0.73	915	96	2.0
V1121.0+2327	0.56	1660	69	2.4
MS1137.5+6625	0.78	536	115	6.6
A1413	0.14	1661	8.8	7.5
V1221.4+4918	0.70	1662	76	4.8
CLJ1226.9+3332	0.89	932	9.2	20.
A1758	0.28	2213	48	7.9
RXJ1350.0+6007	0.80	2229	57	2.3
MS1358.4+6245	0.33	516	47	7.1
A1914	0.17	514	6.9	14.
A2034	0.11	2204	52	4.0
RXJ1532.9+3021	0.35	1649	9.2	20.
A2111	0.23	544	10	4.4
A2218	0.18	1666	34	5.4
A2219	0.23	896	42	16.
RXJ1716.9+6708	0.81	548	51	5.6
RXJ1720.1+2638	0.16	1453	7.7	9.9
A2261	0.22	550	8.4	11.
MS2053.7-0449	0.58	1667, 551	44, 44	2.2

Table 3.1—Continued

Cluster	Redshift	ObsID	Exposure (ks)	Luminosity ($10^{44}h_{70}^{-2}$ ergs s^{-1})
RXJ2129.6+0005	0.24	552	9.8	9.7
MS2137.3-2353	0.31	928	31	14.
A2390	0.23	500	9.7	17.
CLJ2302.8+0844	0.73	918	105	2.1

Note. — Column 4 gives the net exposure after the removal of background flares. Column 5 lists cluster luminosity in the 0.3-7.0 keV band estimated using a Raymond-Smith thermal plasma model with $N_H = 3 \times 10^{20}$ atoms cm^{-2}, $kT = 5$ keV, and an abundance of 0.3. Luminosities are calculated in a circular aperture with a radius of 0.5 Mpc.

X-ray surface brightness is proportional to the gas density squared and generally shows the same qualitative structure as the projected mass density, allowing a similar quantitative classification of clusters.

The powers are formed by integrating the magnitude of Ψ_m, the mth term in the multipole expansion of the potential given in equation (2), over a circle of radius R.

$$P_m(R) = \frac{1}{2\pi} \int_0^{2\pi} \Psi_m(R,\phi)\Psi_m(R,\phi)d\phi \tag{3.3}$$

Ignoring factors of $2G$, this gives

$$P_0 = [a_0 \ln(R)]^2 \tag{3.4}$$

$$P_m = \frac{1}{2m^2 R^{2m}} \left(a_m^2 + b_m^2\right). \tag{3.5}$$

Rather than using the powers themselves, we divide by P_0 to normalize out flux forming the power ratios, P_m/P_0.

Here we consider only the observable two-dimensional cluster properties. As we cannot know a cluster's three-dimensional structure, there is a degeneracy in the interpretation of the dynamical state of any individual cluster due to projection effects. Since we are only concerned with relatively large-scale, cosmologically significant structure, it should be rare that a very disturbed cluster appears very relaxed in projection. The power ratios essentially provide a lower limit on a cluster's true structure. For a reasonable sample size, projection will not have a large effect. In addition, cosmological constraints placed through the comparison of observed clusters to numerical simulations will be valid, because the power ratios can be calculated in a consistent way from projection of the simulated clusters.

For each cluster in our sample, we calculate P_2/P_0, P_3/P_0, and P_4/P_0 in a circular aperture centered on the centroid of cluster emission. P_1 vanishes with the origin at the centroid, and the higher order terms are sensitive to successively smaller scale structures which are both more affected by noise and less cosmologically significant. The results given here are for an aperture radius of 0.5 Mpc. The choice of aperture size will be discussed in more detail in the next section.

3.4 Data Reduction and Uncertainties

3.4.1 Image Preparation

For the most part, the data was prepared using the standard data processing, including updating the gain map, applying the pixel and PHA randomizations, and filtering on *ASCA* grades 0, 2, 3, 4, and 6 and a status of zero[1]. In the case of ACIS-I observations performed in VFAINT (VF) mode, the additional background cleaning for VF mode data was also applied. Events are graded to distinguish good X-ray events from cosmic rays. In the standard data processing, events are graded based on the pulse height in a 3x3 pixel island; in VF mode, the data includes the pixel values in a 5x5 island, allowing the extra pixels to be used to flag bad events. This extra cleaning was not applied to VF mode ACIS-S observations or observations at a focal plane temperature of -110°C due to the lack of corresponding background data (see section 3.4.2). We also did not apply the charge transfer inefficiency (CTI) correction. This correction was released half-way through our analysis, and it was not released for all chips and all time periods. As a test, we applied the CTI correction to a few of the clusters in our sample and found that it had virtually no effect on the flux in the energy band we use.

The energy range was restricted to the 0.3-7.0 keV band. The data was then filtered to exclude time periods with background flares using the routine *lc_clean*. The filtering excluded time periods when the count rate, excluding point sources and cluster emission, in the 0.3-10 keV band was not within 20% of the quiescent rate. This filtering matches the filtering applied to the background fields we use[2]. For ACIS-S observations, flares were detected on S3 only when the cluster emission did not cover more than 20% of the chip; otherwise, flares were detected using the other back-illuminated CCD, S1. Observations with high background rates compared to the background fields were removed from the sample. We then normalized the cluster images by a map of the exposure. Exposure maps were weighted according to a Raymond-Smith spectrum with $N_H = 3 \times 10^{20}$ atoms cm^{-2}, $kT = 5$ keV, and an abundance of 0.3 relative to solar.

The last step in the preparation of cluster images was the removal of point sources. We detected point sources using the CIAO routine *wavdetect* with the significance threshold set to give approximately one false detection per cluster image and wavelet

[1] *Chandra* Proposers' Observatory Guide http://cxc.harvard.edu/proposer/POG/, section "ACIS"

[2] See http://cxc.harvard.edu/cal/Acis/Cal_prods/bkgrnd/acisbg/COOKBOOK.

scales of 1, 2, 4, 8, and 16 pixels. Elliptical background regions were defined around each source such that they contained at least five background counts. We adjusted source and background regions by hand to ensure that they did not overlap other sources or extend off the image. In some cases, sources containing only a few counts that did not appear to be real were excluded, and the regions around bright sources were expanded to include more of the counts in the wings of the PSF. Finally, we removed the sources and filled the source regions using the CIAO tool *dmfilth*. This tool fits a polynomial to each background region, and it computes pixel values within the source region according to this fit. For many clusters, wavdetect found a source at the center of the cluster. In most cases, this source was simply the peak of the surface brightness distribution rather than a central X-ray point source. In all cases, the flux of the "source" was small compared to the cluster flux. We computed the power ratios for several clusters both with and without the central "source" and found that they did not change significantly.

For one cluster, MS2053.7-0449, we merged two observations. Several of the clusters in our sample had multiple observations in the archive, but in the other cases these observations were made at different focal plane temperatures or with different detectors. Under these circumstances we chose to use only the longest observation. Both observations of MS2053.7-0449 were prepared separately according to the steps described above. The two observations were aligned by hand using six bright X-ray point sources that appear in both images. After the exposure correction, we merged the two images. Point sources were then detected and filled in the combined image.

3.4.2 Background

To account for the X-ray background, we chose to use the ACIS "blank-sky" data sets. The X-ray background consists of two components, the particle background and the summed emission from unresolved X-ray sources. The blank-sky data sets are a combination of several relatively source free observations with any obvious sources removed[3]. An observation specific local background was not used because it is difficult to find an area of the detector free of cluster emission for the low-redshift clusters. In addition, the blank-sky data sets allow us to extract a background from the same region of the CCD as the cluster emission which more accurately models spatial variation in the background. The background files are divided into four time periods to account for changes in the background due to a changing focal plane temperature. Our sample includes observations from the last three time periods (B, C, and D). Period B includes the time period when the focal plane temperature was $-110°$C, and periods C and D are for a focal plane temperature of $-120°$C.

The backgrounds were matched to the observation dates with a couple of exceptions. The period D background files contained only observations performed in VF mode allowing these files to be filtered using the additional VF background cleaning, but the period B and C files did not. For cluster observations performed in VF

[3]See the web pages http://cxc.harvard.edu/contrib/maxim/bg/index.html and http://cxc.harvard.edu/cal/Acis/Cal_prods/bkgrnd/acisbg/COOKBOOK.

mode during period C, we used the period D background files. Periods C and D have the same focal plane temperature, and the backgrounds are not very different. For VF mode, period B cluster observations, we used the period B background files and did not perform the VF background cleaning. The period C background files for the ACIS-S detector included observations in the North Polar Spur, and they have a high soft background rate. Therefore, period D background files were also used for ACIS-S, period C observations.

To prepare background images for each cluster observation we took the following steps. First, the gain file of the background was updated to match the gain file used on the corresponding cluster observation. The background events were then reprojected using the cluster aspect file to match the coordinates of the observation. We limited the energy range to 0.3-7.0 keV, and for the D, VF backgrounds we applied the VF filtering. The background files have a much longer exposure time than the observations and must be normalized to match them. We normalized the backgrounds by the ratio of the flux in the 10-12 keV band of the observation to the 10-12 keV flux of the background. These fluxes were calculated after removing cluster and source regions from both the observation and the background, and they were calculated separately for each CCD in the image. The 10-12 keV energy band is used because it is above the passband of the grazing incidence optics. Therefore, it is relatively free of sky emission, and the count rate in this band is fairly constant between observations[4]. We checked these normalizations against the ratio of the exposure times to make sure they were not too different. Another check performed was a comparison of the soft band flux for the cluster pointings versus the pointings included in the background files using the *ROSAT* All-Sky Survey (RASS) R4-R5 band data (Snowden et al. 1997). This check is necessary to ensure that the background files will sufficiently match the background in the observations. A few clusters located in regions of high RASS flux were excluded from the sample.

The last step in the preparation of the background images was to properly account for bad pixels and columns. Pixels flagged as bad include "hot" pixels, node boundaries, pixels with bias errors, and pixels adjacent to bad pixels. Individual pixels flagged as bad would have little effect on the power ratios; however, bad columns may be important. Unfortunately, the bad pixel lists excluded from the background files do not match the observation bad pixel files. For example, pixels and columns adjacent to bad pixels/columns were not excluded from the backgrounds but are excluded from the observations. To account for this mismatch, we made two instrument only exposure maps (i.e. they do not include the effects of the mirror and quantum efficiency) for each background image, one with the background bad pixels and one with the observation bad pixels. We then divided the background image by the background bad pixel exposure map and multiplied it by the observation bad pixel map. Finally, the background image was exposure corrected using the full observation exposure map (including the mirror and QE). For MS2053.7-0449, the background images for each observation were prepared separately and then added.

[4]http://cxc.harvard.edu/cal/Acis/Cal_prods/bkgrnd/acisbg/COOKBOOK

3.4.3 Power Ratio Calculation and Estimation of Uncertainties

The power ratios were calculated in circular apertures for a range of aperture radii varying from co-moving 0.1 Mpc to 1.2 Mpc (or the largest aperture which completely fit in the area of the detector) in 0.1 Mpc intervals. We assumed a cosmology of $H_0 = 70h_{70}$ km s^{-1} Mpc^{-1}, $\Omega_m = 0.3$, and $\Lambda = 0.7$. First, the centroids (where P_1 vanishes) were calculated for each aperture starting with the largest aperture that fit on the detector and iterating in to an aperture radius of 0.1 Mpc. For each aperture, we then calculated P_0, P_2, P_3, and P_4. In the calculation of the powers, the X-ray background was accounted for by calculating the moments ($a_0 - a_4$ and $b_0 - b_4$) separately for the cluster image and the background image and then subtracting the background moments from the observed moments. We then used the net cluster moments to find the powers.

Some of the high-redshift clusters have relatively small fluxes, so it was desirable to set cutoffs for the minimum acceptable number of cluster counts and the minimum signal-to-noise (S/N) level. We, therefore, only considered apertures with more than 500 net counts and with a S/N in the annulus surrounding the next smaller aperture of greater than 3.0. Below this signal-to-noise level the program often had difficulty locating the centroid. We found that an aperture radius of 0.5 Mpc was the largest radius for which all of the high-redshift clusters had an acceptable S/N and which was small enough not to extend beyond the detector for any of the low-redshift clusters. The following analysis and discussion will be limited to this aperture size. The power ratios for a radius of 0.5 Mpc are listed in Table 2.

To estimate the uncertainty in the power ratios due to noise, we employed a Monte Carlo method (Buote & Tsai 1996). First, the exposure corrected cluster images were adaptively binned, using the program *AdaptiveBin* developed by Sanders and Fabian (2001), to give a minimum of two counts per bin. This procedure removed almost all zero pixels, although a few remained because we required that only adjacent pixels be binned together. To add back instrumental effects, the binned image was multiplied by the exposure map. We then added Poisson noise by taking each pixel value as the mean for a Poisson distribution and then randomly selecting a new pixel value from that distribution. Finally, the image was exposure corrected. This process was repeated 100 times for each cluster creating 100 mock cluster observations. A few of the clusters in our sample had background moments similar to the cluster moments. For these clusters, the effects of noise in the background images become important, and we also created 100 mock background images.

We calculated the power ratios for each of the 100 mock cluster images, and the 90% confidence limits were defined to be the fifth highest and fifth lowest ratios. These confidence intervals are listed in Table 3. In the case of MS2053.7-0449, we created 100 mock images for each of the two cluster observations and merged them before calculating the power ratios. For three of the clusters in our sample, one of the observed power ratios falls below the uncertainties. We expect that a few clusters will fall outside of their errors, because the errors are only 90% limits. In all three cases, the power ratios for the surrounding aperture sizes are more reflective of the

Table 3.2. Power Ratios

Cluster	P_2/P_0 ($\times 10^{-7}$)	P_3/P_0 ($\times 10^{-7}$)	P_4/P_0 ($\times 10^{-7}$)
MS0015.9+1609	46.8	0.0427	0.000603
CLJ0152.7-1357	275.	15.8	5.70
A267	62.5	0.00510	0.384
MS0302.7+1658	42.8	2.44	0.801
RXJ0439.0+0715	47.2	1.26	0.146
RXJ0439.0+0520	1.82	0.112	0.0155
A520	41.7	2.72	0.991
MS0451.6-0305	66.4	2.28	0.351
CLJ0542.8-4100	65.2	1.57	2.85
A665	20.0	2.60	0.676
ZWCL1953	32.6	1.33	0.0380
MS0906.5+1110	21.2	0.0689	0.0103
A773	47.5	0.0561	0.374
A781	25.4	1.62	5.61
A963	5.11	0.367	0.0163
ZWCL3146	4.46	0.0888	0.0116
MS1054.5-0321	151.	10.5	3.48
CLJ1113.1-2615	7.01	2.51	1.04
V1121.0+2327	49.4	16.1	0.907
MS1137.5+6625	6.73	0.580	0.00815
A1413	58.3	0.119	0.284
V1221.4+4918	50.8	2.18	1.76
CLJ1226.9+3332	1.90	1.56	0.0840
A1758	188.	1.12	1.65
RXJ1350.0+6007	75.0	20.9	0.324
MS1358.4+6245	13.3	0.286	0.0335
A1914	15.9	0.765	0.00769
A2034	14.1	0.495	0.180
RXJ1532.9+3021	5.05	0.00623	0.0254
A2111	113.	0.685	0.590
A2218	27.6	0.281	0.0556
A2219	142.	0.716	1.03
RXJ1716.9+6708	42.3	0.857	0.870
RXJ1720.1+2638	5.49	0.176	0.0391
A2261	4.94	0.308	0.0966
MS2053.7-0449	15.8	3.34	0.525
RXJ2129.6+0005	18.0	0.0227	0.152

Table 3.2—Continued

Cluster	P_2/P_0 ($\times 10^{-7}$)	P_3/P_0 ($\times 10^{-7}$)	P_4/P_0 ($\times 10^{-7}$)
MS2137.3-2353	1.87	0.0269	0.0140
A2390	58.2	0.344	0.289
CLJ2302.8+0844	9.11	4.65	0.303

position of the uncertainties.

We did not include the effects of point sources in the error estimation because neither unresolved sources nor the details of the source filling have a large effect on the power ratios. We estimated the flux from unresolved sources for a high-redshift, low-exposure cluster, CLJ0152.7-1357, using the LogN-LogS relation from the Chandra Deep Field South (Campana et al. 2001; Tozzi et al. 2001). This flux amounted to at most 13% of the total cluster flux. Unless all of the unresolved X-ray sources were spatially located at the same position, they would not have a significant effect on the power ratios. As far as the source removal and filling, the number of source counts removed from the 0.5 Mpc aperture only exceeded 10% of the cluster counts in a few cases and was never greater than 25% of the cluster counts. The percentage of the counts added by the filling of the source regions was quite a bit smaller. For three clusters, we experimented with the level of binning by trying both binning to give 25 counts per bin and not binning at all. The binning criteria did not seem to have a large effect on the errors derived. However, large amounts of binning tended to smooth out cluster structure and led to a shift in the derived errors toward lower values of the power ratios.

An additional systematic effect considered was the normalization of the background. To estimate the size of the possible error in the background normalizations, we compared the source free 0.3-7.0 keV flux in the observations to the same flux in the normalized backgrounds. We estimate that the background normalizations could be off by a factor between 0.9 and 1.2. We, therefore, reran the error calculations using both a background of 0.9*(background image) and 1.2*(background image) to bound the possible effect on the power ratios. For cluster observations where the 0.5 Mpc aperture fell on multiple CCDs, we renormalized each CCD by 0.9 and 1.2 separately creating $2^{\#ofchips}$ background images, and we ran the error calculation for each of these backgrounds. The systematic errors are listed in brackets in Table 3 next to the corresponding noise errors. We defined the systematic error to be the difference between the average of the 100 power ratios calculated with the original background and the average of the 100 power ratios calculated with the renormalized background. The renormalization of 0.9 creates a shift towards smaller power ratios, and the renormalization of 1.2 creates a shift towards larger power ratios. In a couple of cases, both renormalizations caused a shift of the same sign (P_4/P_0 for RXJ0439.0+0715 and P_3/P_0 for MS0015.9+1609) and the corresponding error was set to zero. For the eight clusters where the 0.5 Mpc aperture fell on multiple CCDs,

we list the maximum offset in the average power ratios of the $2^{\#ofchips}$ renormalized runs from the original background run as the systematic error.

3.5 Results

Figure 1 illustrates the ability of the power ratios to distinguish different cluster morphologies. The central plot shows P_2/P_0 versus P_3/P_0 (or the quadrupole ratio versus the octupole ratio) for the 40 clusters in our sample. The different power ratios are sensitive to different types of structure and the correlations among them aid in differentiating cluster morphologies. In this plot, one could imagine a roughly diagonal line with the most disturbed clusters appearing at the upper-right and the most relaxed clusters appearing at the lower-left. Smoothed *Chandra* images for six clusters are also shown with their power ratios indicated. These images all have the same physical scale of 1.4 Mpc on a side, and while the images contain X-ray point sources, these sources were removed before calculating the power ratios. Both the double cluster CLJ0152.7-1357 and the complex cluster V1121.0+2327 have high power ratios (upper-right), while RXJ0439.0+0520, a relatively round, relaxed cluster, has small power ratios. In between these are two clusters with smaller scale substructure. A1413, an elliptical cluster, has similar P_3/P_0 but higher P_2/P_0 than RXJ0439.0+0520 (odd multipoles are not sensitive to ellipticity).

Figures 2-4 show the three possible projections of the power ratios. Here the high-redshift clusters are plotted with diamonds and have solid error bars. The low-redshift clusters are plotted with asterisks and have dashed error bars. These error bars represent the noise only 90% confidence limits. It is apparent from these plots that the two samples have a similar distribution of P_2/P_0; however, the high-redshift clusters tend to have both higher P_3/P_0 and higher P_4/P_0 than the low-redshift clusters. In particular, in the plot of P_3/P_0 versus P_4/P_0 the high-redshift clusters appear for the most part in the upper corner of the plot, while the low-redshift clusters tend towards the lower corner. These results indicate that the high-redshift clusters have, on average, more substructure and are dynamically young compared to the low-redshift clusters. The fact that P_2/P_0 does not distinguish the two samples could stem from its sensitivity to ellipticity. As mentioned before, ellipticity is not a clear indicator of dynamical state. In Figure 1, CLJ0152.7-1357 has significant ellipticity, but V1121.0+2327, which also shows significant substructure, is comparatively round. In addition, A1413 is fairly elliptical but also fairly relaxed. Ellipticity also contributes to P_4/P_0, but this ratio is more sensitive to smaller scale structure than P_2/P_0. For example, a boxy or cloverleaf cluster structure would give a large P_4/P_0. P_3/P_0 best distinguishes the high and low-redshift clusters. As an odd multipole term, this ratio is not sensitive to ellipticity, and large P_3/P_0 is a clear indication of an asymmetric cluster structure.

We performed a number of tests to establish the statistical significance of the difference in power ratios between the high and low-redshift samples. A Wilcoxon rank-sum test (e.g., Walpole & Myers 1993) gives a probability of 4.6×10^{-5} that the high and low-redshift clusters have the same mean P_3/P_0 and a probability of 0.025

Table 3.3. Power Ratio Errors

Cluster	P_2/P_0 ($\times 10^{-7}$)	P_3/P_0 ($\times 10^{-7}$)	P_4/P_0 ($\times 10^{-7}$)
MS0015	37-55 [+0.71,-0.36]	0.098-1.2 [+0.0045,-0]	0.0013-0.15 [+6.5e-4,-3.8e-4]
CLJ0152	130-480 [+49,-21]	4.5-37 [+2.4,-1.0]	0.88-12 [+0.99,-0.47]
A267	43-79 [+1.8,-0.89]	0.020-1.0 [+0.0072,-0.0041]	0.055-0.94 [+0.0089,-0.0041]
MS0302	7.0-71 [+3.1,-1.4]	0.054-7.1 [+0.23,-0.11]	0.10-3.5 [+0.15,-0.065]
RXJ0439+07	27-60 [+1.3,-0.75]	0.22-3.7 [+0.025,-0.057]	0.011-0.70 [+0,-0.0028]
RXJ0439+05	0.21-5.5 [+0.68,-0.55]	0.0073-1.2 [+0.013,-0.0062]	0.0027-0.27 [+0.0037,-0.0019]
A520	22-49 [+0.74,-0.36]	1.3-5.2 [+0.040,-0.019]	0.51-2.8 [+0.031,-0.015]
MS0451	52-80 [+1.9,-0.95]	1.7-3.9 [+0.13,-0.060]	0.13-0.73 [+0.014,-0.0057]
CLJ0542	38-110 [+8.2,-3.7]	0.10-6.3 [+0.26,-0.12]	0.59-7.0 [+0.49,-0.23]
A665	13-30 [+1.7,-1.3]	1.2-5.0 [+0.33,-0.28]	0.34-1.5 [+0.014,-0.0072]
ZWCL1953	23-48 [+1.3,-0.64]	0.14-2.3 [+0.019,-0.0088]	0.0062-0.48 [+0.0055,-0.0022]
MS0906	16-26 [+0.78,-0.37]	0.0041-0.31 [+0.0032,-8.1e-4]	0.0018-0.11 [+3.3e-4,-3.7e-4]
A773	36-63 [+1.0,-0.49]	0.020-1.0 [+0.025,-0.027]	0.15-1.2 [+0.021,-0.022]
A781	13-60 [+1.3,-0.64]	0.24-7.3 [+0.090,-0.041]	1.7-7.8 [+0.14,-0.080]
A963	3.3-6.5 [+0.22,-0.10]	0.23-0.73 [+0.022,-0.010]	0.0015-0.069 [+0.0020,-9.0e-4]
ZWCL3146	3.5-5.7 [+0.072,-0.044]	0.035-0.19 [+0.0098,-0.0087]	0.0013-0.040 [+0.0017,-0.0015]
MS1054	120-180 [+9.3,-4.3]	6.0-15 [+0.85,-0.37]	2.1-5.5 [+0.30,-0.14]
CLJ1113	0.70-39 [+6.3,-2.1]	0.70-20 [+3.3,-1.1]	0.090-4.8 [+0.58,-0.21]
V1121	24-88 [+11,-4.5]	7.6-33 [+3.5,-1.5]	0.15-5.1 [+0.46,-0.15]
MS1137	2.1-19 [+2.4,-1.0]	0.035-2.5 [+0.12,-0.044]	0.020-0.79 [+0.058,-0.021]
A1413	50-67 [+0.84,-0.42]	0.027-0.54 [+0.0033,-0.0020]	0.15-0.59 [+0.0050,-0.0021]
V1221	24-79 [+5.9,-2.6]	0.80-8.0 [+0.35,-0.15]	0.73-5.7 [+0.38,-0.16]
CLJ1226	0.53-14 [+0.37,-0.16]	0.41-5.5 [+0.11,-0.058]	0.018-1.2 [+0.026,-0.0081]
A1758	170-200 [+6.5,-3.1]	0.71-2.1 [+0.042,-0.025]	1.2-2.2 [+0.072,-0.035]
RXJ1350	39-230 [+24,-9.5]	3.7-51 [+5.1,-1.8]	0.16-13 [+1.4,-0.50]
MS1358	9.7-18 [+0.51,-0.24]	0.10-0.60 [+0.021,-0.010]	0.0035-0.16 [+0.0058,-0.0027]
A1914	12-21 [+0.29,-0.14]	0.37-1.5 [+0.015,-0.0068]	0.0012-0.11 [+0.0011,-8.1e-4]
A2034	12-17 [+3.2,-2.6]	0.24-0.84 [+0.11,-0.080]	0.095-0.30 [+0.052,-0.044]
RXJ1532	3.1-8.4 [+0.066,-0.034]	0.0031-0.14 [+4.9e-4,-1.7e-4]	0.0044-0.13 [+0.0014,-8.0e-4]
A2111	78-150 [+5.3,-2.6]	0.081-2.9 [+0.077,-0.047]	0.036-1.5 [+0.028,-0.014]
A2218	22-33 [+3.1,-2.6]	0.12-0.91 [+0.078,-0.059]	0.011-0.21 [+0.015,-0.011]
A2219	130-150 [+2.4,-1.2]	0.44-1.0 [+0.0088,-0.0038]	0.87-1.3 [+0.018,-0.0088]
RXJ1716	17-82 [+7.7,-3.4]	0.15-6.6 [+0.30,-0.12]	0.058-3.6 [+0.14,-0.062]
RXJ1720	3.2-7.8 [+0.36,-0.21]	0.053-0.66 [+0.066,-0.057]	0.0038-0.17 [+0.0086,-0.0059]
A2261	1.7-6.5 [+0.075,-0.035]	0.013-0.80 [+0.010,-0.0051]	0.020-0.34 [+0.0018,-8.9e-4]
MS2053	2.7-42 [+5.2,-2.1]	0.53-14 [+1.1,-0.47]	0.051-4.0 [+0.31,-0.11]
RXJ2129	13-24 [+0.29,-0.14]	0.0085-0.63 [+0.0050,-0.0023]	0.023-0.36 [+0.0031,-0.0017]
MS2137	1.2-2.8 [+0.024,-0.0095]	0.0038-0.12 [+0.0014,-6.7e-4]	0.0035-0.066 [+2.1e-4,-8.7e-5]
A2390	52-67 [+0.074,-0.038]	0.17-1.0 [+0.0079,-0.044]	0.13-0.59 [+0.0036,-0.0021]
CLJ2302	0.74-42 [+6.5,-2.3]	0.81-19 [+3.7,-1.2]	0.067-3.7 [+0.58,-0.20]

Note. — 90% confidence intervals for the power ratios based on Monte Carlo simulations. The average systematic errors from the normalization of the background are listed in brackets.

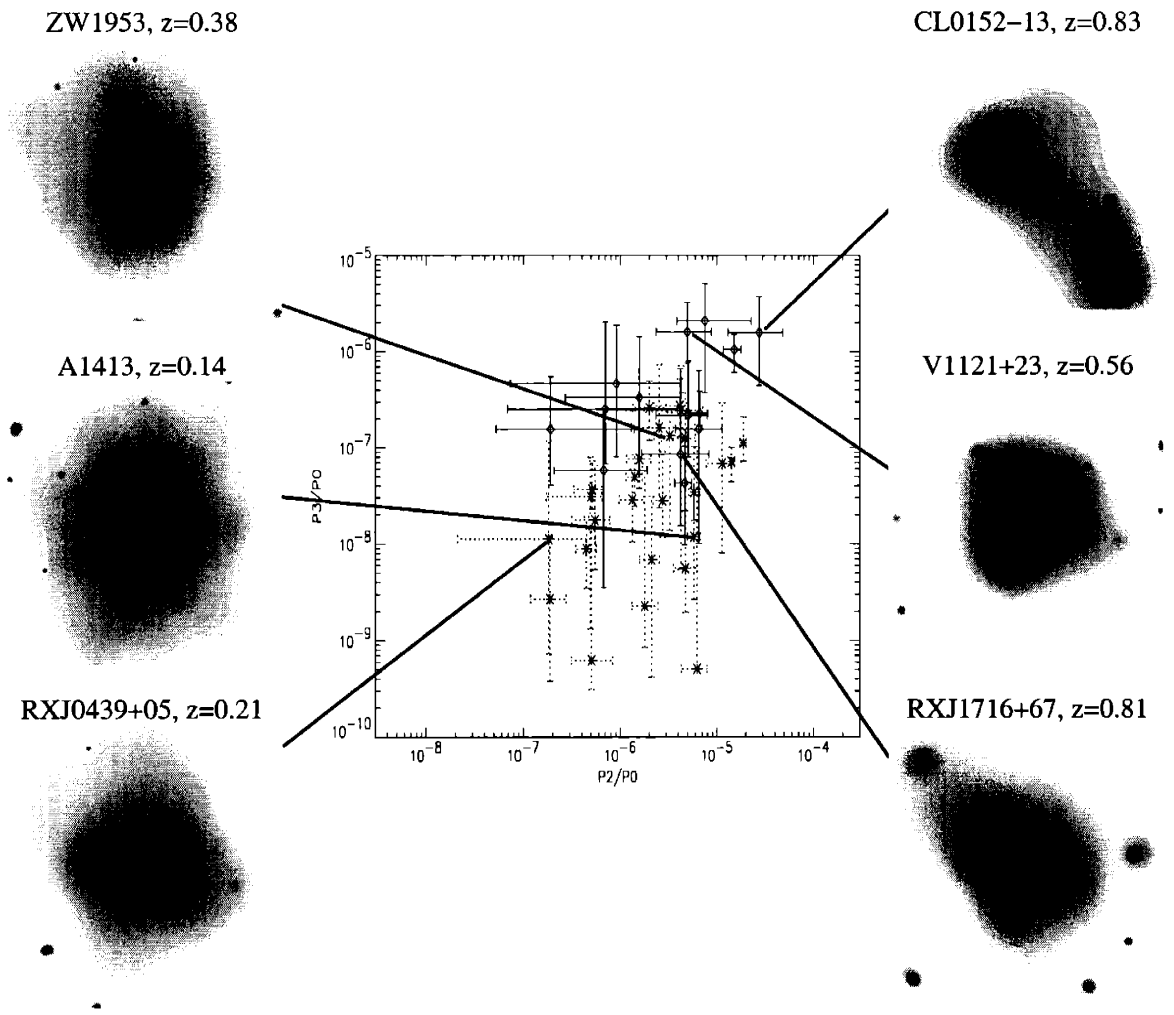

Figure 3-1 The central plot shows P_2/P_0 versus P_3/P_0. Smoothed images for six clusters are shown with their power ratios indicated. Both the double cluster CLJ0152.7-1357 and the complex cluster V1121.0+2327 have high power ratios (upper-right), while RXJ0439.0+0520, a relatively round, relaxed cluster, has small power ratios. In between these are clusters with smaller scale substructure. A1413, an elliptical cluster, has similar P_3/P_0 but higher P_2/P_0 than RXJ0439.0+0520 (odd multipoles are not sensitive to ellipticity). Power ratios are computed in a 0.5 Mpc radius aperture. High-redshift clusters ($z > 0.5$) are plotted with diamonds and have solid error bars. Low-redshift clusters are plotted with asterisks and have dashed error bars. The images were adaptively smoothed using the CIAO routine *csmooth*.

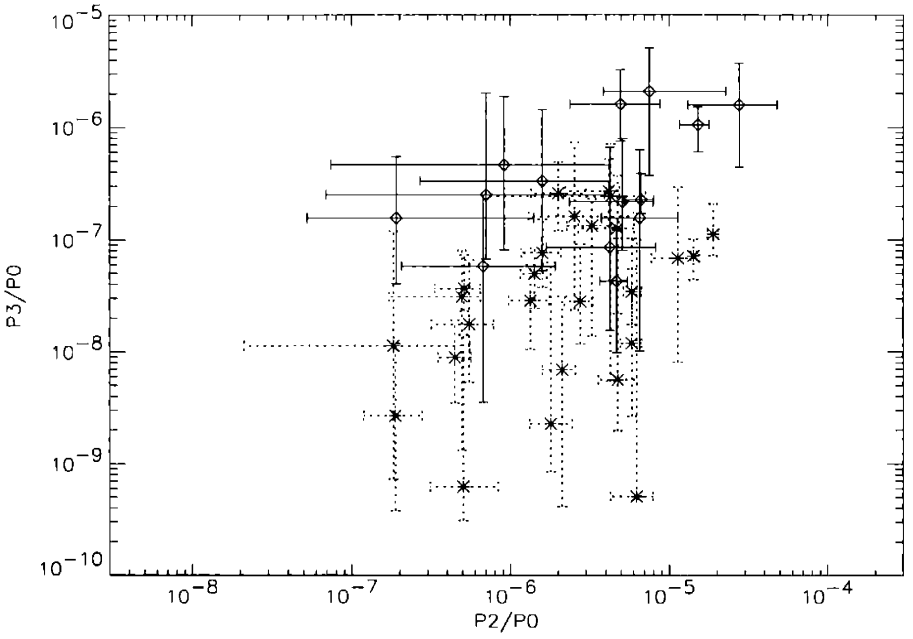

Figure 3-2 P_2/P_0 versus P_3/P_0. Power ratios are computed in a 0.5 Mpc radius aperture. High-redshift clusters ($z > 0.5$) are plotted with diamonds and have solid error bars. Low-redshift clusters are plotted with asterisks and have dashed error bars.

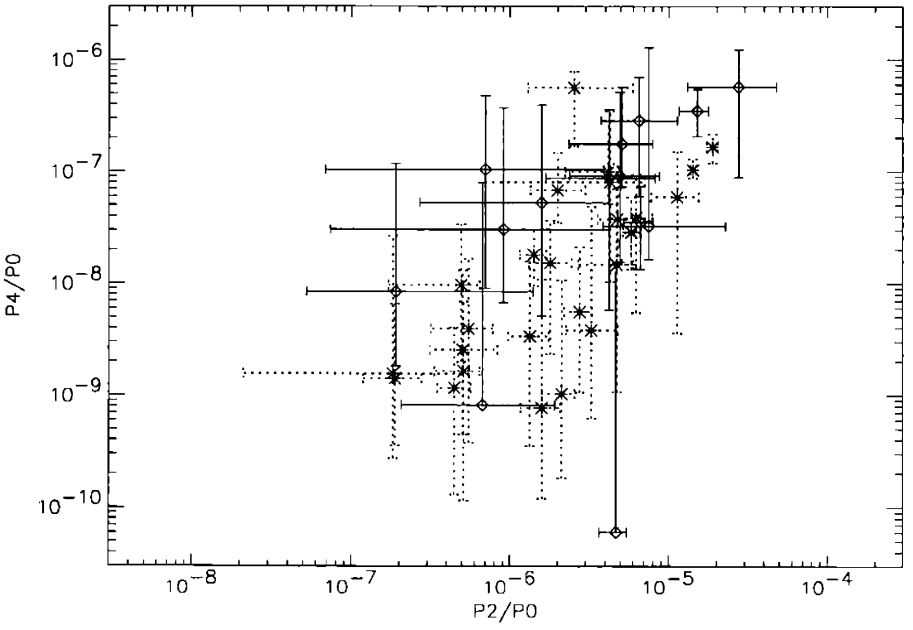

Figure 3-3 Same as Figure 2 for P_2/P_0 versus P_4/P_0.

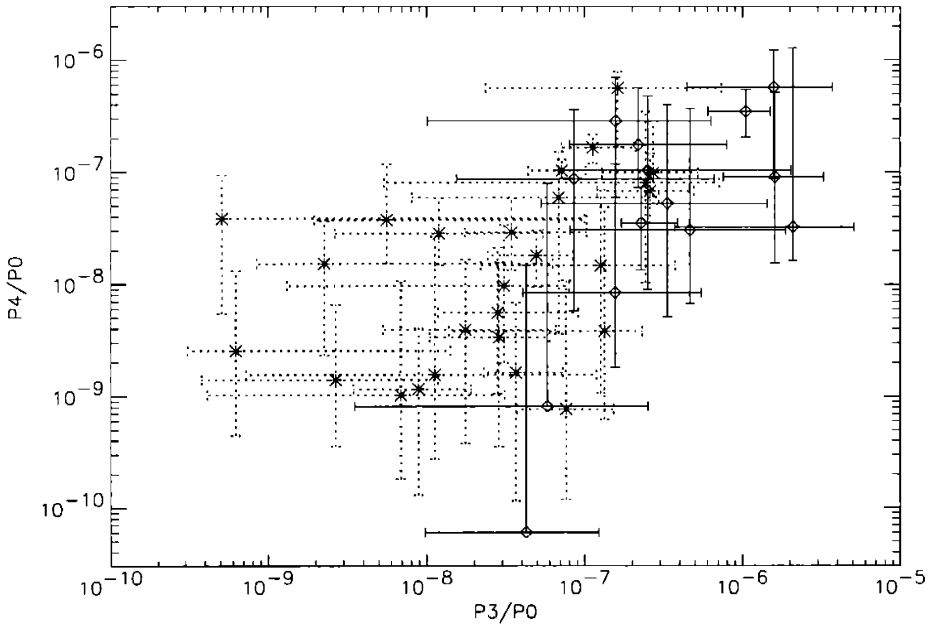

Figure 3-4 Same as Figure 2 for P_3/P_0 versus P_4/P_0.

for P_4/P_0. A Kolmogorov-Smirnov test (e.g., Press et al. 1992, §14.3) also shows that the distributions of P_3/P_0 and P_4/P_0 differ significantly for the high and low-redshift samples, giving probabilities of 0.00064 and 0.041 for P_3/P_0 and P_4/P_0, respectively. These tests do not show a significant difference in the distributions of P_2/P_0.

Unfortunately, the above tests do not include the uncertainties in the power ratios. However, we have the results of the Monte Carlo simulations from which we can resample the power ratios for each cluster. To account for both the noise and systematic errors we combined the results of the error calculations for the three background normalizations, giving 300 sets of power ratios for each cluster. We then randomly selected P_3/P_0 and P_4/P_0 from these 300 for each cluster and reran the rank-sum and Kolmogorov-Smirnov (KS) tests. This process was repeated 1000 times. For P_3/P_0, the rank-sum test never gives a probability higher than 0.018. The KS test gives an average probability of 0.0023 and only gives a probability greater than 0.05 for 5 out of 1000 runs. The result that the high-redshift clusters generally have higher P_3/P_0 is therefore highly significant. For P_4/P_0, the average rank-sum probability is 0.0082 with 28 of 1000 runs yielding a probability greater than 0.05. For the KS test, these numbers are 0.037 and 204 out of 1000, respectively. The difference in the average P_4/P_0 between the two samples is more marginal than for P_3/P_0 but still fairly significant. Table 4 summarizes these results and lists the average power ratios for each sample.

Buote & Tsai (1996) reported a significant correlation between the power ratios of the clusters in their sample. As can be seen from Figures 2-4, this correlation is also present in our data. The Spearman Rank-Order Correlation test (e.g., Press et al. 1992, §14.6) gives probabilities of 0.017, 9.2×10^{-6}, and 2.5×10^{-5} for the $P_2/P_0 - P_3/P_0$, $P_2/P_0 - P_4/P_0$, and $P_3/P_0 - P_4/P_0$ correlations. A probability of

Table 3.4. Statistical Significance of Results

	Average Low-z	Average High-z	Rank-Sum Prob.	KS Prob.	Average RS Prob.	Average KS Prob.
P_2/P_0	3.92e-6	6.16e-6	0.10	0.34	-	-
P_3/P_0	6.93e-8	5.95e-7	4.6e-5	0.00064	0.00036	0.0023
P_4/P_0	5.20e-8	1.30e-7	0.025	0.041	0.0082	0.037

Note. — Columns 1 and 2 give the average power ratios for the high and low-redshift samples, respectively. Column 3 lists the probability from a rank-sum test that the low and high-redshift clusters have the same average power ratios. The probability from a KS-test that the two samples have the same distribution is given in column 4. The last two columns list the average rank-sum and KS probabilities for 1000 runs where the power ratios were randomly selected from the Monte Carlo simulations.

one indicates no correlation, and the test included all 40 clusters. The same test applied to the low and high-redshift samples separately gave mixed results. The $P_2/P_0 - P_4/P_0$ correlation is significant for both samples, and the $P_3/P_0 - P_4/P_0$ correlation is significant for the low-redshift sample. The correlations among the high-redshift clusters generally gave marginal results, which is perhaps not surprising given the small sample size and relatively large errors. Similar to Buote & Tsai (1996), we find the most significant correlation in $P_2/P_0 - P_4/P_0$.

Finally, we compare our results to the 59 $z \leq 0.2$ clusters studied by Buote & Tsai (1996). The overall range of power ratios in our sample is very similar to their sample. For the five clusters common to both samples, our power ratios are all contained within the Buote & Tsai (1996) confidence ranges except P_4/P_0 for A1914. We find no significant difference between our low-redshift sample and the Buote & Tsai (1996) sample; however, all three power ratios are significantly higher for our high-redshift sample. Figure 5 shows P_3/P_0 versus P_4/P_0 for the 59 Buote & Tsai (1996) clusters compared to our clusters.

3.6 Discussion

Here we discuss several systematic effects which could influence our results. First, we investigate whether the difference in power ratios could be caused by a difference in luminosity between the two samples. In calculating the power ratios, we normalize by cluster flux to get a "shape only" measure; however, one could imagine that massive clusters and groups could have different amounts of substructure. In selecting the

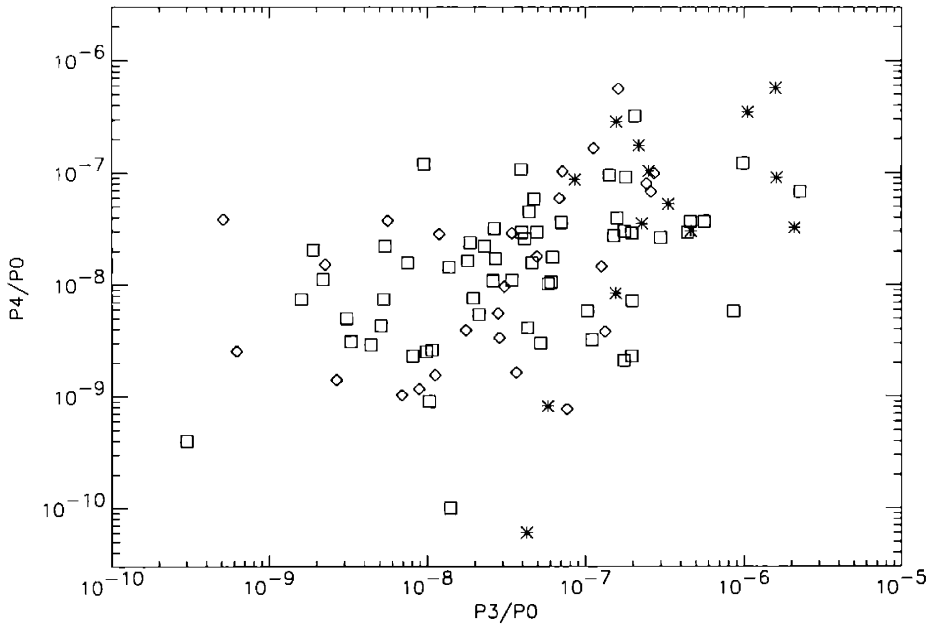

Figure 3-5 P_3/P_0 versus P_4/P_0 for an aperture radius of 0.5 Mpc. Plotted with squares are 59 $z \leq 0.2$ clusters observed with *ROSAT* (Buote & Tsai 1996). Diamonds represent our low-redshift sample, and asterisks represent our high-redshift sample.

sample, we chose only clusters with relatively high luminosities. The range of cluster luminosities is only about an order of magnitude, implying that we are comparing reasonably similar clusters, but we will consider further whether the distribution of luminosities is different for the high and low-redshift clusters. The average luminosities of the two samples are 7.4×10^{44} ergs s^{-1} for the high-redshift sample and 9.1×10^{44} ergs s^{-1} for the low-redshift sample. This difference in average luminosity is not large and is within the error in our luminosity estimates. On the other hand, investigation of Table 1 reveals that a few of the high-redshift clusters have lower luminosities than the rest of the sample. A KS-test does not show a significant difference between the two samples (probability 0.12), but a rank-sum test gives a probability of 0.047 that the samples have the same mean luminosity.

We decided to remove the five lowest luminosity clusters from the sample to test whether it would effect our results. These clusters were CLJ1113.1-2615, RXJ1350.0 +6007, V1121.0+2327, CLJ2302.8+0844, and MS2053.7-0449. With these clusters removed, the high-redshift sample has an average luminosity of 10.4×10^{44} ergs s^{-1}, and the KS and rank-sum tests of the luminosities give probabilities of 0.54 and 0.42, respectively. The difference in the average P_3/P_0 between the two samples is still very significant, with KS and rank-sum probabilities of 0.013 and 0.0018. The difference in P_4/P_0, on the other hand, is no longer significant at the 0.05 level, giving probabilities for the two tests of 0.17 and 0.10. While it is still only a marginal result, the high luminosity sample shows a more significant difference in P_2/P_0 between the high and low-redshift clusters. For P_2/P_0, the KS-test gives a probability of 0.12 and the rank-

sum test gives a probability of 0.051. P_3/P_0 is the most unambiguous indicator of an asymmetric cluster morphology, and the significant difference in P_3/P_0 between the two samples even without the low-luminosity clusters shows that the high-redshift clusters tend to have more structure than the low-redshift clusters. With five clusters removed, the high-redshift sample only contains nine clusters, perhaps leading to the marginal results for P_4/P_0.

The second effect we consider is our choice of aperture radius; we chose to use a radius of a fixed physical size rather than a fixed over-density. A radius of fixed over-density, such as r_{500}, would be difficult to determine accurately for both the disturbed and low S/N clusters, but it is worth considering whether we are comparing the same relative scale of structure in the high and low-redshift clusters. To approximate the difference in physical radius between the high and low-redshift samples that would result from using a radius of fixed over-density we examine our results for an aperture radius of 0.4 Mpc. For the high-redshift clusters, we substitute the power ratios for $R = 0.4$ Mpc and compare these to the power ratios of the low-redshift clusters at $R = 0.5$ Mpc. The shift in the power ratios of high-redshift clusters is generally within the errors and is not consistently either positive or negative. The 0.4 Mpc and 0.5 Mpc high-redshift power ratios also do not have significantly different means. Both a rank-sum test and a KS-test show that P_3/P_0 is still significantly higher for the high-redshift sample. A rank-sum test also shows a significant difference in P_4/P_0, but the KS probability is 0.10. We also considered an aperture radius of 0.3 Mpc for the high-redshift clusters, because this radius is closer to the correct comparison radius for the $z > 0.8$ clusters. We found that all three power ratios were then significantly higher for the high-redshift sample.

Finally, we look into the effect of signal-to-noise. The high-redshift clusters generally have lower S/N than the low-redshift clusters. Naively, we would not expect this to affect our results because we normalize by flux and because we take into account the uncertainty due to noise through our Monte Carlo simulations. Lower S/N simply leads to larger error bars. However, consider two cases where S/N might have an effect. First, consider that a double cluster or a highly structured cluster could have an outer, more symmetric envelope that would be visible in high-S/N data but not in low-S/N data. Second, the power ratios for a relaxed cluster might be artificially inflated in low-S/N data. To test these possibilities, we selected two low-redshift clusters, A1758 and RXJ0439.0+0520, and lowered their S/N. A1758 is one of the most disturbed looking low-redshift clusters but has an outer envelope that appears elliptical. RXJ0439.0+0520 is a round, single cluster and has among the lowest power ratios in the sample. We simulate a decrease in the S/N by rerunning our Monte Carlo procedure with a reduced cluster count rate and the same background count rate. First, we divide the adaptively binned cluster image by a factor to give the desired count rate. Then, the background image is weighted and added to the binned cluster image to give the original background count rate. Finally, we run the Monte Carlo procedure to add Poisson noise, and we recalculate the power ratios. We selected a S/N of 35, which is higher than the few lowest S/N clusters but smaller than the median value of the high-redshift sample.

For A1758, we find that the 90% confidence limits widen, as we would expect.

The median value of P_3/P_0 from the 100 trials increases with decreasing S/N, but this median value is still not as large as P_3/P_0 for the high-redshift clusters with large scale structure. The medians of P_2/P_0 and P_4/P_0 increase slightly. The new error bars completely encompass the old ones, and we believe that our Monte Carlo procedure is properly accounting for S/N at the highly structured end. For RXJ0439.0+0520, the P_2/P_0 error bars widen and completely encompass the original uncertainties, but both the median values of P_3/P_0 and P_4/P_0 and their uncertainties shift towards higher power ratios. These higher power ratios are now comparable to a couple, but not all of the relaxed, high-redshift clusters; the median P_3/P_0 for RXJ0439.0+0520 is now greater than MS0015.9+1609 and MS1137.5+6625, and the median P_4/P_0 shifts above CLJ1226.9+3332. Figure 6 shows both the observed power ratios for A1758 and RXJ0439.0+0520 and the reduced S/N power ratios compared to the high-redshift sample. With a lower limit on the S/N of 35, four high-redshift clusters and one low-redshift cluster are removed from the sample. The difference in P_3/P_0 between the two samples remains highly significant, but the difference in P_4/P_0 does not.

As a final test we analyzed a new, longer observation of CLJ1226.9+3332, a relaxed high-redshift cluster. The S/N in the 0.5 Mpc aperture is now 46 compared to 35 for the old observation. For this cluster, both P_2/P_0 and P_3/P_0 and their confidence limits shift towards smaller power ratios, but P_4/P_0 and its confidence limits increase. The new power ratios are all contained within the original 90% confidence limits, although P_3/P_0 and P_4/P_0 are near the lower and upper extremes, respectively. These results are plotted in Figure 7. For clusters with distinct substructure, our results indicate that the difference in S/N between the high and low-redshift samples is accounted for by the uncertainties. For fairly relaxed clusters with small power ratios, the effects of noise are more important. Noise can artificially inflate the power ratios in this case, although P_4/P_0 for CLJ1226.9+3332 increases for increased S/N.

Longer observations of the high-redshift, single clusters would help to better determine their structure. Correct modeling of the noise contribution is difficult, and it is a topic that we are exploring further. We have attempted some estimates of the shift in the power ratios due to noise for the relaxed clusters. We find that this shift, while significant, is not large enough to effect the conclusions of this thesis (i.e. the difference in P_3/P_0 remains highly significant). Buote & Tsai (1995) also looked at the effect of noise on the power ratios of model clusters. Their results show that for cluster models with small or zero power ratios the addition of noise significantly increases the power ratios, but not enough to make a relaxed cluster look like a disturbed cluster. For a cluster model with a perfectly round surface brightness distribution the increase in the power ratios after the addition of noise above the true value of zero is roughly consistent with our estimates of the effect of noise on our observed clusters for clusters with a similar signal-to-noise.

To summarize, we have tested three possible sources of systematic error: the inclusion of a few lower luminosity high-redshift clusters in our sample, our use of an aperture radius of fixed physical size versus fixed over-density, and the generally lower S/N of the high-redshift cluster data compared to the low-redshift data. The fact that the high-redshift clusters typically have higher P_3/P_0 than the low-redshift clusters remains highly significant under all of these tests. The difference in P_4/P_0

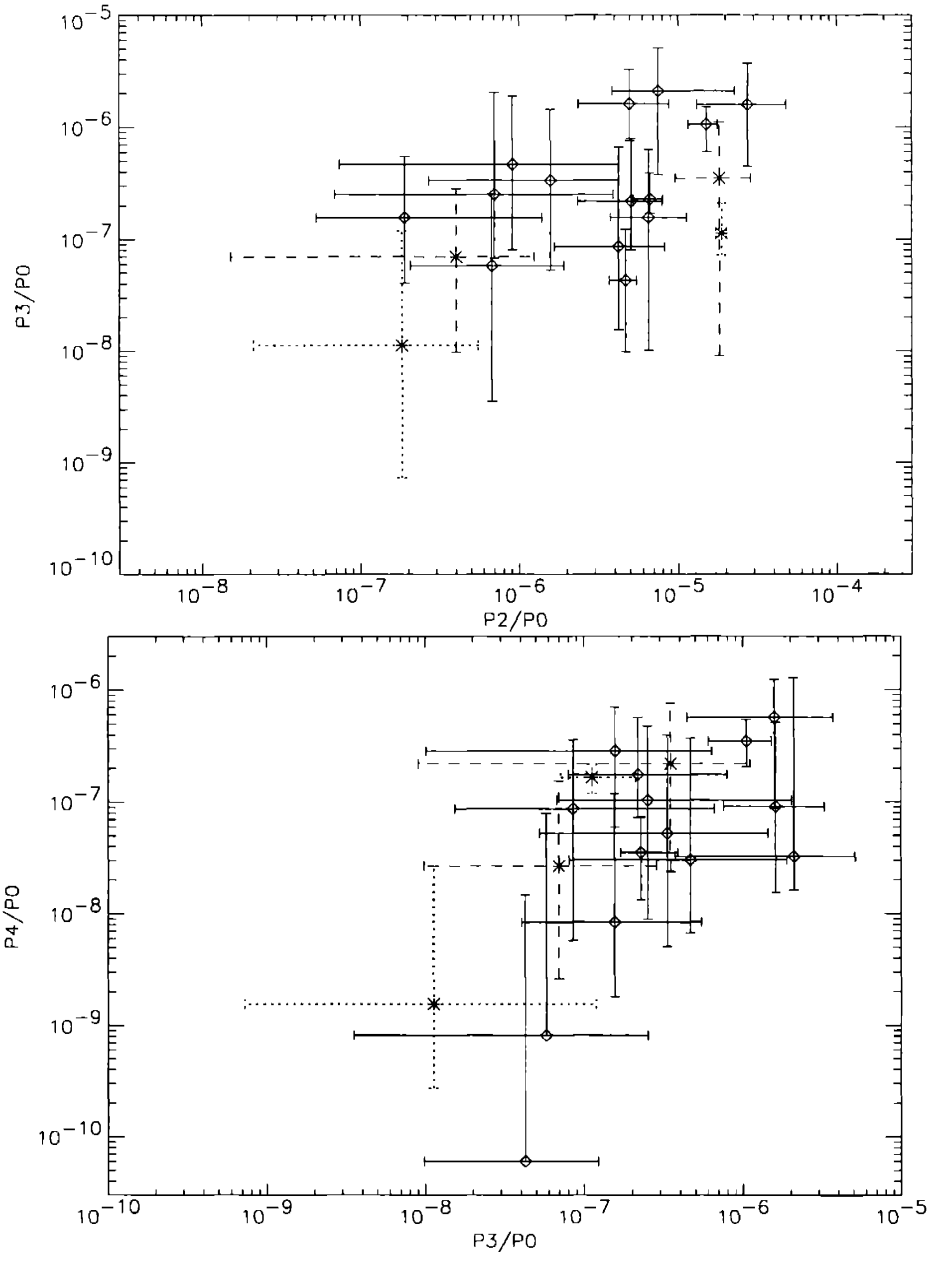

Figure 3-6 The power ratios of A1758 and RXJ0439.0+0520 with the S/N reduced to 35 compared to the observed ratios. Dotted error bars indicate the original uncertainties, and dashed error bars indicate the uncertainties for the reduced S/N. The high-redshift sample is also plotted as a reference. Top: P_2/P_0 versus P_3/P_0. Bottom: P_3/P_0 versus P_4/P_0.

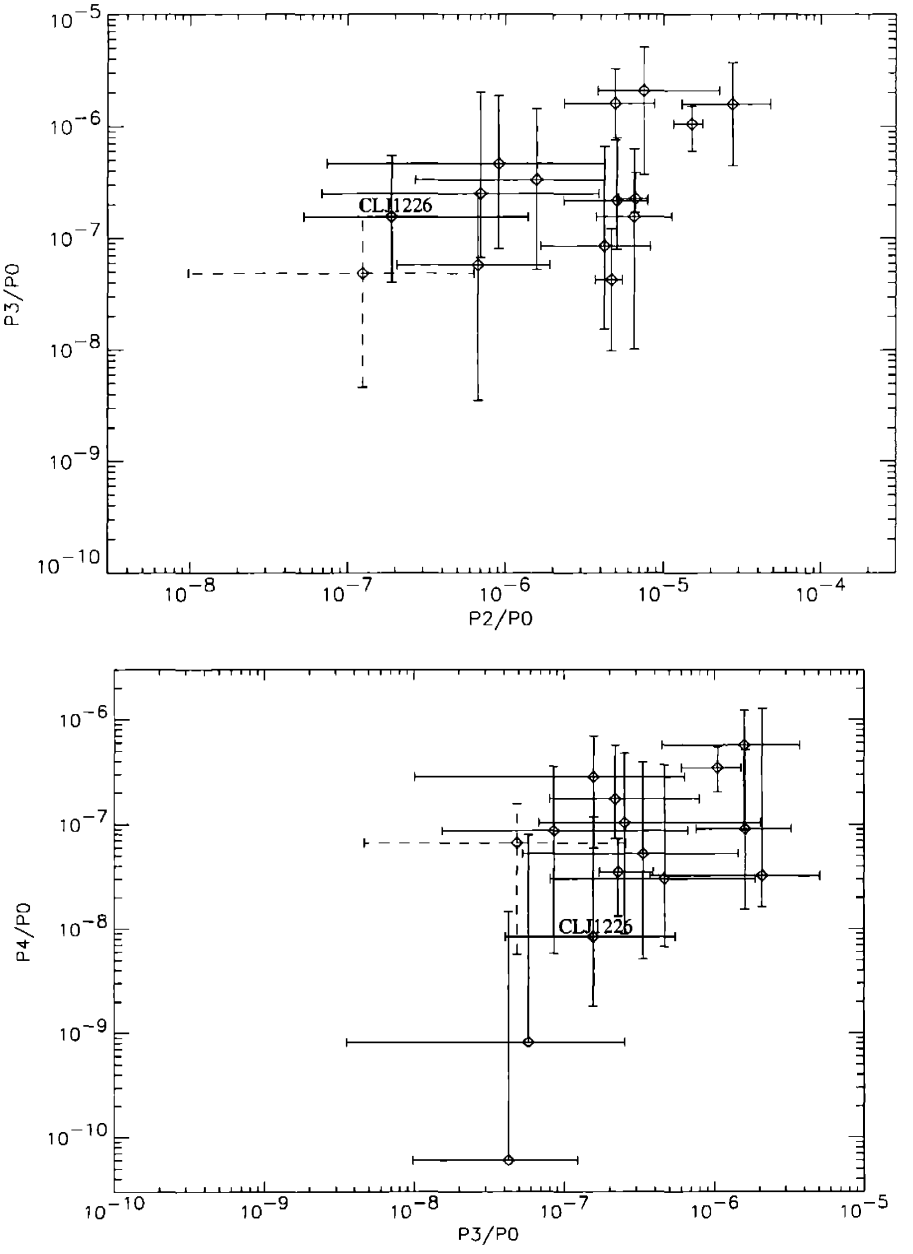

Figure 3-7 The power ratios for a new observation of CLJ1226.9+3332 compared to the high-redshift sample. The dashed error bars indicate the new observation, and the original observation is labeled CLJ1226. Top: P_2/P_0 versus P_3/P_0. Bottom: P_3/P_0 versus P_4/P_0.

between the two samples is still significant for the change in aperture radius but is marginal for the other two tests.

3.7 Conclusions

We investigate the observed evolution of cluster structure with redshift out to $z \sim 1$ using a sample of 40 clusters observed with *Chandra*. We find that, as expected from hierarchical models of structure formation, high-redshift clusters have more substructure and are dynamically younger than low-redshift clusters. Specifically, the clusters in our sample with $z > 0.5$ tend to have both higher P_3/P_0 and higher P_4/P_0 than the clusters with $z < 0.5$. We do not find a significant difference in P_2/P_0 between the two samples, possibly because of its sensitivity to ellipticity. As mentioned above, ellipticity is not a clear indicator of dynamical state; a double cluster and a relaxed, but elliptical single cluster can have the same ellipticity. The results for P_3/P_0 are robust when compared to the effects of noise, luminosity, and the choice of aperture radius. The results for P_4/P_0 are also fairly robust but show more sensitivity to these effects. As an even multipole, P_4/P_0 is also sensitive to ellipticity, although less so than P_2/P_0.

The observation of structure evolution in the redshift range probed by current cluster surveys indicates that dynamical state should be taken into account by cosmological cluster studies. In the future, we will use these results to place constraints on cosmological models by comparing the observed evolution in cluster morphology to the evolution predicted by hydrodynamic simulations. Our findings and method may also prove useful in understanding the relationship of dynamical state to other observed cluster properties such as luminosity, temperature, and galaxy evolution.

Bibliography

[1] Anders, E., & Grevesse, N. 1989, Geochimica et Cosmochimica Acta, 53, 197
[2] Buote, D.A., & Tsai, J.C. 1995, ApJ, 452, 522
[3] Buote, D.A., & Tsai, J.C. 1996, ApJ, 458, 27
[4] Buote, D.A. & Xu, G. 1997, MNRAS, 284, 439
[5] Buote, D.A. 1998, MNRAS, 293, 381
[6] Buote, D.A. 2002, in Merging Processes in Galaxy Clusters, ed. L. Feretti, I.M. Gioia, & G. Giovannini (Dordrecht: Kluwer), 79, astro-ph/0106057
[7] Campana, S., Moretti, A., Lazzati, D., & Tagliaferri, G. 2001, ApJ, 560, L19
[8] Crone, M.M., Evrard, A.E., & Richstone, D.O. 1996, ApJ, 467, 489
[9] Dutta, S.N. 1995, MNRAS, 276, 1109
[10] Ebeling, H., Edge, A.C., Bohringer, H., Allen, S.W., Crawford, C.S., Fabian, A.C., Voges, W., & Huchra, J.P. 1998, MNRAS, 301, 881
[11] Evrard, A.E., Mohr, J.J., Fabricant, D.G., & Geller, M.J. 1993, ApJ, 419, L9
[12] Gioia, I.M., & Luppino, G.A. 1994, ApJS, 94, 583
[13] Gioia, I.M., Henry, J.P., Mullis, C.R., Bohringer, H., Briel, U.G., Voges, W., & Huchra, J.P. 2003, ApJS, 149, 29
[14] Gomez, P.L., Pinkney, J., Burns, J.O., Wang, Q., Owen, F.N., & Voges, W. 1997, ApJ, 474, 580
[15] Jing, Y.P., Mo, H.J., Borner, G., & Fang, L.Z. 1995, MNRAS, 276, 417
[16] Jones, C. & Forman, W. 1992, in Clusters and Superclusters of Galaxies (NATO ASI Vol. 366), ed. A.C. Fabian, (Dordrecht/Boston/London: Kluwer), 49
[17] Kolokotronis, V., Basilakos, S., Plionis, M., & Georgabtopoulos, I. 2001, MNRAS, 320, 49
[18] Melott, A., Chambers, S.W., Miller, C.J. 2001, ApJ, 559, 75
[19] Mohr, J.J., Fabricant, D.G., & Geller, M.J. 1993, ApJ, 413, 492
[20] Mohr, J.J., Evrard, A.E., Fabricant, D.G., & Geller, M.J. 1995, ApJ, 447, 8
[21] Perlman, E.S., Horner, D.J., Jones, L.R., Scharf, C.A., Ebeling, H., Wegner, G., & Malkan, M. 2002, ApJS, 140, 265
[22] Plionis, M. 2002, ApJ, 572, 67
[23] Press, W.H., Teukolsky, S.A., Vetterling, W.T., & Flannery, B.P. 1992, Numerical Recipes in C (2d ed.; New York: Cambridge University Press)
[24] Richstone, D., Loeb, A., & Turner, E.L. 1992, ApJ, 393, 477
[25] Rizza, E., Burns, J.O., Ledlow, M.J., Owen, F.N., Voges, W., & Bliton, M. 1998, MNRAS, 301, 328
[26] Rosati, P., Della Ceca, R., Burg, R., Norman, R., & Giacconi, R. 1998, ApJ,

492, L21
[27] Sanders, J.S. & Fabian, A.C. 2001, MNRAS, 325, 178
[28] Schuecker, P., Bohringer, H., Reiprich, T.H., & Feretti, L. 2001, A&A, 378, 408
[29] Snowden, S.L., Egger, R., Freyberg, M.J., McCammon, D., Plucinsky, P.P., Sanders, W.T., Schmitt, J.H.M.M., Truemper, J., & Voges, W. 1997, ApJ, 485, 125
[30] Suwa, T., Habe, A., Yoshikawa, K., & Okamoto, T. 2003, ApJ, 588, 7
[31] Thomas, P.A., & the Virgo Consortium 1998, MNRAS, 296, 1061
[32] Tozzi, P., et al. 2001, ApJ, 562, 42
[33] Valdarnini, R., Ghizzardi, S., & Bonometto, S. 1999, New Astronomy, 4, 71
[34] Vikhlinin, A., McNamara, B.R., Forman, W., Jones, C., Quintana, H., & Hornstrup, A. 1998, ApJ, 502, 558
[35] Walpole, R.E., & Myers, R.H. 1993, Probability and Statistics for Engineers and Scientists (5th ed.; New York: Macmillan Publishing Company)

Chapter 4

Conclusions

4.1 Summary

In this thesis, I pursued two projects involving clusters of galaxies with the aims of both constraining cosmological models and acquiring a better understanding of cluster formation and evolution. The first of these projects was an examination of the *Chandra* observation of the massive, high-redshift cluster MS1054-0321. Second, I studied the evolution of cluster morphology with redshift, quantifying for the first time cluster structure out to $z \sim 1$.

At a redshift of 0.83, MS1054-0321 is the highest redshift cluster in the *Einstein* Medium Sensitivity Survey (EMSS). With the *Chandra* observation, I was able to resolve and remove point sources and to confirm that MS1054-0321 is a hot, massive cluster. I was also able to make the first positive identification of an iron line in this cluster. I find that the iron abundance is similar to the abundance found in low-redshift clusters, consistent with early enrichment of the ICM. I confirmed the presence of significant substructure in MS1054-0321 that had been previously indicated by the *ROSAT* observation (Neumann & Arnaud 2000). MS1054-0321 appears to be a nearly equal mass double cluster. I showed that the western subcluster is slightly cooler than the main cluster and, through the presence of an iron line, found it to have a redshift similar to MS1054-0321. This observation shows that the secondary is in fact merging with the main cluster and is not simply a foreground object. A third peak seen in the weak lensing mass reconstruction is not present in X-rays; however, the cluster galaxies do extend into this region (see Figures 2.5 and 2.9). When considering the overlay of the X-ray contours on both the Hubble mosaic and the weak lensing mass map it appears that both the cluster galaxies and mass associated with the western subclump lie south of the X-ray peak. This leads to the interesting possibility that the gas in the subclump is being stripped off as it falls into the cluster. Cosmologically, the observation of such a massive cluster in the EMSS alone constrains Ω_m to be less than one (Donahue et al. 1998; Jeltema et al. 2001).

Using Chandra archival data, I studied for the first time the evolution of cluster structure with redshift to $z \sim 1$. I quantified cluster morphology using the power ratio method developed by Buote and Tsai (1995). This method is capable of distinguish-

ing a large range of morphologies and has been shown to distinguish cosmological models in numerical simulations (Buote & Xu 1997; Thomas et al. 1998; Valdarnini, Ghizzardi, & Bonometto 1999; Suwa et al. 2003). I calculated power ratios for a sample of 40 X-ray selected, luminous clusters with redshifts between 0.1 and 0.9. The high-redshift clusters ($z > 0.5$) have significantly higher average P_3/P_0 and P_4/P_0 than the low-redshift clusters, which can be seen in Figure 3.4. On average, the high-redshift clusters have more structure than the low-redshift clusters, as expected from hierarchical models of structure formation. P_2/P_0 is not as good at distinguishing the two samples, perhaps because it is sensitive to ellipticity. These findings show that care must be taken to consider dynamical state in cosmological studies utilizing high-redshift clusters, and when compared to simulations the observation of structure evolution may itself lead to interesting constraints on cosmological models. In addition, these observations will aid us in understanding how other observed cluster properties (luminosity, temperature, galaxy evolution, etc.) and their evolution with redshift relate to cluster morphology.

4.2 Future Prospects

In a future study, I plan to examine cluster structure and its evolution in hydrodynamic cluster simulations to compare current theory to the *Chandra* observations. These simulations will include the expanded and higher resolution simulations of Valdarnini and simulated clusters from the Virtual Cluster Exploratory (http://vce.physics.lsa.umich.edu/index.html). The power ratio method may also prove useful to constrain systematic biases in cosmological studies based on observables such as cluster luminosity, temperature, gas mass fraction, and velocity dispersion. The power ratios have already been shown to correlate with mass deposition rate in cooling flow clusters and radio halo (or relic) power (Buote 2002).

The possibility of a third subcluster in MS1054-0321 seen in the weak lensing mass reconstruction but not seen in X-rays brings up interesting questions about the relationship of structure in the X-ray surface brightness to structure in the dark matter. It is possible that this third peak is not as fully collapsed as the other two and, therefore, is not yet visible in X-rays. Recent studies of optically-selected high-redshift clusters have also found that what appear to be optically rich clusters are underluminous in X-rays (Lubin, Mulchaey, & Postman 2004). For example, I have been involved in the X-ray follow-up of six clusters from the Red-Sequence Cluster Survey (RCS), and we find that these clusters are underluminous and, where measurable, under-hot compared to their optical richness. Lubin et al. (2004) study two high-redshift clusters selected from another optical survey and find their X-ray luminosities and temperatures to be low compared to their velocity dispersions. Again, these clusters may not be fully collapsed, or their optical properties could be the result of several structures along the line of sight. These selection effects and the evolution in the relationship of optical and X-ray mass estimators will be important to the interpretation of future and ongoing high-redshift cluster surveys in optical, X-ray, and SZ, and to the reliability of cosmological constraints placed by these surveys.

A joint study of cluster structure seen through optical, X-ray, and weak lensing observations for a large sample of clusters over a large redshift range, such as the *Chandra* sample in this thesis, would provide a much more complete view of cluster evolution. This sample would allow a comparison of cluster structure in all three cluster mass components (gas, galaxies, and dark matter) as well as a better understanding of the interactions between the components. Kolokotronis et al. (2001) compared morphological features in the galaxy and X-ray distributions of 22 low-redshift clusters and found that they generally correlate well, although 22% show optical subclumps not present in X-rays. This study should be expanded to look at high-redshift clusters, where the optical and X-ray properties may diverge, and to include lensing observations, which to probe cluster dark matter. In addition, the simulations of Valdarnini et al. (1999) and Suwa et al. (2003) show that that the power ratios calculated from the projected mass density are generally larger than those calculated from the X-ray surface brightness because the collisional gas relaxes faster than the collisionless dark matter. It may be possible to use the power ratios to examine the relative relaxation times of the cluster mass components and to constrain dark matter self-interaction.

Galaxy evolution in clusters may also be tied to cluster dynamical state. Observations show that the morphologies and stellar content of galaxies are tied to environment, but the mechanisms responsible for this are not clearly understood (e.g., Dressler 1980; Butcher & Oemler 1984; Abraham et al. 1996; Ellingson et al. 2001; Kodama et al. 2001). It is possible that an increase in cluster merging at higher redshifts is the underlying cause of the Butcher-Oemler effect, and a comparison of the power ratios to cluster blue fraction could test this theory.

Finally, longer observations of the high-redshift clusters and a larger sample could significantly reduce the uncertainties in the power ratios, allowing firmer constraints to be placed on structure evolution. With the *Chandra* and *XMM-Newton* archives continually growing, this may be possible in the near future.

Bibliography

[1] Abraham, R.G., Smecker-Hane, T.A., Hutchings, J.B., Carlberg, R.G., Yee, H.K.C., Ellingson, E., Morris, S., Oke, J.B., & Rigler, M. 1996, ApJ, 471, 694

[2] Buote, D.A., & Tsai, J.C. 1995, ApJ, 452, 522

[3] Buote, D.A. & Xu, G. 1997, MNRAS, 284, 439

[4] Buote, D.A. 2002, in Merging Processes in Galaxy Clusters, ed. L. Feretti, I.M. Gioia, & G. Giovannini (Dordrecht: Kluwer), 79, astro-ph/0106057

[5] Butcher, H., & Oemler, A. 1984, ApJ, 285, 426

[6] Donahue, M., Voit, G.M., Gioia, I., Luppino, G., Hughes, J.P., & Stocke, J.T. 1998, ApJ, 502, 550

[7] Dressler, A. 1980, ApJ, 236, 351

[8] Ellingson, E., Lin, H., Yee, H.K.C., & Carlberg, R.G. 2001, ApJ, 547, 609

[9] Jeltema, T.E., Canizares, C.R., Bautz, M.W., Malm, M.R., Donahue, M., & Garmire, G.P. 2001, ApJ, 562, 124

[10] Kodama, T., Smail, I., Nakata, F., Okamura, S., & Bower, R.G. 2001, ApJ, 562, L9

[11] Kolokotronis, V., Basilakos, S., Plionis, M., & Georgabtopoulos, I. 2001, MNRAS, 320, 49

[12] Lubin, L.M., Mulchaey, J.S., & Postman, M. 2004, ApJ, 601, L9

[13] Neumann, D.M., & Arnaud, M. 2000, ApJ, 542, 35

[14] Suwa, T., Habe, A., Yoshikawa, K., & Okamoto, T. 2003, ApJ, 588, 7

[15] Thomas, P.A., & the Virgo Consortium 1998, MNRAS, 296, 1061

[16] Valdarnini, R., Ghizzardi, S., & Bonometto, S. 1999, New Astronomy, 4, 71

Appendix A

Notes on Individual Clusters

Here we give a brief description of the clusters in our sample. Also listed are any specific notes on their processing. For the clusters that were not selected from either the EMSS or BCS, we indicate the survey in which they were discovered. The references for these surveys are:
160 deg^2 survey - Vikhlinin et al. 1998
RDCS - Rosati et al. 1998
WARPS - Perlman et al. 2002
NEP - Gioia et al. 2003

MS0015.9+1609 - This cluster is elliptical and has an asymmetric core structure. It is one of three clusters for which the uncertainties calculated from the Monte Carlo simulations do not contain one of the observed power ratios. In this case, P_4/P_0 is below the error bars. The uncertainties are 90% confidence limits, and we expect that the power ratios will occasionally fall outside of these.
CLJ0152.7-1357 - This cluster is a well-separated double cluster with nearly equal mass subclusters. Discovered in a number of surveys including RDCS, WARPS, and the bright SHARC (Romer et al. 2000). It was also discovered by *Einstein*, but its significance was underestimated due to its morphology, and it was not included in the EMSS cluster catalog.
A267 - A267 appears to be a disturbed, single component cluster. Its core is very elliptical, offset from the center, and twists from being extended in the NE-SW direction to extending S. The cluster as a whole is also extended in the NE-SW direction. A smaller extended source appears 2 Mpc east of the cluster. There were three observations of this cluster in the archive but one was very short and another had a high background count rate. We used only the longest observation. This cluster is one of three clusters where the uncertainties calculated from the Monte Carlo simulations do not contain one of the observed power ratios. For A267, P_3/P_0 is below the error bars.
MS0302.7+1658 - This cluster is elliptical, the core is offset to the south, and it has excess emission to the NW making the outer contours look triangular.
RXJ0439.0+0715 - RXJ0439.0+0715 is a single, elliptical cluster. The core is offset a bit from the center of the cluster, but otherwise it appears fairly symmetric. This

cluster had three observations in the archive. However, one of these observations was for less than a kilosecond, and another observation had a high background rate. We only used the longest of the three observations.

RXJ0439.0+0520 - A fairly round, relaxed looking single cluster. For this cluster, the 0.5 Mpc aperture fell on two of the ACIS-I CCDs.

A520 - This cluster has clear substructure in the form of a bright arm of emission leading to a bright knot to the SW. This clump is cooler than the surrounding gas, and it appears to be a group of galaxies that has recently passed through the main cluster (Govoni et al. 2004).

MS0451.6-0305 - This cluster is elliptical and extended in a roughly E-W direction, with excess emission to the E. The core is lumpy and extended, and there is evidence that the BCG has not yet settled into the center of the cluster (Donahue et al. 2003). There were two observations of this cluster in the archive, but both the instrument and the focal plane temperature differed between the observations. We chose to use only the longer, ACIS-S observation.

CLJ0542.8-4100 - This cluster is extended in the E-W direction. The core is elliptical, offset from the center, and shows a position angle twist from E-W to SE.

A665 - A665 is a very odd looking cluster with a twisted, almost S-shaped core and a large extension to the NW. Several observation suggest that this cluster is currently undergoing a merger (Govoni et al. 2004; Gomez, Hughes, & Birkinshaw 2000; Buote & Tsai 1996). The 0.5 Mpc aperture fell on two of the ACIS-I CCDs.

ZWCL1953 - This cluster has a double peaked core which is offset from the centroid. It is also extended in a roughly N-S direction.

MS0906.5+1110 - This cluster is elliptical and fairly relaxed with some possible extension in the core. There is a second extended structure at the edge of the CCD which may or may not be associated with MS0906.5+1110. However, this component does not fall in the 0.5 Mpc aperture.

A773 - A773 is roughly elliptical and has a very elongated, slightly curved core. The temperature map and galaxy distribution suggest that it is undergoing a merger (Govoni et al. 2004). In this observation, the 0.5 Mpc aperture fell on two of the ACIS-I CCDs.

A781 - This is a complex cluster with multiple peaks. The core is offset from the center and has an extension that curves towards a peak to the north. There is also an extension towards a peak to the east, but the peak itself falls outside the 0.5 Mpc aperture. To the E-SE there are two other extended X-ray sources which may form part of line of clusters along a filament. The closest of these is over 1.2 Mpc from the center of A781.

A963 - A963 is elliptical and very relaxed looking with some possible very small scale structure in the core. We included the effects of background noise when calculating the uncertainties in the power ratios of this cluster.

ZWCL3146 - This cluster is elliptical and fairly relaxed and has a slightly offset core. ZWCL3146 is a cooling flow cluster with a complicated core structure (Forman et al. 2003), but this structure is very small scale and therefore not important to this analysis. The 0.5 Mpc aperture fell on two of the ACIS-I CCDs.

MS1054.5-0321 - MS1054.5-0321 is a nearly equal mass, double cluster and the highest redshift cluster in the EMSS.
CLJ1113.1-2615 - A single, relatively relaxed looking cluster. In the smooth image it appears to be slightly triangular rather than perfectly round. Discovered in WARPS. For this cluster, the background moments were similar to the cluster moments, and we included the effects of background noise in the calculation of the uncertainties.
V1121.0+2327 - V1121.0+2327 is a complicated cluster with 2-3 peaks and very twisted emission. Discovered in the 160 deg^2 survey. This cluster has background moments similar to the cluster moments, and we included the effects of background noise in the uncertainties.
MS1137.5+6625 - A relaxed looking single cluster. We included the effects of background noise in the calculation of the uncertainties for this cluster. This cluster is one of three clusters where the uncertainties calculated from the Monte Carlo simulations do not contain one of the power ratios. In this case, P_4/P_0 is below the error bars.
A1413 - An elliptical, but otherwise relaxed looking cluster. There were two observations of this cluster in the archive, but one of these observations had a high background rate.
V1221.4+4918 - This cluster has two peaks surrounded by an outer envelope that is extended in the NW-SE direction. Discovered in the 160 deg^2 survey.
CLJ1226.9+3332 - CLJ1226.9+3332 is the highest redshift cluster in our sample, and it is a fairly relaxed single cluster. In the smoothed image, it appears boxy rather than perfectly round. Maughan et al. (2004) observed this cluster with *XMM-Newton*. They find it to be very hot and fairly isothermal. There are possibly two other extended sources near this cluster, one 1.8 Mpc to the east and one 4.5 Mpc to the north. CLJ1226.9+3332 was discovered in WARPS. We included the effects of background noise in the calculation of the uncertainties in the power ratios.
A1758 - One of the most complicated looking low-redshift clusters. A1758 has approximately two main clumps but these are lumpy and disrupted, probably due to an ongoing merger where the two clusters have already passed through each other. The outer envelope of this cluster is elliptical.
RXJ1350.0+6007 - A disturbed looking single cluster with an offset core and a large position angle twist from E-W to SE. Discovered in the RDCS. We included the effects of background noise in the calculation of the uncertainties in the power ratios for this cluster.
MS1358.4+6245 - MS1358.4+6245 is a relaxed, cooling flow cluster (Arabadjis, Bautz, & Garmire 2002). In the smoothed image, it is elliptical and has some extension in the core; however, this core structure is fairly small scale. We included the effects of background noise in the calculation of the uncertainties.
A1914 - This cluster has two peaks surrounded by an outer roughly elliptical envelope. The SE peak extends and curves towards the NW peak. The temperature map shows a hot region between the two peaks suggesting shock heated gas (Govoni et al. 2004). In this observation, the 0.5 Mpc aperture fell on two of the ACIS-I CCDs.
A2034 - A2034 is fairly round but has some small scale core structure, including a curved structure extending away from the peak. It also shows both a northern cold

front and a southern excess (Kempner, Sarazin, & Markevitch 2003). It is currently unclear if the southern excess is associated with A2034, and Kempner et al. (2003) suggest that it may be a background cluster. Most of the southern excess is not in the 0.5 Mpc aperture, but our aperture does overlap the top of this feature. Comparing to the 0.3 Mpc and 0.4 Mpc apertures which do not contain the excess, P_3/P_0 and P_4/P_0 do shift somewhat. However, this shift is towards smaller values of the power ratios which would only strengthen our conclusions. This cluster has the lowest redshift in our sample, and the 0.5 Mpc aperture overlapped all four ACIS-I CCDs.

RXJ1532.9+3021 - Relaxed, slightly elliptical single cluster. There is some very small scale extension in the core of this cluster. There were two 10 ksec observations of RXJ1532.9+3021, one with ACIS-I and one with ACIS-S. We used only the ACIS-S observation which appeared to have a higher net cluster count rate.

A2111 - This cluster is very elongated and extended towards the NW. It also has a double peaked core.

A2218 - A2218 looks fairly relaxed and symmetric except for a slightly offset core and some very small scale core structure. Govoni et al. (2004) find an asymmetric temperature structure, and they suggest that this cluster is a late-stage merger. This cluster had three observations in the archive, including two short observations at a focal plane temperature of -110°C and a longer observation at -120°C. We used only the last observation which had more than double the exposure time of the other two. The 0.5 Mpc aperture fell on three of the ACIS-I CCDs.

A2219 - This cluster is very elliptical and elongated in the NW-SE direction. It also has some small scale lumpiness in the center. This cluster has both an elongated galaxy distribution and an elongated radio halo (Boschin et al. 2004). Boschin et al. (2004) suggest that A2219 is a late-stage merger.

RXJ1716.9+6708 - This cluster has a small subcluster or group to the NE of the main cluster. In addition, the core is elongated in the direction of the subcluster. In NED, we found two cluster galaxies associated with this small clump. RXJ1716.9+6708 was discovered in the NEP. The optical galaxy distribution resembles an inverted S-shaped filament (Gioia et al. 1999).

RXJ1720.1+2638 - A fairly round, relaxed cluster. It becomes somewhat elliptical outside the 0.5 Mpc aperture. There were three observations of this cluster, one was very short and the other two were at different focal plane temperatures. We use only the longest observation performed at a focal plane temperature of -110°C. The 0.5 Mpc aperture fell on three of the ACIS-I CCDs.

A2261 - This cluster has a small secondary clump to the west of the main cluster. This clump does not fall in the 0.5 Mpc aperture, and within the aperture A2261 is very round and relaxed.

MS2053.7-0449 - A single cluster; it is extended in the NW-SE direction and slightly lumpy rather than perfectly elliptical. For this cluster, we merged two observations. Both observations were made with ACIS-I at a focal plane temperature of -120°C, one in F mode and one in VF mode. The two observations were aligned by hand using six bright X-ray point sources that appear in both images.

RXJ2129.6+0005 - An elliptical, relaxed looking single cluster. It is elongated in the NE-SW direction.

MS2137.3-2353 - MS2137.3-2353 is a very relaxed looking, slightly elliptical cluster.
A2390 - This cluster has a large scale extension to the east as well as a pointy or triangular extension to the NW, giving it an odd appearance. It also has some very small scale structure in the core. A2390 was observed twice with *Chandra*, but we use only the observation at a focal plane temperature of $-120°$C.
CLJ2302.8+0844 - This cluster is a fairly relaxed looking single cluster. There is a large foreground galaxy near this cluster, but it is not in the 0.5 Mpc aperture. Discovered in WARPS. For this cluster, the background moments were similar to the cluster moments, and we included the effects of background noise in the calculation of the uncertainties.

Bibliography

[1] Arabadjis, J.S., Bautz, M.W., & Garmire, G.P. 2002, ApJ, 572, 66

[2] Boschin, W., Girardi, M., Barrena, R., Biviano, A., Feretti, L., & Ramella, M. 2004, A&A, 416, 839

[3] Buote, D.A., & Tsai, J.C. 1996, ApJ, 458, 27

[4] Donahue, M., Gaskin, J.A., Patel, S.K., Joy, M., Clowe, D., & Hughes, J.P. 2003, ApJ, 598, 190

[5] Forman, W., Churazov, E., David, L., Durret, F., Jones, C., Markevitch, M., Murray, S., Sun, M., & Vikhlinin, A. 2003, in IAU Symposium 214, High Energy Processes and Phenomena in Astrophysics, ed. X. D. Li, V. Trimble & Z. R. Wang, astro-ph/0301476

[6] Gioia, I.M., Henry, J.P., Mullis, C.R., Ebeling, H., & Wolter, A. 1999, AJ, 117, 2608

[7] Gioia, I.M., Henry, J.P., Mullis, C.R., Bohringer, H., Briel, U.G., Voges, W., & Huchra, J.P. 2003, ApJS, 149, 29

[8] Gomez, P.L., Hughes, J.P., & Birkinshaw, M. 2000, ApJ, 540, 726

[9] Govoni, F., Markevitch, M., Vikhlinin, A., VanSpeybroeck, L., Feretti, L., & Giovannini, G. 2004, ApJ, 605, 695

[10] Kempner, K.C., Sarazin, C.L., & Markevitch, M. 2003, ApJ, 593, 291

[11] Maughan, B.J., Jones, L.R., Ebeling, H., & Scharf, C. 2004, MNRAS, in press, astro-ph/0403521

[12] Perlman, E.S., Horner, D.J., Jones, L.R., Scharf, C.A., Ebeling, H., Wegner, G., & Malkan, M. 2002, ApJS, 140, 265

[13] Romer, A.K., et al. 2000, ApJS, 126, 209

[14] Rosati, P., Della Ceca, R., Burg, R., Norman, R., & Giacconi, R. 1998, ApJ, 492, L21

[15] Vikhlinin, A., McNamara, B.R., Forman, W., Jones, C., Quintana, H., & Hornstrup, A. 1998, ApJ, 502, 558

Appendix B

Cluster Images

In this appendix, we show smoothed *Chandra* images of the clusters in our sample in order of increasing redshift. These images were created using the CIAO program *csmooth*, and they are approximately 1.4 Mpc on a side. The point source removal and exposure correction have not been applied to these images. For those clusters where the aperture used to calculate the power ratios fell on multiple CCDs the low exposure regions (chip gaps and some bad columns) of the image have been masked out.

A2034

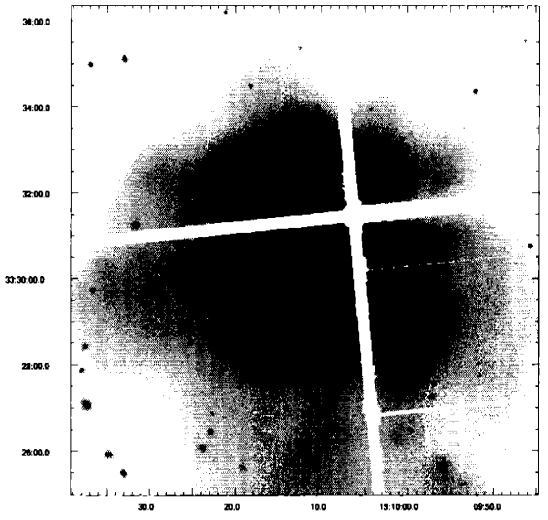

A1413

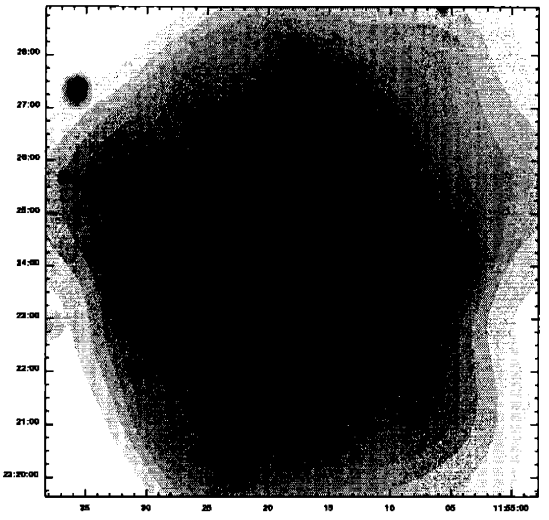

RXJ1720.1+2638

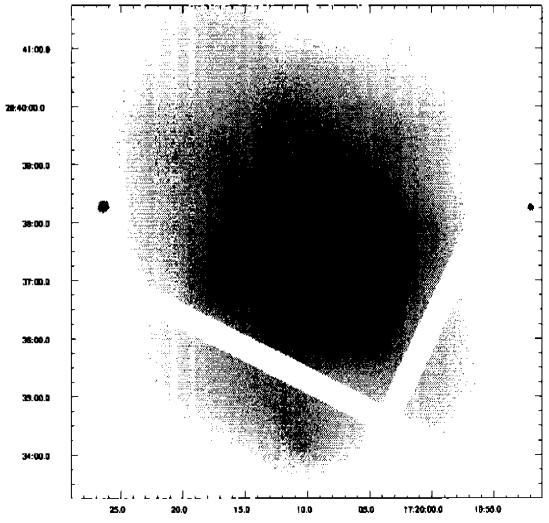

A1914

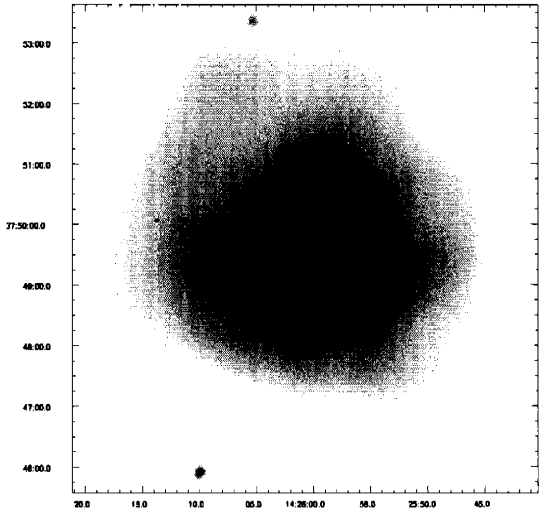

A2218

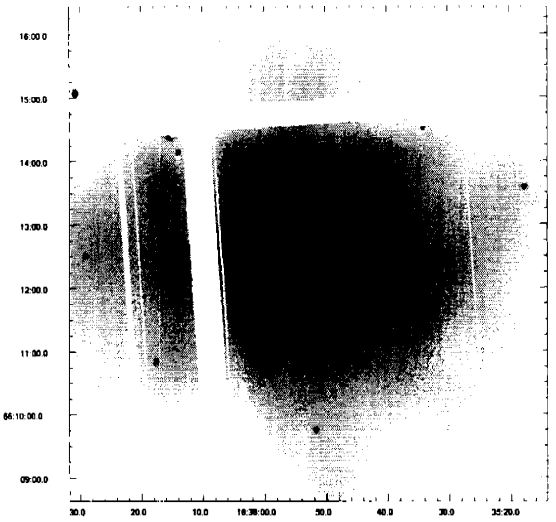

MS0906.5+1110

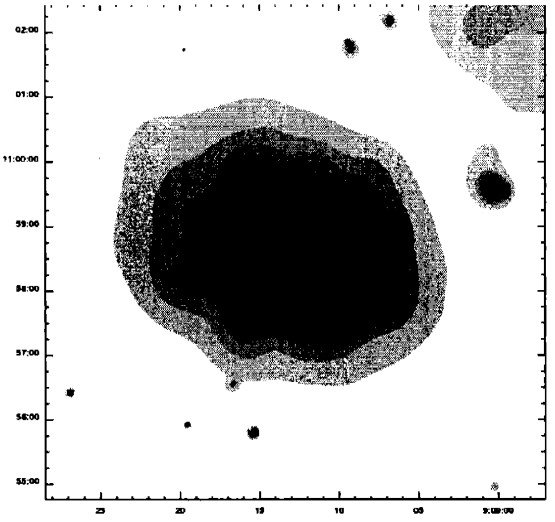

A665

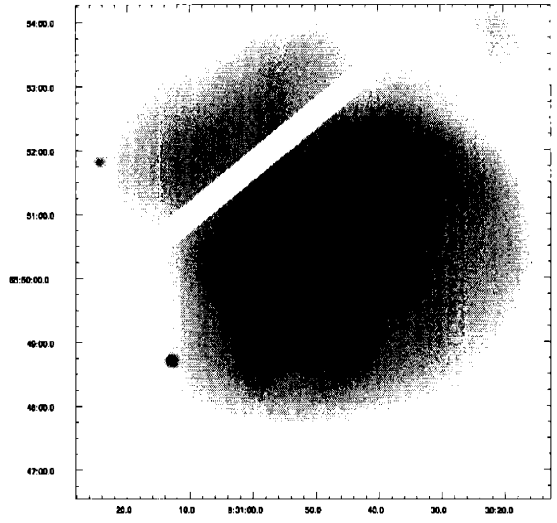

A520

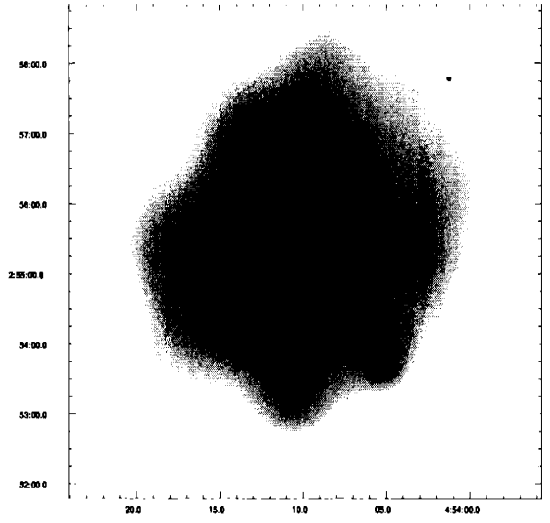

RXJ0439.0+0520

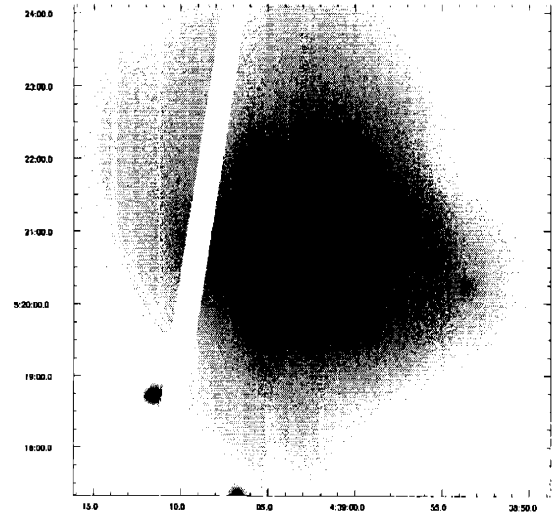

A963

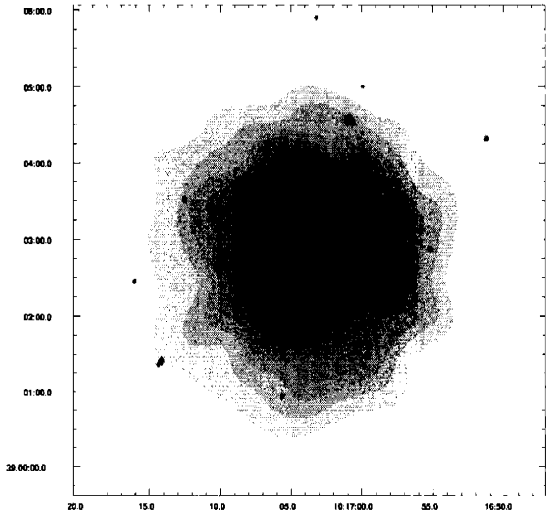

A773

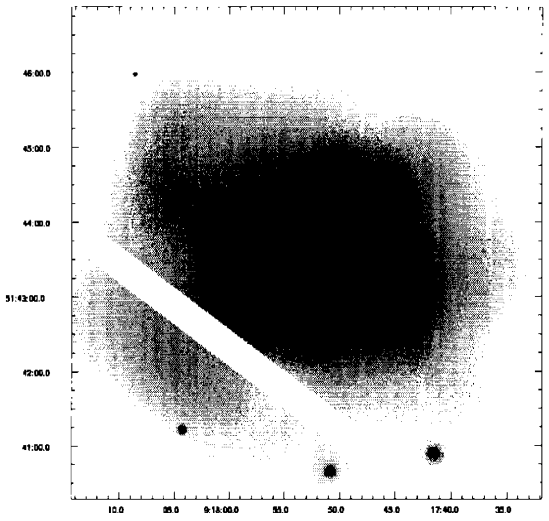

A2261

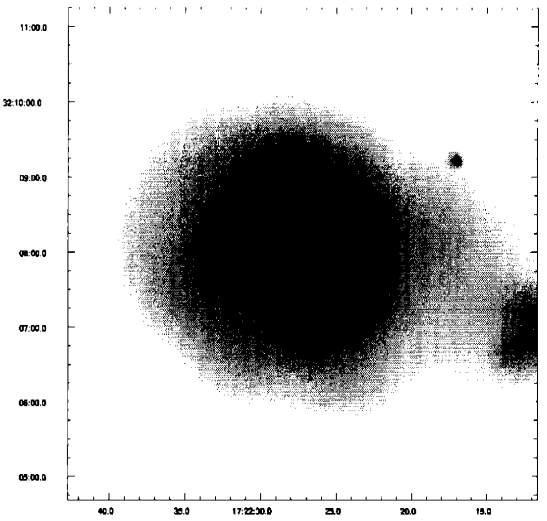

A2219

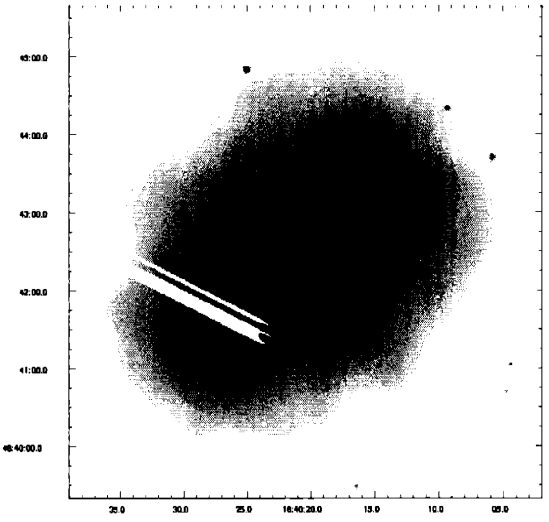

A2111

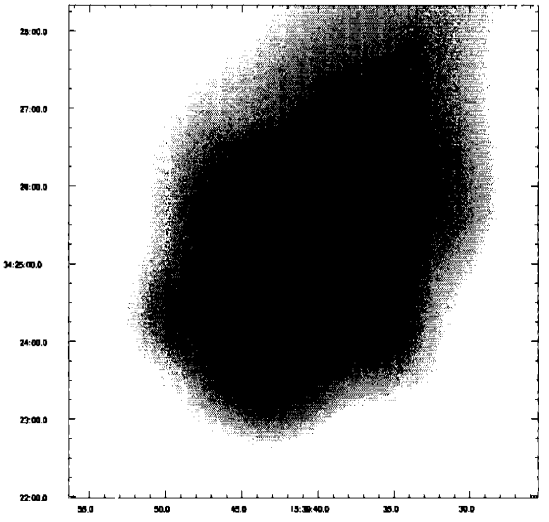

A2390

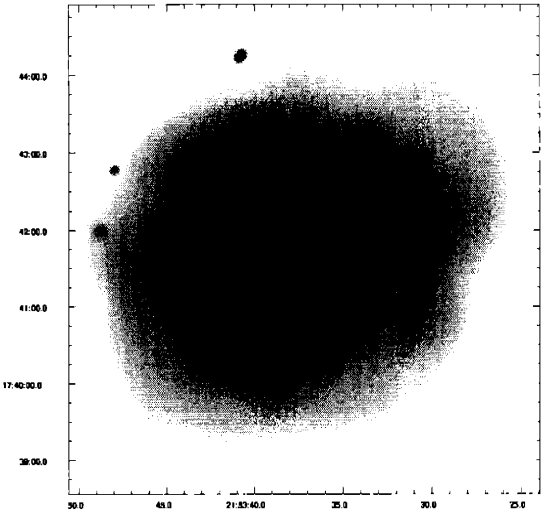

A267

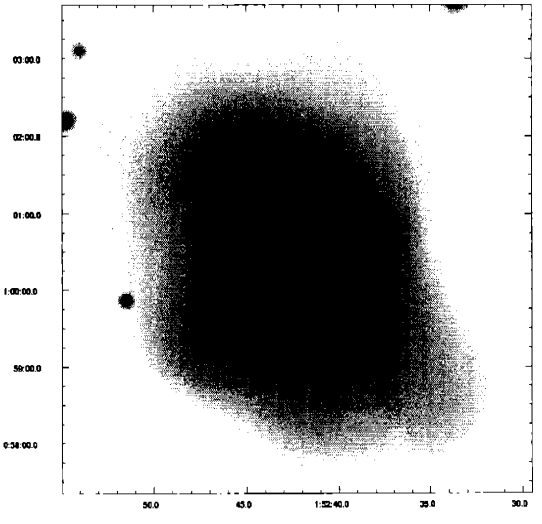

RXJ2129.6+0005

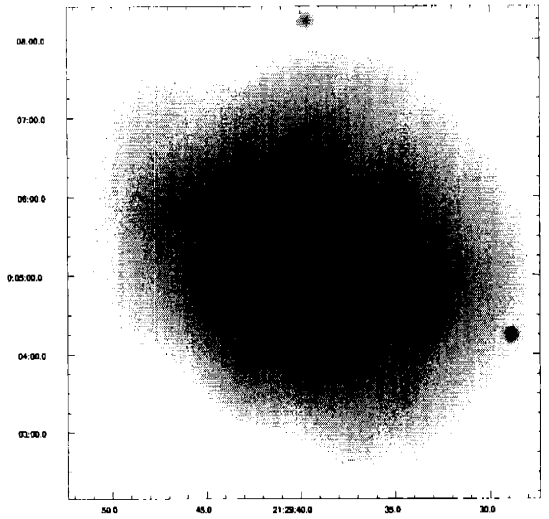

RXJ0439.0+0715

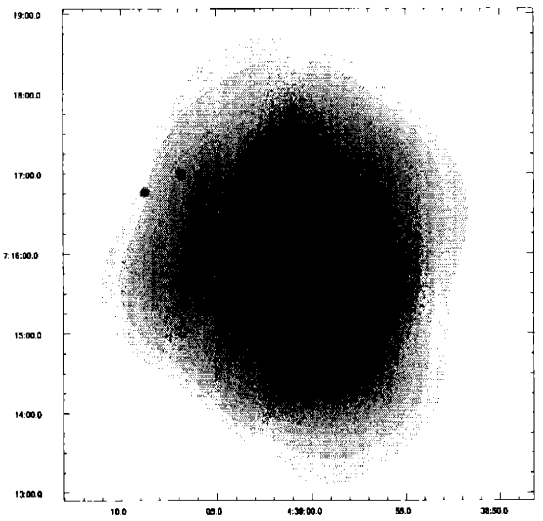

A1758

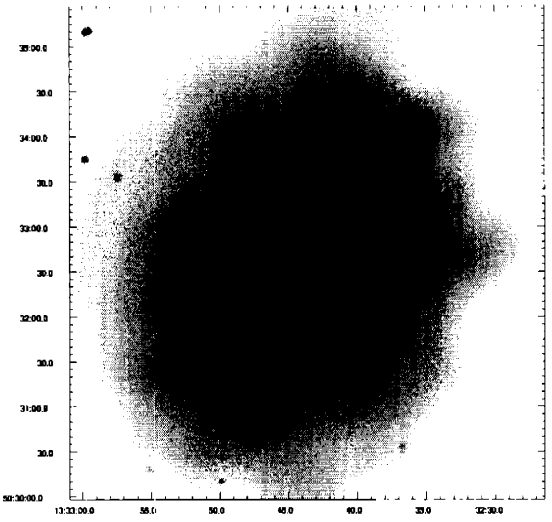

ZWCL3146

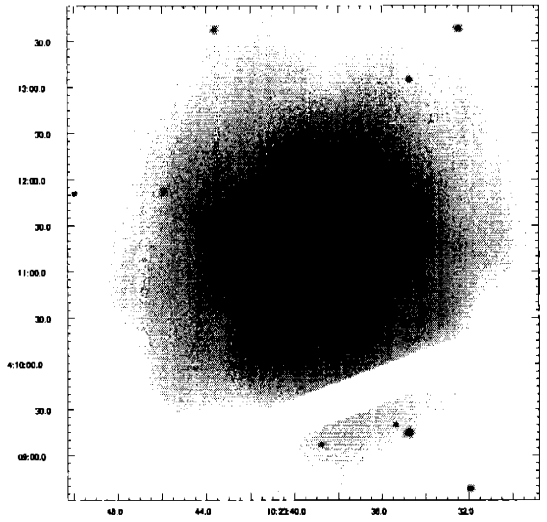

A781

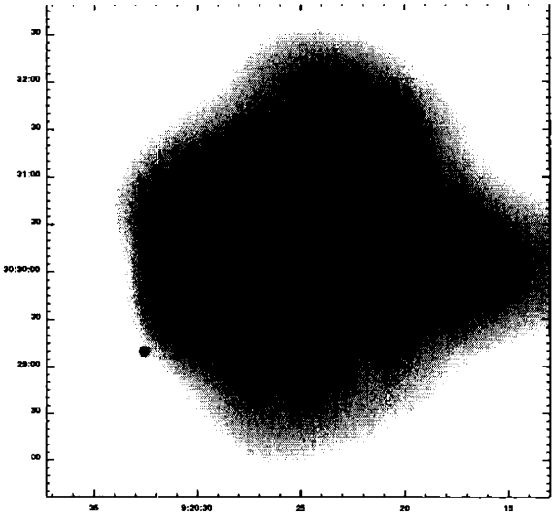

MS2137.3−2353

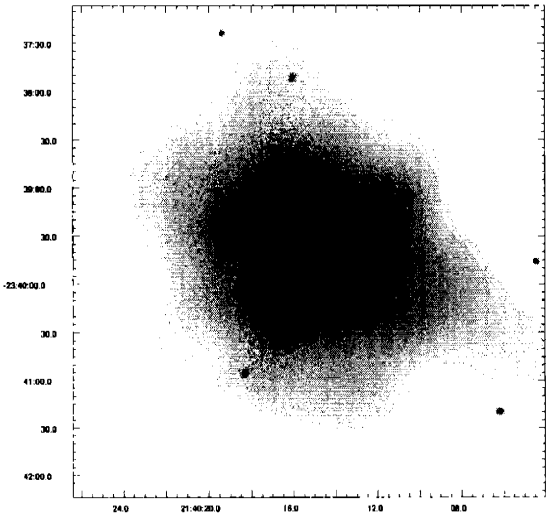

MS1358.4+6245

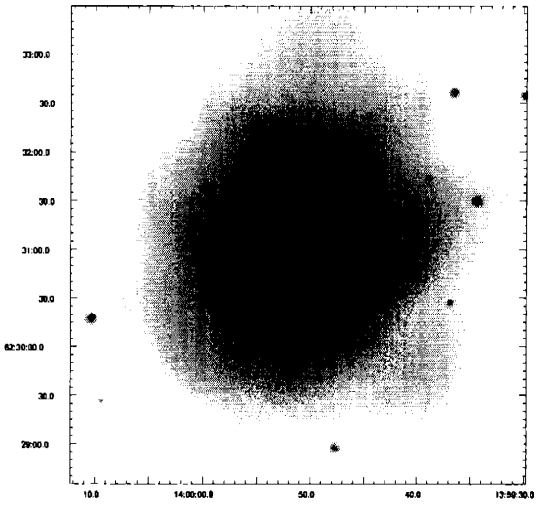

RXJ1532.9+3021

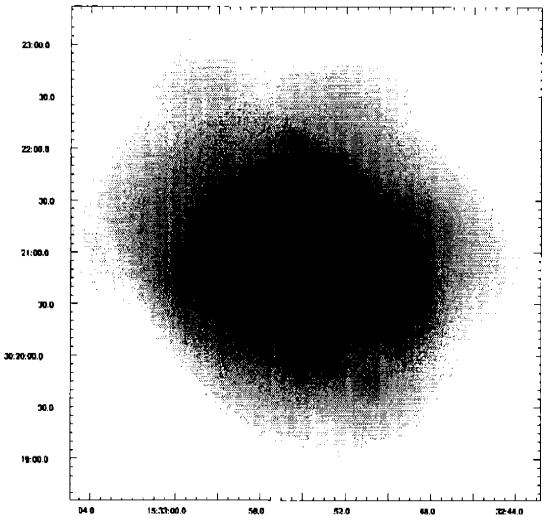

ZWCL1953

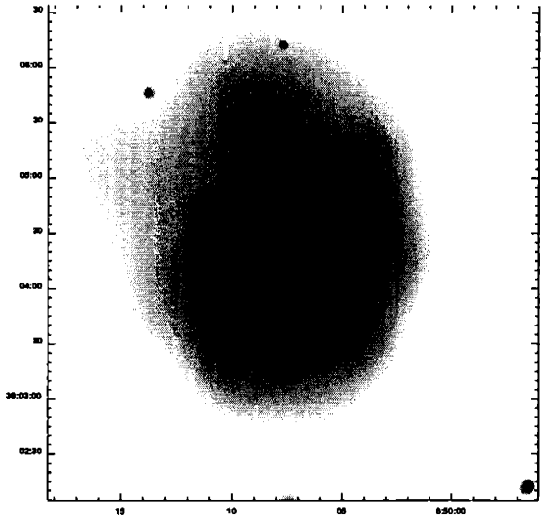

MS0302.7+1658

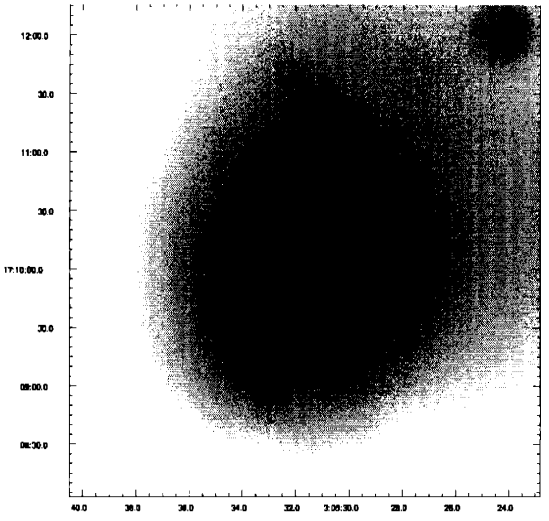

MS0451.6−0305

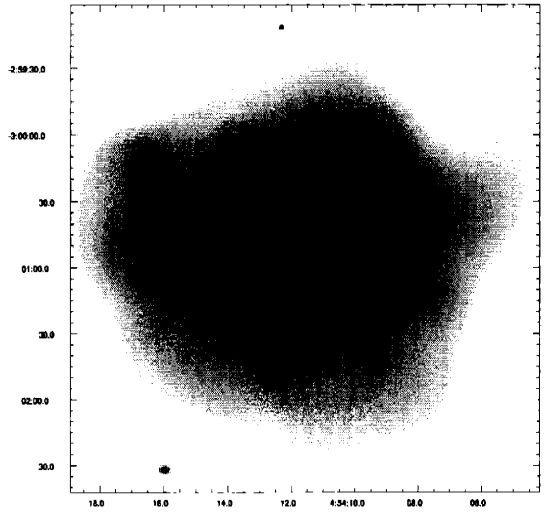

MS0015.9+1609

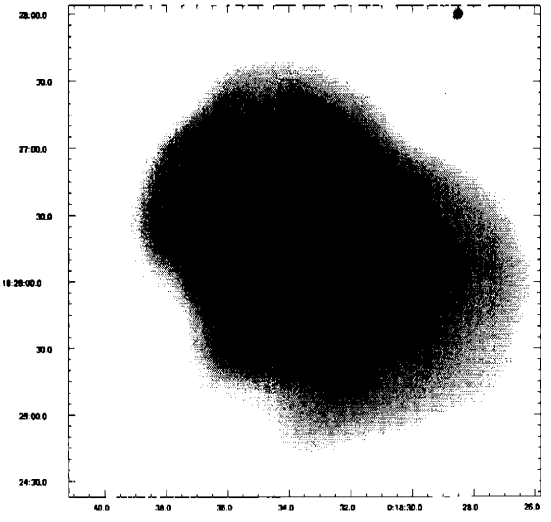

V1121.0+2327

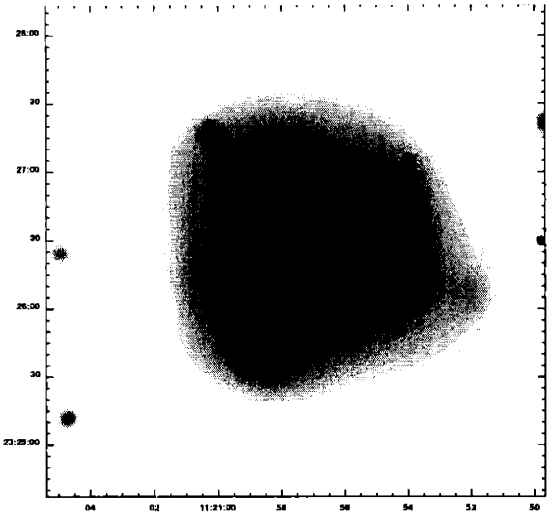

MS2053.7−0449

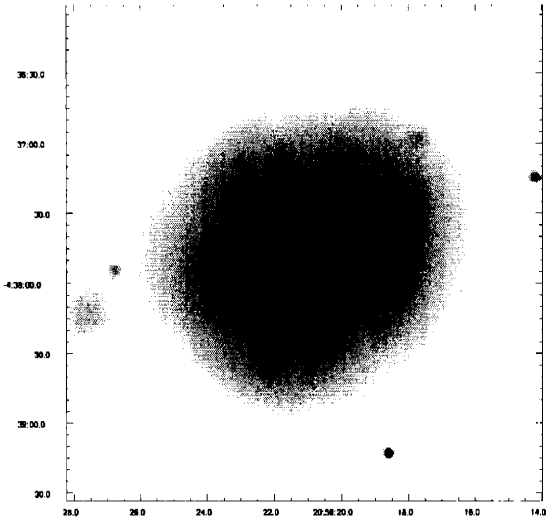

CLJ0542.8−4100

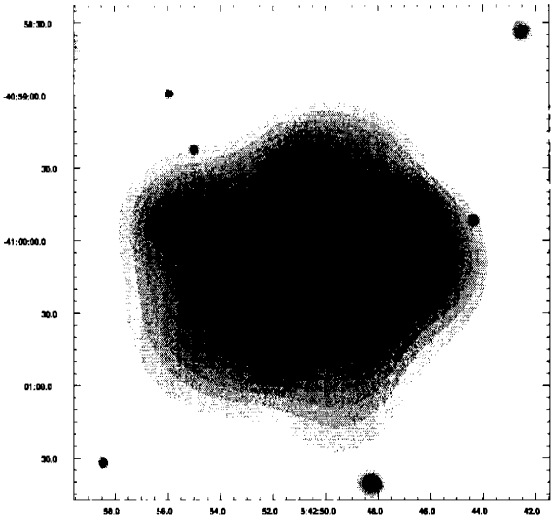

V1221.0+2327

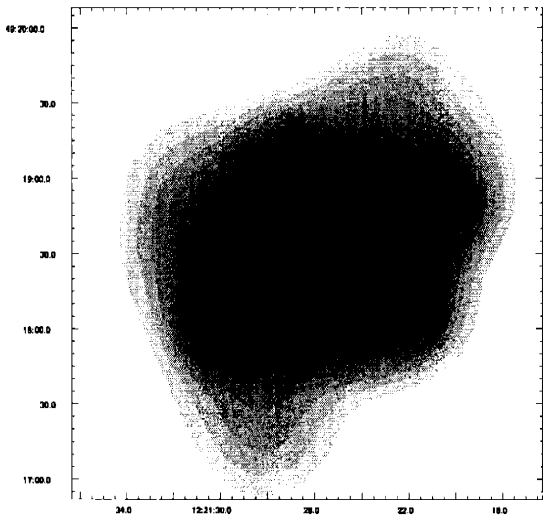

CLJ1113.1−2615

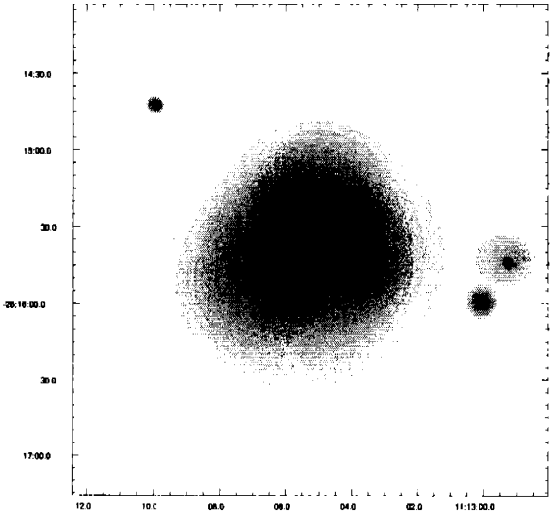

CLJ2302.8+0844

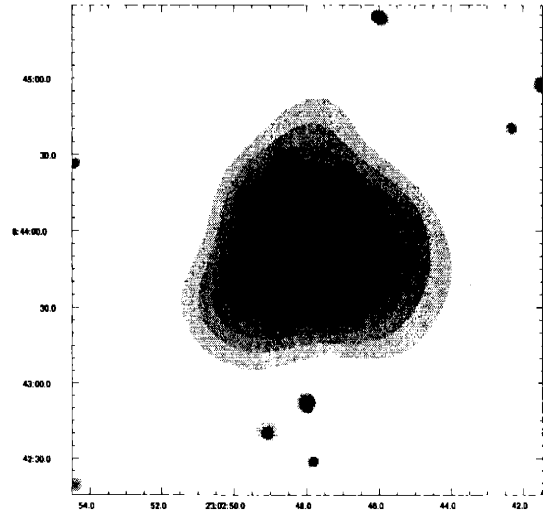

MS1137.5+6625

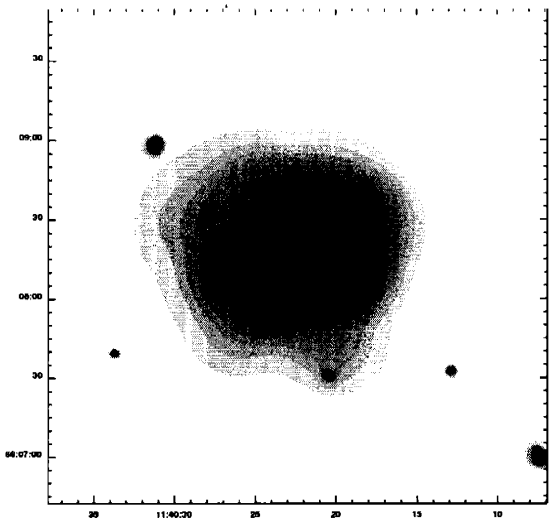

RXJ1350.0+6007

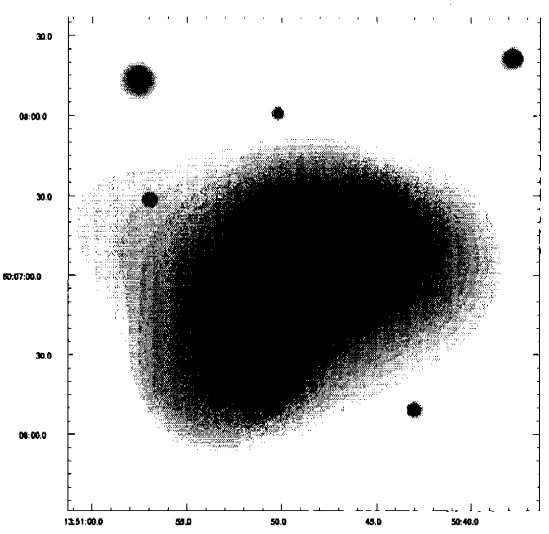

RXJ1716.9+6708

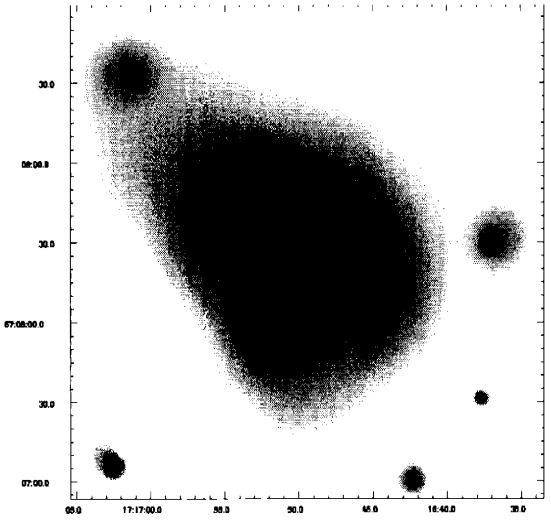

CLJ0152.7−1357

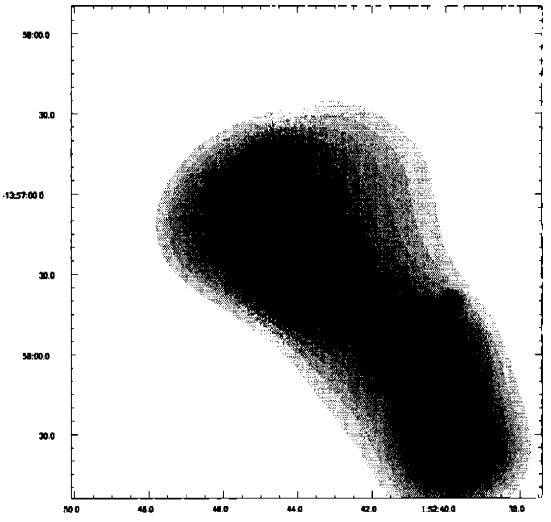

MS1054.5−0321

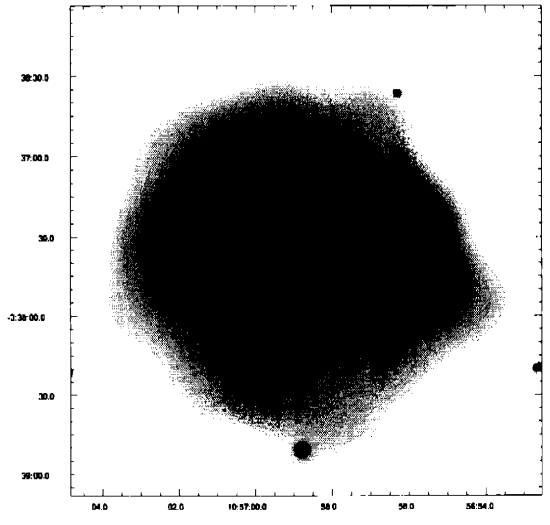

CLJ1226.9+3332